

GALACTIC H₂CO DENSITOMETRY I: PILOT SURVEY OF ULTRACOMPACT H II REGIONS AND METHODOLOGY

ADAM GINSBURG, JEREMY DARLING, CARA BATTERSBY, BEN ZEIGER, AND JOHN BALLY

Center for Astrophysics and Space Astronomy, Department of Astrophysical and Planetary Sciences, University of Colorado 389 UCB, Boulder, CO 80309-0389

Draft version July 22, 2022

ABSTRACT

We present a pilot survey of 21 lines of sight towards ultracompact H II (UCH II) regions and three towards continuum-free lines of sight in the formaldehyde (H₂CO) 1₁₀ – 1₁₁ (6 cm) and 2₁₁ – 2₁₂ (2 cm) transitions, using the H₂CO centimeter lines as a molecular gas densitometer. Using Arecibo and Green Bank beam-matched observations, we measure the density of 51 detected H₂CO line pairs and present upper limits on density for an additional 24 detected 1₁₀ – 1₁₁ lines. We analyze the systematic uncertainties in the H₂CO densitometer, achieving H₂ density measurements with accuracies $\sim 0.1 - 0.3$ dex. The densities measured are not correlated with distance, implying that it is possible to make accurate density measurements throughout the galaxy without a distance bias. We confirm that ultracompact HII regions are associated with, and possibly embedded in, gas at densities $n(\text{H}_2) \gtrsim 10^5 \text{ cm}^{-3}$. The densities measured in line-of-sight molecular clouds suggest that they consist of low volume filling factor ($f \sim 10^{-2}$) gas at high ($n(\text{H}_2) > 10^4 \text{ cm}^{-3}$) density, which is inconsistent with purely supersonic turbulence and requires high-density clumping greater than typically observed in gravo-turbulent simulations. We observe complex line morphologies that indicate density variations with velocity around UCH II regions, and we classify a subset of the UCH II molecular envelopes as collapsing or expanding. We compare these measurements to Bolocam Galactic Plane Survey 1.1 mm observations, and note that most UCH II regions have 1.1 mm emission consisting of significant (5-70%) free-free emission and are therefore not necessarily dominated by optically thin dust emission as is often assumed when computing clump masses. A comparison of our data with the Mangum et al. (2008) starburst sample shows that the area filling factor of dense ($n(\text{H}_2) \sim 10^5 \text{ cm}^{-3}$) molecular gas in typical starburst galaxies is $\lesssim 0.01$, but in extreme starburst galaxies like Arp 220, is ~ 0.1 , suggesting that Arp 220 is physically similar to an oversized UCH II region.

Subject headings: ISM: HII regions — ISM: molecules — stars: formation

1. INTRODUCTION

Massive stars are known to form preferentially in clustered environments (de Wit et al. 2005). They therefore likely form from “clumps,” collections of gas and dust more dense and compact than Giant Molecular Clouds (GMCs) but larger and more diffuse than typical low-mass protostellar cores. “Clumps” have been observed with masses ranging from $10 - 10^6 M_\odot$ (but more typically $10^2 - 10^3 M_\odot$) and with beam-averaged densities in the range $10^3 \lesssim n(\text{H}_2) \lesssim 10^5 \text{ cm}^{-3}$ and sizes $\sim 1 \text{ pc}$ (e.g., Rosolowsky et al. 2010; Dunham et al. 2010). While giant molecular clouds in the Galaxy have been surveyed (e.g., Jackson et al. 2006), the process by which these clouds condense into clumps and cores and the mechanisms by which they are dispersed are not understood.

It is still not known what sets the final mass of massive stars, but it is thought that they must ignite while still accreting (McKee & Ostriker 2007). Hot O and B stars emitting strongly in the ultraviolet will ionize their surroundings, creating density-bounded H II regions. They progress from hypercompact through ultracompact and compact and finally diffuse H II region phases, during which they either dissociate or blow out their surrounding medium (Churchwell 2002; Keto 2007). The brightest sources in the Galactic plane in both the free-free continuum in the cm-wavelength regime and the dust continuum

in the sub-mm to mm-wavelength regime generally host UCH II regions.

While the gas within UCH II regions is hot and ionized, the surrounding gas is initially molecular. At the interface between the molecular cloud and the ionization front, a photon-dominated or photodissociation region appears (Roshi et al. 2005). Churchwell et al. (2010) observed HCO⁺ towards a sample of UCH II regions and noted both infall and outflow motions in molecular tracers towards these objects. It should be possible to determine whether the UCH II regions still have collapsing envelopes (infall signatures) or only disks (outflow signatures) and thereby determine relative evolutionary states of the regions.

Two centimeter transitions of formaldehyde, o-H₂CO 1₁₀ – 1₁₁ (6 cm) and 2₁₁ – 2₁₂ (2 cm)¹, have been used to measure the density of molecular clouds in massive-star-forming regions (e.g., Dickel et al. 1986; Dickel & Goss 1987), high-latitude Galactic clouds (e.g., Turner et al. 1989), the Galactic Center (e.g., Zylka et al. 1992) starburst galaxies (e.g., Mangum et al. 2008), and molecular clouds in a gravitational lens (e.g., Zeiger & Darling 2010). Studies similar to our own have been performed by Wadiak et al. (1988) and Henkel et al. (1983), in which

¹ All references to H₂CO in this paper, except where otherwise noted, are to the ortho o-H₂CO population, as no para p-H₂CO lines were observed

bright continuum sources were observed in the same transitions with (approximately) beam-matched telescopes at $\sim 2'$ resolution. Our study delves deeper into the spectral line profiles and systematic uncertainties of H_2CO densitometry and is performed at higher spatial resolution than past work.

This paper presents a pilot study as a proof-of-concept for a much larger ongoing survey² towards 400 lines of sight and the methodology applicable to the larger survey.

In section 2 we present the new observations and describe other data sets used in our analysis. Section 3 describes the modeling procedure used to derive density from the H_2CO line observations. Section 4 presents detailed discussion of the modeling and derivation of physical parameters and their uncertainties. Section 5 describes the derived and measured values. Section 6 discusses the larger implications of our results. We conclude with a brief summary of important results.

2. OBSERVATIONS AND DATA

2.1. Source Selection

The observed lines-of-sight included 21 sources selected from the Araya et al. (2002) UCH II sample and 3 from

the Araya et al. (2004) “massive-star forming candidate” sample. The sources were selected primarily on the basis of having been previously observed with Arecibo³ in the $1_{10} - 1_{11}$ transition of H_2CO with the intent of demonstrating the densitometry method within the Galaxy rather than making systematic observations of any source class. Nonetheless, the Araya et al. (2002) sample includes the majority of the bright UCH II regions accessible to Arecibo. Additionally, there are many detected GMCs along the line of sight to these UCH II regions.

The Araya et al. (2004) observations included 15 pointings towards infrared dark cloud (IRDC) candidates and High-Mass Protostellar Object (HMPO) candidates. The sources we selected from this sample include two sources classified as IRDCs based on MSX data and one HMPO candidate. The selection of these sources was arbitrary; we were only able to observe 24 lines-of-sight in our 4 hour observation block. The remaining sources will be discussed in a later paper. The observed lines of sight are listed in Table 1.

Table 1
Measured H_2CO $1_{10} - 1_{11}$ line properties

Source Name ^a	l °	b °	6cm Continuum (Jy)	Peak (Jy)	Center (km s ⁻¹)	FWHM (km s ⁻¹)	RMS (Jy)	Channel Width (km s ⁻¹)
G32.80+0.19 0	0.1904	32.7968	2.18 (0.01)	-0.393 (0.008)	15.39 (0.05)	6.57 (0.06)	0.0049	1.1374
G32.80+0.19 1	0.1904	32.7968	2.18 (0.01)	-0.092 (0.008)	11.45 (0.26)	10.25 (0.65)	0.0049	1.1374
G32.80+0.19 2	0.1904	32.7968	2.18 (0.01)	-0.063 (0.008)	80.63 (0.13)	2.49 (0.36)	0.0049	1.1374
G32.80+0.19 3	0.1904	32.7968	2.18 (0.01)	-0.254 (0.008)	84.61 (0.02)	1.37 (0.06)	0.0049	1.1374
G32.80+0.19 4	0.1904	32.7968	2.18 (0.01)	-0.090 (0.008)	88.66 (0.09)	3.21 (0.31)	0.0049	1.1374
G33.13-0.09 0	-0.0949	33.1297	0.49 (0.00)	-0.192 (0.007)	75.92 (0.05)	3.80 (0.12)	0.0045	1.1374
G33.13-0.09 1	-0.0949	33.1297	0.49 (0.00)	-0.023 (0.007)	81.62 (0.35)	2.49 (0.88)	0.0045	1.1374
G33.13-0.09 2	-0.0949	33.1297	0.49 (0.00)	-0.040 (0.007)	101.50 (0.40)	11.30 (0.80)	0.0045	1.1374
G33.13-0.09 3	-0.0949	33.1297	0.49 (0.00)	-0.039 (0.007)	10.39 (0.08)	2.04 (0.24)	0.0045	1.1374
G33.92+0.11 0	0.1112	33.914	0.83 (0.00)	-0.081 (0.008)	107.28 (0.18)	6.62 (0.34)	0.005	1.1374
G33.92+0.11 1	0.1112	33.914	0.83 (0.00)	-0.079 (0.008)	106.03 (0.06)	2.41 (0.23)	0.005	1.1374
G33.92+0.11 2	0.1112	33.914	0.83 (0.00)	-0.160 (0.030)	57.30 (0.40)	10.60 (0.80)	0.005	1.1374
G34.26+0.15 0	0.1538	34.2572	5.57 (0.01)	-1.828 (0.015)	60.24 (0.01)	3.80 (0.03)	0.0063	1.1374
G34.26+0.15 1	0.1538	34.2572	5.57 (0.01)	-0.160 (0.015)	26.69 (0.08)	1.04 (0.22)	0.0063	1.1374
G34.26+0.15 2	0.1538	34.2572	5.57 (0.01)	-0.099 (0.015)	11.25 (0.19)	2.01 (0.40)	0.0063	1.1374
G34.26+0.15 3	0.1538	34.2572	5.57 (0.01)	-0.126 (0.015)	51.70 (2.00)	4.20 (1.00)	0.0063	1.1374
G34.26+0.15 4	0.1538	34.2572	5.57 (0.01)	-0.047 (0.015)	48.20 (2.00)	1.80 (1.00)	0.0063	1.1374
G35.20-1.74 0	-1.7409	35.1997	5.17 (0.00)	-1.018 (0.008)	43.37 (0.01)	3.67 (0.02)	0.0051	1.1374
G35.20-1.74 1	-1.7409	35.1997	5.17 (0.00)	-0.147 (0.008)	36.67 (0.10)	1.49 (0.27)	0.0051	1.1374
G35.20-1.74 2	-1.7409	35.1997	5.17 (0.00)	-0.324 (0.008)	14.08 (0.01)	0.93 (0.03)	0.0051	1.1374
G35.20-1.74 3	-1.7409	35.1997	5.17 (0.00)	-0.039 (0.008)	50.59 (0.53)	4.92 (1.31)	0.0051	1.1374
G35.57-0.03 0	-0.0306	35.5779	0.47 (0.00)	-0.064 (0.009)	52.10 (0.10)	4.60 (0.30)	0.0053	1.1374
G35.57-0.03 1	-0.0306	35.5779	0.47 (0.00)	-0.021 (0.009)	45.60 (0.30)	1.90 (0.60)	0.0053	1.1374
G35.57-0.03 2	-0.0306	35.5779	0.47 (0.00)	-0.019 (0.009)	57.60 (0.50)	2.90 (0.97)	0.0053	1.1374
G35.57-0.03 3	-0.0306	35.5779	0.47 (0.00)	-0.031 (0.009)	12.80 (0.20)	1.84 (0.41)	0.0053	1.1374
G35.57-0.03 4	-0.0306	35.5779	0.47 (0.00)	-0.031 (0.008)	29.04 (0.11)	0.82 (0.25)	0.0053	1.1374
G35.58+0.07 0	0.0657	35.5801	0.53 (0.01)	-0.146 (0.004)	49.37 (0.21)	5.33 (0.34)	0.0048	1.1374
G35.58+0.07 1	0.0657	35.5801	0.53 (0.01)	-0.049 (0.013)	53.13 (0.25)	2.98 (0.64)	0.0048	1.1374
G35.58+0.07 2	0.0657	35.5801	0.53 (0.01)	-0.025 (0.004)	58.12 (0.29)	3.63 (0.74)	0.0048	1.1374
G35.58+0.07 3	0.0657	35.5801	0.53 (0.01)	-0.034 (0.004)	13.24 (0.17)	2.80 (0.39)	0.0048	1.1374
G37.87-0.40 0	-0.3993	37.873	4.40 (0.01)	-0.531 (0.006)	60.23 (0.11)	8.73 (0.35)	0.0069	1.1374
G37.87-0.40 1	-0.3993	37.873	4.40 (0.01)	-0.124 (0.014)	53.27 (0.19)	4.03 (0.46)	0.0069	1.1374
G37.87-0.40 2	-0.3993	37.873	4.40 (0.01)	-0.356 (0.019)	65.13 (0.04)	2.74 (0.15)	0.0069	1.1374
G37.87-0.40 3	-0.3993	37.873	4.40 (0.01)	-0.324 (0.045)	72.18 (0.04)	1.35 (0.14)	0.0069	1.1374
G37.87-0.40 4	-0.3993	37.873	4.40 (0.01)	-0.424 (0.013)	73.97 (0.13)	3.01 (0.22)	0.0069	1.1374
G37.87-0.40 5	-0.3993	37.873	4.40 (0.01)	-0.185 (0.012)	79.98 (0.06)	1.80 (0.14)	0.0069	1.1374
G37.87-0.40 6	-0.3993	37.873	4.40 (0.01)	-0.114 (0.015)	91.96 (0.08)	1.21 (0.18)	0.0069	1.1374

² GBT project code GBT10B-019

³ The Arecibo Observatory is part of the National Astronomy and Ionosphere Center, which is operated by Cornell University under a cooperative agreement with the National Science Foundation.

Table 1
Measured H₂CO 1₁₀ – 1₁₁ line properties

G37.87-0.40 7	-0.3993	37.873	4.40 (0.01)	-0.175 (0.012)	14.32 (0.14)	2.94 (0.20)	0.0069	1.1374
G37.87-0.40 8	-0.3993	37.873	4.40 (0.01)	-0.072 (0.022)	13.16 (0.10)	0.87 (0.32)	0.0069	1.1374
G37.87-0.40 9	-0.3993	37.873	4.40 (0.01)	-0.137 (0.012)	20.54 (0.06)	1.37 (0.14)	0.0069	1.1374
G43.89-0.78 0	-0.7838	43.8892	0.66 (0.00)	-0.181 (0.004)	54.86 (0.02)	2.19 (0.06)	0.0032	1.1374
G43.89-0.78 1	-0.7838	43.8892	0.66 (0.00)	-0.020 (0.002)	50.55 (0.59)	15.90 (1.20)	0.0032	1.1374
G45.07+0.13 0	0.1323	45.0711	0.47 (0.00)	-0.056 (0.006)	57.49 (0.10)	4.24 (0.23)	0.0035	1.1374
G45.07+0.13 1	0.1323	45.0711	0.47 (0.00)	-0.036 (0.006)	65.44 (0.15)	4.09 (0.34)	0.0035	1.1374
G45.12+0.13 0	0.1326	45.1223	4.28 (0.01)	-0.188 (0.006)	55.70 (0.12)	3.32 (0.24)	0.0065	1.1374
G45.12+0.13 1	0.1326	45.1223	4.28 (0.01)	-0.154 (0.009)	59.40 (0.13)	3.11 (0.33)	0.0065	1.1374
G45.12+0.13 2	0.1326	45.1223	4.28 (0.01)	-0.200 (0.010)	24.86 (0.03)	1.68 (0.08)	0.0065	1.1374
G45.12+0.13 3	0.1326	45.1223	4.28 (0.01)	-0.027 (0.004)	65.53 (0.82)	7.23 (2.03)	0.0065	1.1374
G45.45+0.06 0	0.0593	45.4548	4.77 (0.01)	-1.347 (0.018)	59.58 (0.02)	3.18 (0.05)	0.0063	1.1374
G45.45+0.06 1	0.0593	45.4548	4.77 (0.01)	-0.123 (0.040)	55.34 (0.38)	3.15 (0.38)	0.0063	1.1374
G45.45+0.06 2	0.0593	45.4548	4.77 (0.01)	-0.056 (0.005)	25.02 (0.12)	2.82 (0.28)	0.0063	1.1374
G45.47+0.05 0	0.0455	45.4655	0.75 (0.00)	-0.274 (0.003)	60.62 (0.03)	6.59 (0.07)	0.0039	1.1374
G45.47+0.05 1	0.0455	45.4655	0.75 (0.00)	-0.017 (0.004)	25.55 (0.23)	2.18 (0.55)	0.0039	1.1374
G48.61+0.02 0	0.0229	48.6055	1.01 (0.00)	-0.067 (0.003)	18.08 (0.09)	4.97 (0.22)	0.0035	1.1374
G48.61+0.02 1	0.0229	48.6055	1.01 (0.00)	-0.024 (0.005)	6.08 (0.13)	1.20 (0.31)	0.0035	1.1374
G48.61+0.02 2	0.0229	48.6055	1.01 (0.00)	-0.018 (0.003)	53.73 (0.33)	4.72 (0.79)	0.0035	1.1374
G50.32+0.68 0	0.6761	50.3153	0.24 (0.00)	-0.011 (0.003)	26.28 (0.40)	3.32 (0.94)	0.0031	1.1374
G60.88-0.13 0	-0.1285	60.8826	0.66 (0.01)	-0.093 (0.009)	22.60 (0.15)	3.24 (0.35)	0.0096	1.1374
G61.48+0.09 0	0.0893	61.4769	6.16 (0.01)	-0.531 (0.009)	21.45 (0.02)	2.81 (0.06)	0.0084	1.1374
G69.54-0.98 0	-0.9759	69.5398	0.28 (0.01)	-0.280 (0.006)	10.65 (0.05)	4.55 (0.11)	0.0076	1.1374
G70.29+1.60 0	1.6006	70.2927	4.37 (0.13)	-0.372 (0.008)	-21.74 (0.07)	3.92 (0.15)	0.0108	1.1374
G70.29+1.60 1	1.6006	70.2927	4.37 (0.13)	-0.050 (0.007)	-27.17 (0.58)	4.86 (1.33)	0.0108	1.1374
G70.33+1.59 0	1.589	70.3296	2.21 (0.01)	-1.201 (0.007)	-21.24 (0.01)	3.65 (0.03)	0.0115	1.1374
IRAS 20051+3435 0	0.2088	32.4662	0.00 (0.01)	-0.019 (0.001)	10.77 (0.07)	3.60 (0.18)	0.00071	2.2747
G41.74+0.10 0	0.0975	41.7415	0.34 (0.00)	-0.062 (0.004)	14.60 (0.09)	2.56 (0.26)	0.0033	1.1374
G41.74+0.10 1	0.0975	41.7415	0.34 (0.00)	-0.020 (0.004)	10.99 (0.29)	2.52 (0.71)	0.0033	1.1374
G41.74+0.10 2	0.0975	41.7415	0.34 (0.00)	-0.066 (0.004)	34.25 (0.05)	1.63 (0.13)	0.0033	1.1374
G41.74+0.10 3	0.0975	41.7415	0.34 (0.00)	-0.022 (0.005)	56.61 (0.13)	1.15 (0.32)	0.0033	1.1374
G41.74+0.10 4	0.0975	41.7415	0.34 (0.00)	-0.043 (0.005)	17.57 (0.07)	1.13 (0.18)	0.0033	1.1374
IRDC 1923+13 0	-0.4972	48.9325	0.40 (0.00)	-0.011 (0.001)	50.20 (0.08)	1.83 (0.19)	0.0008	0.7582
IRDC 1923+13 1	-0.4972	48.9325	0.40 (0.00)	-0.009 (0.001)	57.56 (0.09)	2.57 (0.22)	0.0008	0.7582
IRDC 1923+13 2	-0.4972	48.9325	0.40 (0.00)	-0.005 (0.001)	47.32 (0.20)	2.11 (0.51)	0.0008	0.7582
IRDC 1916+11 0	-0.2923	45.666	0.00 (0.01)	-0.005 (0.001)	25.94 (0.17)	2.53 (0.41)	0.00083	0.7582
IRDC 1916+11 1	-0.2923	45.666	0.00 (0.01)	-0.013 (0.001)	55.91 (0.13)	6.21 (0.34)	0.00083	0.7582
IRDC 1916+11 2	-0.2923	45.666	0.00 (0.01)	-0.003 (0.001)	48.85 (0.48)	3.58 (1.13)	0.00083	0.7582

^a Sources are labeled by the line-of-sight followed by the number of the component identified, indexed from zero. The components do not follow a particular order, but are uniquely identifiable by their velocity, width, and amplitude.

Table 2
Measured H₂CO 2₁₁ – 2₁₂ line properties

Source Name	2cm Continuum (Jy)	Peak ^a (Jy)	Center (km s ⁻¹)	FWHM (km s ⁻¹)	RMS ^b (Jy)
G32.80+0.19 0	3.68 (0.02)	-0.519 (0.032)	15.65 (0.03)	5.72 (0.08)	0.0038
G32.80+0.19 1	3.68 (0.02)	-0.076 (0.019)	11.90 (1.18)	8.17 (0.98)	0.0038
G32.80+0.19 2	3.68 (0.02)	-0.016 (0.001)	80.47 (0.14)	4.35 (0.36)	0.0038
G32.80+0.19 3	3.68 (0.02)	-0.065 (0.002)	84.96 (0.02)	1.29 (0.05)	0.0038
G32.80+0.19 4	3.68 (0.02)	-0.026 (0.001)	88.83 (0.06)	2.31 (0.14)	0.0038
G33.13-0.09 0	0.47 (0.02)	-0.224 (0.003)	76.17 (0.02)	3.31 (0.05)	0.003
G33.13-0.09 1	0.47 (0.02)	0.000 (0.000)	0.00 (0.00)	0.00 (0.00)	0.003
G33.13-0.09 2	0.47 (0.02)	0.000 (0.000)	0.00 (0.00)	0.00 (0.00)	0.003
G33.13-0.09 3	0.47 (0.02)	0.000 (0.000)	0.00 (0.00)	0.00 (0.00)	0.003
G33.92+0.11 0	0.87 (0.02)	-0.086 (0.003)	106.43 (0.03)	2.17 (0.09)	0.0032
G33.92+0.11 1	0.87 (0.02)	-0.069 (0.002)	108.83 (0.11)	6.82 (0.16)	0.0032
G33.92+0.11 2	0.87 (0.02)	0.000 (0.000)	0.00 (0.00)	0.00 (0.00)	0.0032
G34.26+0.15 0	5.89 (0.02)	-1.356 (0.006)	60.99 (0.01)	3.96 (0.02)	0.0051
G34.26+0.15 1	5.89 (0.02)	-0.046 (0.003)	27.11 (0.04)	1.03 (0.09)	0.0051
G34.26+0.15 2	5.89 (0.02)	-0.018 (0.002)	11.23 (0.16)	3.19 (0.38)	0.0051
G34.26+0.15 3	5.89 (0.02)	-0.025 (0.004)	52.82 (0.58)	6.34 (1.53)	0.0051
G34.26+0.15 4	5.89 (0.02)	-0.018 (0.007)	47.05 (0.47)	2.47 (1.15)	0.0051
G35.20-1.74 0	5.98 (0.03)	-0.482 (0.004)	43.38 (0.02)	3.71 (0.04)	0.0055
G35.20-1.74 1	5.98 (0.03)	-0.028 (0.005)	37.91 (0.32)	3.46 (0.76)	0.0055
G35.20-1.74 2	5.98 (0.03)	-0.056 (0.003)	14.18 (0.02)	1.00 (0.05)	0.0055
G35.20-1.74 3	5.98 (0.03)	0.000 (0.000)	0.00 (0.00)	0.00 (0.00)	0.0055
G35.57-0.03 0	0.32 (0.15)	-0.075 (0.003)	52.14 (0.09)	4.39 (0.21)	0.0046
G35.57-0.03 1	0.32 (0.15)	-0.015 (0.006)	47.39 (0.25)	1.31 (0.60)	0.0046

Table 2
Measured H₂CO 2₁₁ – 2₁₂ line properties

G35.57-0.03 2	0.32 (0.15)	0.000 (0.000)	0.00 (0.00)	0.00 (0.00)	0.0046
G35.57-0.03 3	0.32 (0.15)	0.000 (0.000)	0.00 (0.00)	0.00 (0.00)	0.0046
G35.57-0.03 4	0.32 (0.15)	-0.024 (0.008)	29.25 (0.11)	0.43 (0.15)	0.0046
G35.58+0.07 0	0.23 (0.09)	-0.106 (0.002)	49.21 (0.06)	5.00 (0.14)	0.0031
G35.58+0.07 1	0.23 (0.09)	0.000 (0.004)	0.00 (0.00)	0.00 (0.00)	0.0031
G35.58+0.07 2	0.23 (0.09)	0.000 (0.004)	0.00 (0.00)	0.00 (0.00)	0.0031
G35.58+0.07 3	0.23 (0.09)	0.000 (0.004)	0.00 (0.00)	0.00 (0.00)	0.0031
G37.87-0.40 0	3.73 (0.02)	-0.221 (0.003)	59.99 (0.12)	8.53 (0.14)	0.0048
G37.87-0.40 1	3.73 (0.02)	-0.045 (0.007)	54.55 (0.25)	5.99 (0.34)	0.0048
G37.87-0.40 2	3.73 (0.02)	-0.036 (0.007)	65.06 (0.11)	2.57 (0.45)	0.0048
G37.87-0.40 3	3.73 (0.02)	-0.053 (0.003)	72.44 (0.05)	1.37 (0.08)	0.0048
G37.87-0.40 4	3.73 (0.02)	-0.047 (0.002)	74.25 (0.07)	2.07 (0.18)	0.0048
G37.87-0.40 5	3.73 (0.02)	-0.016 (0.001)	80.04 (0.03)	1.28 (0.07)	0.0048
G37.87-0.40 6	3.73 (0.02)	-0.010 (0.002)	91.99 (0.12)	1.60 (0.28)	0.0048
G37.87-0.40 7	3.73 (0.02)	-0.026 (0.002)	14.89 (0.12)	1.40 (0.20)	0.0048
G37.87-0.40 8	3.73 (0.02)	-0.017 (0.002)	13.29 (0.19)	1.52 (0.34)	0.0048
G37.87-0.40 9	3.73 (0.02)	-0.017 (0.001)	20.52 (0.10)	3.09 (0.23)	0.0048
G43.89-0.78 0	0.53 (0.02)	-0.059 (0.004)	54.61 (0.08)	2.85 (0.23)	0.003
G43.89-0.78 1	0.53 (0.02)	-0.015 (0.002)	49.59 (0.94)	14.49 (1.69)	0.003
G45.07+0.13 0	0.79 (0.07)	-0.073 (0.003)	57.18 (0.08)	3.45 (0.18)	0.0029
G45.07+0.13 1	0.79 (0.07)	-0.011 (0.003)	65.67 (0.42)	3.46 (0.98)	0.0029
G45.12+0.13 0	5.20 (0.20)	-0.086 (0.002)	56.21 (0.11)	5.22 (0.21)	0.0044
G45.12+0.13 1	5.20 (0.20)	-0.059 (0.005)	59.70 (0.06)	2.42 (0.16)	0.0044
G45.12+0.13 2	5.20 (0.20)	-0.047 (0.002)	25.14 (0.04)	1.55 (0.09)	0.0044
G45.12+0.13 3	5.20 (0.20)	-0.021 (0.001)	64.68 (0.39)	8.15 (0.87)	0.0044
G45.45+0.06 0	3.16 (0.02)	-0.260 (0.003)	59.58 (0.01)	2.06 (0.03)	0.0043
G45.45+0.06 1	3.16 (0.02)	-0.042 (0.002)	57.90 (0.14)	9.40 (0.31)	0.0043
G45.45+0.06 2	3.16 (0.02)	0.000 (0.000)	0.00 (0.00)	0.00 (0.00)	0.0043
G45.47+0.05 0	0.38 (0.02)	-0.124 (0.003)	61.67 (0.07)	5.85 (0.17)	0.0049
G45.47+0.05 1	0.38 (0.02)	-0.000 (0.007)	0.00 (0.00)	0.00 (0.00)	0.0049
G48.61+0.02 0	0.41 (0.02)	-0.022 (0.003)	18.50 (0.25)	4.39 (0.59)	0.0033
G48.61+0.02 1	0.41 (0.02)	-0.000 (0.000)	0.00 (0.00)	0.00 (0.00)	0.0033
G48.61+0.02 2	0.41 (0.02)	-0.005 (0.002)	52.50 (1.25)	7.47 (2.94)	0.0033
G50.32+0.68 0	0.16 (0.02)	-0.011 (0.003)	26.21 (0.44)	3.10 (1.03)	0.0036
G60.88-0.13 0	0.29 (0.02)	-0.016 (0.003)	21.63 (0.21)	2.47 (0.50)	0.003
G61.48+0.09 0	3.42 (0.02)	-0.300 (0.004)	21.40 (0.02)	2.39 (0.04)	0.0037
G69.54-0.98 0	0.23 (0.02)	-0.220 (0.002)	9.97 (0.03)	5.81 (0.08)	0.0031
G70.29+1.60 0	6.21 (0.02)	-0.159 (0.003)	-23.52 (0.06)	5.36 (0.13)	0.0046
G70.29+1.60 1	6.21 (0.02)	-0.000 (0.000)	-0.00 (0.00)	0.00 (0.00)	0.0046
G70.33+1.59 0	2.68 (0.02)	-1.081 (0.005)	-21.17 (0.01)	2.95 (0.01)	0.0038
IRAS 20051+3435 0	0.00 (0.02)	-0.016 (0.003)	11.51 (0.37)	4.14 (0.88)	0.0032
G41.74+0.10 0	0.28 (0.02)	-0.014 (0.002)	14.36 (0.34)	3.80 (0.80)	0.0032
G41.74+0.10 1	0.28 (0.02)	0.000 (0.004)	0.00 (0.00)	0.00 (0.00)	0.0032
G41.74+0.10 2	0.28 (0.02)	0.000 (0.004)	0.00 (0.00)	0.00 (0.00)	0.0032
G41.74+0.10 3	0.28 (0.02)	0.000 (0.004)	0.00 (0.00)	0.00 (0.00)	0.0032
G41.74+0.10 4	0.28 (0.02)	0.000 (0.004)	0.00 (0.00)	0.00 (0.00)	0.0032
IRDC 1923+13 0	0.00 (0.02)	0.000 (0.000)	0.00 (0.00)	0.00 (0.00)	0.0032
IRDC 1923+13 1	0.00 (0.02)	0.000 (0.000)	0.00 (0.00)	0.00 (0.00)	0.0032
IRDC 1923+13 2	0.00 (0.02)	0.000 (0.000)	0.00 (0.00)	0.00 (0.00)	0.0032
IRDC 1916+11 0	0.00 (0.02)	0.000 (0.000)	0.00 (0.00)	0.00 (0.00)	0.0048
IRDC 1916+11 1	0.00 (0.02)	0.000 (0.000)	0.00 (0.00)	0.00 (0.00)	0.0048
IRDC 1916+11 2	0.00 (0.02)	0.000 (0.000)	0.00 (0.00)	0.00 (0.00)	0.0048

^a The Upper Limit Flag is 1 when the measurement indicated is a 3 – σ upper limit on the 2₁₁ – 2₁₂ line depth when there is a corresponding 1₁₀ – 1₁₁ line detection.

^b RMS in 1.011 km s⁻¹ channels.

Table 3
Distance, BGPS 1.1 mm, and other properties

Source Name	Distance (kpc)	Galactocentric Distance (kpc)	KDA ^a Resolution	S _{1.1mm} (Jy)	Source Type	H ₂ CO Spectrum Type	Scenario ^b
G32.80+0.19 0	12.9	7.4	far	6.94	UCHII	red gradient	2+3
G32.80+0.19 1	13.1	7.6	far	6.94	UCHII	envelope	2+3
G32.80+0.19 2	9.4	5.1	far	6.94	GMC	-	2+3
G32.80+0.19 3	9.2	5.0	far	6.94	GMC	-	2+3
G32.80+0.19 4	9.0	4.9	far	6.94	GMC	-	2+3
G33.13-0.09 0	9.6	5.2	far	2.26	UCHII	red gradient	2
G33.13-0.09 1	9.3	5.1	far	2.26	GMC	envelope	2
G33.13-0.09 2	7.1	4.7	tangent	2.26	GMC	-	2
G33.13-0.09 3	0.9	7.6	near	2.26	GMC	-	2

Table 3
Distance, BGPS 1.1 mm, and other properties

G33.92+0.11 0	7.0	4.6	tangent	3.86	UCHII	red gradient	2
G33.92+0.11 1	7.0	4.6	tangent	3.86	UCHII	envelope	2
G33.92+0.11 2	3.6	5.8	near	3.86	GMC	-	2
G34.26+0.15 0	3.6	5.7	near	35.69	UCHII	red gradient	2
G34.26+0.15 1	1.9	6.9	near	35.69	GMC	-	2
G34.26+0.15 2	1.0	7.6	near	35.69	GMC	-	2
G34.26+0.15 3	3.6	6.0	near	35.69	GMC	envelope	2
G34.26+0.15 4	3.6	6.1	near	35.69	GMC	-	2
G35.20-1.74 0	2.8	6.3	near	-	UCHII	single	4
G35.20-1.74 1	2.5	6.5	near	-	GMC	-	4
G35.20-1.74 2	1.1	7.5	near	-	GMC	-	4
G35.20-1.74 3	3.2	6.1	near	-	GMC	-	4
G35.57-0.03 0	10.3	6.0	far	2.57	UCHII	single	2+3
G35.57-0.03 1	10.7	6.2	far	2.57	GMC	-	2+3
G35.57-0.03 2	3.6	5.9	near	2.57	GMC	-	2+3
G35.57-0.03 3	1.1	7.6	near	2.57	GMC	-	2+3
G35.57-0.03 4	2.0	6.8	near	2.57	GMC	-	2+3
G35.58+0.07 0	10.5	6.1	far	1.44	UCHII	blue gradient	2
G35.58+0.07 1	10.3	6.0	far	1.44	UCHII	-	2
G35.58+0.07 2	3.6	5.8	near	1.44	GMC	-	2
G35.58+0.07 3	1.1	7.5	near	1.44	GMC	-	2
G37.87-0.40 0	9.4	5.9	far	4.14	UCHII	blue gradient	1
G37.87-0.40 1	9.8	6.1	far	4.14	UCHII	blue gradient	1
G37.87-0.40 2	9.2	5.7	far	4.14	UCHII	blue gradient	1
G37.87-0.40 3	8.7	5.6	far	4.14	GMC	-	1
G37.87-0.40 4	8.6	5.5	far	4.14	GMC	-	1
G37.87-0.40 5	8.1	5.4	far	4.14	GMC	-	1
G37.87-0.40 6	6.6	5.1	tangent	4.14	GMC	-	1
G37.87-0.40 7	1.2	7.5	near	4.14	GMC	-	1
G37.87-0.40 8	1.1	7.6	near	4.14	GMC	-	1
G37.87-0.40 9	1.5	7.2	near	4.14	GMC	-	1
G43.89-0.78 0	8.3	6.2	far	-	UCHII	blue gradient	3
G43.89-0.78 1	8.6	6.3	far	-	GMC	envelope	3
G45.07+0.13 0	7.6	6.2	far	4.26	UCHII	single	2
G45.07+0.13 1	6.5	6.0	far	4.26	GMC	-	2
G45.12+0.13 0	7.4	6.2	far	6.78	UCHII	other	1
G45.12+0.13 1	7.4	6.1	far	6.78	UCHII	envelope	1
G45.12+0.13 2	1.9	7.2	near	6.78	GMC	-	1
G45.12+0.13 3	7.4	6.0	far	6.78	GMC	envelope	1
G45.45+0.06 0	7.2	6.1	far	3.71	UCHII	blue gradient	2
G45.45+0.06 1	7.6	6.2	far	3.71	GMC	envelope	2
G45.45+0.06 2	1.9	7.2	near	3.71	GMC	-	2
G45.47+0.05 0	7.1	6.1	far	3.34	UCHII	red gradient	1+2+3
G45.47+0.05 1	1.9	7.2	near	3.34	GMC	-	1+2+3
G48.61+0.02 0	9.6	7.5	far	2.20	UCHII	red gradient	2+3
G48.61+0.02 1	0.7	8.0	near	2.20	GMC	-	2+3
G48.61+0.02 2	6.5	6.4	far	2.20	GMC	-	2+3
G50.32+0.68 0	2.1	7.2	near	-	UCHII	-	1
G60.88-0.13 0	2.8	7.4	near	4.90	UCHII	limit	2
G61.48+0.09 0	5.2	7.5	far	7.86	UCHII	single	4
G69.54-0.98 0	2.57	7.9	tangent	-	UCHII	thick	4+5
G70.29+1.60 0	7.3	9.1	far	-	UCHII	blue gradient	2
G70.29+1.60 1	7.8	9.3	far	-	GMC	envelope	2
G70.33+1.59 0	7.3	9.1	far	-	UCHII	single	1+2
IRAS 20051+3435 0	2.6	7.6	tangent	-	GMC	limit	-1
G41.74+0.10 0	11.3	7.6	far	0.56	UCHII	limit	-1
G41.74+0.10 1	11.6	7.7	far	0.56	UCHII	-	-1
G41.74+0.10 2	2.4	6.8	near	0.56	GMC	-	-1
G41.74+0.10 3	3.8	6.1	near	0.56	GMC	-	-1
G41.74+0.10 4	11.2	7.4	far	0.56	UCHII	-	-1
IRDC 1923+13 0	4.2	6.5	near	-	GMC	limit	-1
IRDC 1923+13 1	5.5	6.3	tangent	-	GMC	-	-1
IRDC 1923+13 2	3.8	6.6	near	-	GMC	-	-1
IRDC 1916+11 0	2.0	7.2	near	-	GMC	limit	-1
IRDC 1916+11 1	4.2	6.2	near	-	GMC	-	-1
IRDC 1916+11 2	3.6	6.4	near	-	GMC	-	-1

^a The Kinematic Distance Ambiguity described in Section 5.3.

^b Scenario or scenarios most likely to be consistent with the observed spectrum, as described in Section 6.3. In some cases, the spectrum was consistent with multiple scenarios or some blend of multiple scenarios. In others, the source could not be classified, in which case it is marked with -1 in this column.

Table 4
Inferred H₂CO line properties

Source Name	τ_{1-1}	τ_{1-1} (FFC)	τ_{2-2}	τ_{2-2} (FFC)	2-2 Upper Limit Flag	2cm Area ^a '' ²	6cm Area ^a '' ²	FFC Error
G32.80+0.19 0	0.18 (0.055)	0.2 (0.059)	0.12 (0.024)	0.15 (0.031)	0	88.0	226.2	0.1
G32.80+0.19 1	0.04 (0.013)	0.043 (0.013)	0.016 (0.0051)	0.021 (0.0065)	0	88.0	226.2	0.1
G32.80+0.19 2	0.027 (0.0089)	0.029 (0.0095)	0.0033 (0.00069)	0.0042 (0.00088)	0	88.0	226.2	0.1
G32.80+0.19 3	0.11 (0.035)	0.12 (0.037)	0.014 (0.0028)	0.018 (0.0035)	0	88.0	226.2	0.1
G32.80+0.19 4	0.039 (0.012)	0.042 (0.013)	0.0055 (0.0011)	0.0071 (0.0014)	0	88.0	226.2	0.1
G33.13-0.09 0	0.34 (0.1)	0.49 (0.15)	0.16 (0.032)	0.63 (0.12)	0	33.5	33.5	0.2
G33.13-0.09 1	0.035 (0.015)	0.047 (0.02)	0 (0.0059)	0 (0.0031)	1	33.5	33.5	0.2
G33.13-0.09 2	0.062 (0.022)	0.084 (0.029)	0 (0.0059)	0 (0.0031)	1	33.5	33.5	0.2
G33.13-0.09 3	0.061 (0.021)	0.082 (0.028)	0 (0.0059)	0 (0.0031)	1	33.5	33.5	0.2
G33.92+0.11 0	0.084 (0.027)	0.1 (0.031)	0.045 (0.0091)	0.094 (0.018)	0	214.0	214.0	0.2
G33.92+0.11 1	0.082 (0.026)	0.098 (0.031)	0.036 (0.0072)	0.075 (0.014)	0	214.0	214.0	0.2
G33.92+0.11 2	0.17 (0.062)	0.21 (0.074)	0 (0.0049)	0 (0.0031)	1	214.0	214.0	0.2
G34.26+0.15 0	0.38 (0.12)	0.4 (0.12)	0.22 (0.043)	0.26 (0.052)	0	10.9	10.9	0.2
G34.26+0.15 1	0.028 (0.0089)	0.029 (0.0092)	0.0067 (0.0014)	0.0079 (0.0017)	0	10.9	10.9	0.2
G34.26+0.15 2	0.017 (0.0059)	0.018 (0.006)	0.0026 (0.00059)	0.0031 (0.0007)	0	10.9	10.9	0.2
G34.26+0.15 3	0.022 (0.0072)	0.023 (0.0074)	0.0036 (0.00092)	0.0043 (0.0011)	0	10.9	10.9	0.2
G34.26+0.15 4	0.0082 (0.0036)	0.0085 (0.0037)	0.0026 (0.0011)	0.003 (0.0013)	0	10.9	10.9	0.2
G35.20-1.74 0	0.21 (0.063)	0.22 (0.066)	0.071 (0.014)	0.084 (0.017)	0	39.5	39.5	0.2
G35.20-1.74 1	0.028 (0.0085)	0.029 (0.0088)	0.0039 (0.0011)	0.0046 (0.0013)	0	39.5	39.5	0.2
G35.20-1.74 2	0.063 (0.019)	0.065 (0.019)	0.008 (0.0017)	0.0095 (0.0019)	0	39.5	39.5	0.2
G35.20-1.74 3	0.0073 (0.0027)	0.0075 (0.0028)	0 (0.0023)	0 (0.0031)	1	39.5	39.5	0.2
G35.57-0.03 0	0.11 (0.035)	0.15 (0.049)	0.056 (0.011)	0.26 (0.054)	0	6.7	6.7	0.1
G35.57-0.03 1	0.034 (0.018)	0.046 (0.024)	0.011 (0.0047)	0.047 (0.02)	0	6.7	6.7	0.1
G35.57-0.03 2	0.03 (0.017)	0.042 (0.023)	0 (0.0099)	0 (0.019)	1	6.7	6.7	0.1
G35.57-0.03 3	0.05 (0.021)	0.069 (0.029)	0 (0.0099)	0 (0.019)	1	6.7	6.7	0.1
G35.57-0.03 4	0.051 (0.02)	0.069 (0.028)	0.017 (0.0065)	0.077 (0.029)	0	6.7	6.7	0.1
G35.58+0.07 0	0.24 (0.071)	0.32 (0.097)	0.085 (0.017)	0.61 (0.12)	0	2.1	2.1	0.2
G35.58+0.07 1	0.072 (0.029)	0.096 (0.038)	0 (0.0072)	0 (0.019)	1	2.1	2.1	0.2
G35.58+0.07 2	0.037 (0.012)	0.049 (0.016)	0 (0.0072)	0 (0.019)	1	2.1	2.1	0.2
G35.58+0.07 3	0.05 (0.016)	0.066 (0.021)	0 (0.0072)	0 (0.01)	1	2.1	2.1	0.2
G37.87-0.40 0	0.12 (0.037)	0.13 (0.038)	0.047 (0.0095)	0.061 (0.012)	0	27.5	170.9	0.2
G37.87-0.40 1	0.028 (0.0089)	0.029 (0.0092)	0.0095 (0.0024)	0.012 (0.0031)	0	27.5	170.9	0.2
G37.87-0.40 2	0.081 (0.025)	0.084 (0.026)	0.0075 (0.0021)	0.0096 (0.0027)	0	27.5	170.9	0.2
G37.87-0.40 3	0.074 (0.024)	0.076 (0.025)	0.011 (0.0023)	0.014 (0.003)	0	27.5	170.9	0.2
G37.87-0.40 4	0.097 (0.029)	0.1 (0.03)	0.0098 (0.002)	0.013 (0.0026)	0	27.5	170.9	0.2
G37.87-0.40 5	0.041 (0.013)	0.043 (0.013)	0.0033 (0.00068)	0.0043 (0.00087)	0	27.5	170.9	0.2
G37.87-0.40 6	0.025 (0.0083)	0.026 (0.0086)	0.0021 (0.00052)	0.0026 (0.00066)	0	27.5	170.9	0.2
G37.87-0.40 7	0.039 (0.012)	0.04 (0.012)	0.0054 (0.0012)	0.0069 (0.0015)	0	27.5	170.9	0.2
G37.87-0.40 8	0.016 (0.0069)	0.016 (0.0071)	0.0035 (0.00081)	0.0046 (0.001)	0	27.5	170.9	0.2
G37.87-0.40 9	0.03 (0.0095)	0.031 (0.0098)	0.0035 (0.00073)	0.0045 (0.00094)	0	27.5	170.9	0.2
G43.89-0.78 0	0.25 (0.074)	0.32 (0.096)	0.037 (0.0078)	0.12 (0.024)	0	13.5	13.5	0.1
G43.89-0.78 1	0.025 (0.0077)	0.031 (0.0097)	0.0097 (0.0022)	0.029 (0.0067)	0	13.5	13.5	0.1
G45.07+0.13 0	0.092 (0.029)	0.13 (0.04)	0.04 (0.0081)	0.096 (0.02)	0	2.5	2.5	0.2
G45.07+0.13 1	0.058 (0.02)	0.08 (0.027)	0.0061 (0.0019)	0.014 (0.0045)	0	2.5	2.5	0.2
G45.12+0.13 0	0.043 (0.013)	0.045 (0.013)	0.014 (0.0028)	0.017 (0.0033)	0	15.4	516.6	0.2
G45.12+0.13 1	0.035 (0.011)	0.036 (0.011)	0.0095 (0.002)	0.011 (0.0025)	0	15.4	516.6	0.2
G45.12+0.13 2	0.046 (0.014)	0.048 (0.014)	0.0075 (0.0015)	0.009 (0.0019)	0	15.4	516.6	0.2
G45.12+0.13 3	0.006 (0.002)	0.0062 (0.0021)	0.0033 (0.00068)	0.004 (0.00082)	0	15.4	516.6	0.2
G45.45+0.06 0	0.32 (0.096)	0.32 (0.095)	0.063 (0.013)	0.069 (0.012)	0	1963.0	1963.0	0.2
G45.45+0.06 1	0.025 (0.011)	0.026 (0.011)	0.01 (0.0021)	0.011 (0.0019)	0	1963.0	1963.0	0.2
G45.45+0.06 2	0.011 (0.0036)	0.012 (0.0035)	0 (0.0031)	0 (0.01)	1	1963.0	1963.0	0.2
G45.47+0.05 0	0.35 (0.11)	0.45 (0.14)	0.089 (0.018)	0.39 (0.079)	0	3.0	3.0	0.2
G45.47+0.05 1	0.018 (0.0068)	0.023 (0.0084)	0 (0.01)	0 (0.01)	1	3.0	3.0	0.2
G48.61+0.02 0	0.058 (0.018)	0.068 (0.021)	0.015 (0.0034)	0.053 (0.012)	0	25.5	25.5	0.2
G48.61+0.02 1	0.02 (0.0075)	0.023 (0.0088)	0 (0.0067)	0 (0.0026)	1	25.5	25.5	0.2
G48.61+0.02 2	0.016 (0.0052)	0.018 (0.0061)	0.0033 (0.0013)	0.012 (0.0046)	0	25.5	25.5	0.2
G50.32+0.68 0	0.027 (0.01)	0.045 (0.017)	0.0089 (0.0031)	0.058 (0.019)	0	108.0	108.0	0.2
G60.88-0.13 0	0.12 (0.037)	0.14 (0.043)	0.011 (0.0031)	0.031 (0.0071)	0	615.0	615.0	0.2
G61.48+0.09 0	0.088 (0.026)	0.09 (0.027)	0.069 (0.014)	0.088 (0.017)	0	355.0	355.0	0.2
G69.54-0.98 0	0.98 (0.29)	5.7 (1.7)	0.18 (0.037)	2.9 (0.57)	0	0.5	0.5	0.2
G70.29+1.60 0	0.086 (0.026)	0.089 (0.027)	0.022 (0.0044)	0.026 (0.0052)	0	52.8	52.8	0.1
G70.29+1.60 1	0.011 (0.0037)	0.012 (0.0038)	0 (0.0019)	0 (0.0026)	1	52.8	52.8	0.1
G70.33+1.59 0	0.7 (0.21)	0.78 (0.24)	0.34 (0.068)	0.52 (0.1)	0	16.4	16.4	0.1
IRAS 20051+3435 0	0.12 (0.036)	0.13 (0.014)	0.015 (0.0041)	0.016 (0.0034)	0	2747.75	2747.75	0.0
G41.74+0.10 0	0.13 (0.04)	0.2 (0.06)	0.01 (0.0027)	0.045 (0.012)	0	75.2	75.2	0.2
G41.74+0.10 1	0.04 (0.014)	0.06 (0.021)	0 (0.0071)	0 (0.0026)	1	75.2	75.2	0.2
G41.74+0.10 2	0.14 (0.043)	0.21 (0.065)	0 (0.0071)	0 (0.0026)	1	75.2	75.2	0.2
G41.74+0.10 3	0.045 (0.017)	0.067 (0.025)	0 (0.0071)	0 (0.0026)	1	75.2	75.2	0.2
G41.74+0.10 4	0.089 (0.029)	0.13 (0.043)	0 (0.0071)	0 (0.0028)	1	75.2	75.2	0.2
IRDC 1923+13 0	0.02 (0.0062)	0.02 (0.0047)	0 (0.009)	0 (0.0028)	1	2747.75	2747.75	0.0
IRDC 1923+13 1	0.016 (0.0051)	0.017 (0.0038)	0 (0.009)	0 (0.0028)	1	2747.75	2747.75	0.0
IRDC 1923+13 2	0.0081 (0.0028)	0.0083 (0.0023)	0 (0.009)	0 (0.0028)	1	2747.75	2747.75	0.0

Table 4
Inferred H₂CO line properties

IRDC 1916+11 0	0.033 (0.011)	0.036 (0.0062)	0 (0.014)	0 (0.042)	1	2747.75	2747.75	0.0
IRDC 1916+11 1	0.082 (0.025)	0.089 (0.0095)	0 (0.014)	0 (0.042)	1	2747.75	2747.75	0.0
IRDC 1916+11 2	0.017 (0.0064)	0.018 (0.0046)	0 (0.014)	0 (0.042)	1	2747.75	2747.75	0.0

^a The beam area is 2747.75''², which is used when the CMB is the only background continuum illumination

Table 5
Derived physical properties from H₂CO

Source Name	N(H ₂ CO) ^a (cm ⁻²)	N(H ₂ CO) (FFC) ^b (cm ⁻²)	n(H ₂) ^a (cm ⁻³)	n(H ₂) (FFC) ^b (cm ⁻³)	X _{H₂CO} ^a	X _{H₂CO} (FFC) ^b	Flag ^c
G32.80+0.19 0	12.79 ^{+0.11} _{-0.16}	12.94 ^{+0.16} _{-0.24}	5.10 ^{+0.25} _{-0.26}	5.21 ^{+0.27} _{-0.29}	-10.79 ^{+0.15} _{-0.20}	-10.75 ^{+0.15} _{-0.18}	2
G32.80+0.19 1	12.05 ^{+0.12} _{-0.11}	12.14 ^{+0.13} _{-0.13}	4.96 ^{+0.22} _{-0.28}	5.05 ^{+0.21} _{-0.28}	-11.39 ^{+0.20} _{-0.23}	-11.39 ^{+0.17} _{-0.20}	2
G32.80+0.19 2	11.66 ^{+0.10} _{-0.10}	11.71 ^{+0.10} _{-0.10}	4.16 ^{+0.39} _{-0.38}	4.33 ^{+0.31} _{-0.32}	-10.97 ^{+0.44} _{-0.46}	-11.10 ^{+0.37} _{-0.37}	2
G32.80+0.19 3	12.18 ^{+0.10} _{-0.09}	12.23 ^{+0.09} _{-0.09}	4.07 ^{+0.38} _{-0.39}	4.23 ^{+0.32} _{-0.32}	-10.37 ^{+0.44} _{-0.45}	-10.48 ^{+0.36} _{-0.38}	2
G32.80+0.19 4	11.82 ^{+0.10} _{-0.09}	11.87 ^{+0.10} _{-0.09}	4.30 ^{+0.31} _{-0.32}	4.44 ^{+0.26} _{-0.29}	-10.97 ^{+0.37} _{-0.37}	-11.05 ^{+0.31} _{-0.32}	2
G33.13-0.09 0	> 12.80	> 13.56	> 4.54	> 5.10	> -10.62	> -11.70	8
G33.13-0.09 1	< 11.96	< 11.90	< 4.50	< 3.91	< -8.44	< -8.45	6
G33.13-0.09 2	< 12.20	< 0.00	< 4.29	< 0.00	< -8.29	< 0.00	5
G33.13-0.09 3	< 12.20	< 0.00	< 4.32	< 0.00	< -8.29	< 0.00	5
G33.92+0.11 0	> 12.35	> 12.64	> 4.86	> 5.16	> -11.29	> -12.30	8
G33.92+0.11 1	12.34 ^{+0.07} _{-0.08}	12.65 ^{+0.11} _{-0.17}	4.97 ^{+0.22} _{-0.23}	5.26 ^{+0.22} _{-0.24}	-11.11 ^{+0.19} _{-0.22}	-11.09 ^{+0.13} _{-0.16}	2
G33.92+0.11 2	-	-	-	-	-	-	9
G34.26+0.15 0	13.01 ^{+0.10} _{-0.17}	13.13 ^{+0.15} _{-0.23}	4.91 ^{+0.28} _{-0.29}	5.01 ^{+0.31} _{-0.32}	-10.38 ^{+0.18} _{-0.23}	-10.36 ^{+0.17} _{-0.23}	2
G34.26+0.15 1	11.79 ^{+0.09} _{-0.08}	11.83 ^{+0.09} _{-0.08}	4.67 ^{+0.23} _{-0.25}	4.75 ^{+0.21} _{-0.24}	-11.36 ^{+0.26} _{-0.27}	-11.40 ^{+0.23} _{-0.25}	2
G34.26+0.15 2	11.53 ^{+0.10} _{-0.10}	11.56 ^{+0.10} _{-0.10}	4.38 ^{+0.30} _{-0.33}	4.48 ^{+0.28} _{-0.30}	-11.33 ^{+0.36} _{-0.37}	-11.40 ^{+0.32} _{-0.34}	2
G34.26+0.15 3	11.63 ^{+0.11} _{-0.10}	11.66 ^{+0.10} _{-0.10}	4.43 ^{+0.29} _{-0.32}	4.53 ^{+0.26} _{-0.30}	-11.28 ^{+0.34} _{-0.35}	-11.34 ^{+0.31} _{-0.32}	2
G34.26+0.15 4	11.40 ^{+0.17} _{-0.14}	11.45 ^{+0.17} _{-0.16}	4.87 ^{+0.31} _{-0.43}	4.94 ^{+0.30} _{-0.42}	-11.95 ^{+0.30} _{-0.35}	-11.98 ^{+0.27} _{-0.34}	2
G35.20-1.74 0	12.60 ^{+0.08} _{-0.07}	12.65 ^{+0.08} _{-0.07}	4.72 ^{+0.25} _{-0.25}	4.79 ^{+0.25} _{-0.26}	-10.61 ^{+0.23} _{-0.27}	-10.62 ^{+0.22} _{-0.26}	2
G35.20-1.74 1	11.69 ^{+0.11} _{-0.10}	11.72 ^{+0.11} _{-0.10}	4.30 ^{+0.33} _{-0.37}	4.41 ^{+0.30} _{-0.33}	-11.09 ^{+0.39} _{-0.39}	-11.16 ^{+0.34} _{-0.36}	2
G35.20-1.74 2	11.97 ^{+0.09} _{-0.09}	12.00 ^{+0.09} _{-0.09}	4.20 ^{+0.34} _{-0.35}	4.31 ^{+0.30} _{-0.30}	-10.70 ^{+0.39} _{-0.41}	-10.79 ^{+0.34} _{-0.36}	2
G35.20-1.74 3	< 11.41	< 11.44	< 4.89	< 5.02	< -9.24	< -9.30	6
G35.57-0.03 0	> 12.42	> 13.38	> 4.82	> 5.61	> -11.20	> -12.02	8
G35.57-0.03 1	> 11.72	> 12.25	> 4.51	> 5.13	> -11.80	> -12.72	8
G35.57-0.03 2	> 11.98	> 12.12	> 4.96	> 5.12	> -8.71	> -8.72	6
G35.57-0.03 3	< 12.09	< 12.23	< 4.60	< 4.78	< -8.38	< -8.37	6
G35.57-0.03 4	> 11.93	> 12.47	> 4.58	> 5.20	> -11.55	> -12.48	8
G35.58+0.07 0	> 12.58	> 14.06	> 4.50	> 5.48	> -10.79	> -11.71	8
G35.58+0.07 1	< 12.19	< 12.32	< 4.08	< 4.55	< -8.07	< -8.14	6
G35.58+0.07 2	< 11.96	< 12.10	< 4.57	< 4.95	< -8.53	< -8.63	6
G35.58+0.07 3	< 12.06	< 12.17	< 4.35	< 4.38	< -8.32	< -8.24	6
G37.87-0.40 0	12.44 ^{+0.07} _{-0.07}	12.53 ^{+0.07} _{-0.09}	4.86 ^{+0.22} _{-0.23}	4.98 ^{+0.21} _{-0.24}	-10.90 ^{+0.20} _{-0.24}	-10.92 ^{+0.18} _{-0.21}	2
G37.87-0.40 1	11.87 ^{+0.10} _{-0.09}	11.95 ^{+0.10} _{-0.09}	4.89 ^{+0.22} _{-0.26}	5.00 ^{+0.21} _{-0.24}	-11.50 ^{+0.21} _{-0.24}	-11.53 ^{+0.18} _{-0.22}	2
G37.87-0.40 2	12.10 ^{+0.18} _{-0.26}	12.09 ^{+0.14} _{-0.28}	3.16 ^{+1.15} _{-1.20}	3.79 ^{+1.78} _{-0.71}	-9.54 ^{+1.32} _{-1.41}	-10.18 ^{+0.77} _{-2.06}	4
G37.87-0.40 3	12.05 ^{+0.10} _{-0.10}	12.10 ^{+0.10} _{-0.09}	4.33 ^{+0.32} _{-0.33}	4.49 ^{+0.28} _{-0.29}	-10.76 ^{+0.37} _{-0.39}	-10.87 ^{+0.31} _{-0.34}	2
G37.87-0.40 4	12.17 ^{+0.17} _{-0.25}	12.14 ^{+0.10} _{-0.09}	3.36 ^{+1.35} _{-0.98}	4.13 ^{+0.35} _{-0.36}	-9.67 ^{+1.12} _{-1.60}	-10.46 ^{+0.41} _{-0.42}	2
G37.87-0.40 5	11.85 ^{+0.18} _{-0.21}	11.88 ^{+0.18} _{-0.25}	3.05 ^{+1.04} _{-1.17}	3.34 ^{+1.33} _{-1.03}	-9.68 ^{+1.32} _{-1.25}	-9.94 ^{+1.17} _{-1.58}	4
G37.87-0.40 6	11.67 ^{+0.19} _{-0.23}	11.70 ^{+0.19} _{-0.26}	3.08 ^{+1.07} _{-1.21}	3.33 ^{+1.32} _{-1.13}	-9.89 ^{+1.36} _{-1.30}	-10.11 ^{+1.26} _{-1.58}	4
G37.87-0.40 7	11.81 ^{+0.10} _{-0.09}	11.86 ^{+0.10} _{-0.09}	4.28 ^{+0.31} _{-0.33}	4.45 ^{+0.27} _{-0.29}	-10.95 ^{+0.37} _{-0.38}	-11.07 ^{+0.32} _{-0.32}	2
G37.87-0.40 8	11.56 ^{+0.11} _{-0.11}	11.63 ^{+0.11} _{-0.10}	4.67 ^{+0.30} _{-0.33}	4.80 ^{+0.29} _{-0.31}	-11.59 ^{+0.34} _{-0.38}	-11.65 ^{+0.30} _{-0.34}	2
G37.87-0.40 9	11.72 ^{+0.13} _{-0.29}	11.74 ^{+0.10} _{-0.09}	3.98 ^{+1.97} _{-0.52}	4.32 ^{+0.31} _{-0.32}	-10.74 ^{+0.60} _{-2.26}	-11.06 ^{+0.36} _{-0.37}	2
G43.89-0.78 0	12.49 ^{+0.10} _{-0.09}	12.76 ^{+0.08} _{-0.07}	4.18 ^{+0.34} _{-0.33}	4.68 ^{+0.28} _{-0.28}	-10.17 ^{+0.37} _{-0.40}	-10.40 ^{+0.24} _{-0.30}	2
G43.89-0.78 1	11.87 ^{+0.09} _{-0.08}	12.80 ^{+0.61} _{-1.00}	4.95 ^{+0.20} _{-0.23}	6.16 ^{+0.96} _{-1.84}	-11.56 ^{+0.19} _{-0.22}	-11.84 ^{+0.88} _{-0.42}	1
G45.07+0.13 0	12.38 ^{+0.08} _{-0.08}	12.75 ^{+0.13} _{-0.20}	4.96 ^{+0.22} _{-0.24}	5.25 ^{+0.25} _{-0.27}	-11.06 ^{+0.19} _{-0.22}	-10.97 ^{+0.15} _{-0.18}	2
G45.07+0.13 1	-	-	-	-	-	-	9
G45.12+0.13 0	12.02 ^{+0.08} _{-0.07}	12.07 ^{+0.08} _{-0.07}	4.83 ^{+0.21} _{-0.21}	4.92 ^{+0.19} _{-0.21}	-11.30 ^{+0.20} _{-0.23}	-11.32 ^{+0.19} _{-0.21}	2
G45.12+0.13 1	11.90 ^{+0.09} _{-0.08}	11.95 ^{+0.08} _{-0.08}	4.74 ^{+0.22} _{-0.23}	4.83 ^{+0.21} _{-0.23}	-11.32 ^{+0.23} _{-0.25}	-11.36 ^{+0.21} _{-0.23}	2
G45.12+0.13 2	11.90 ^{+0.10} _{-0.08}	11.93 ^{+0.09} _{-0.09}	4.41 ^{+0.26} _{-0.28}	4.52 ^{+0.24} _{-0.26}	-11.00 ^{+0.32} _{-0.32}	-11.06 ^{+0.29} _{-0.30}	2
G45.12+0.13 3	11.48 ^{+0.08} _{-0.09}	11.55 ^{+0.08} _{-0.12}	5.15 ^{+0.19} _{-0.21}	5.23 ^{+0.19} _{-0.22}	-12.15 ^{+0.16} _{-0.18}	-12.16 ^{+0.14} _{-0.17}	2
G45.45+0.06 0	12.62 ^{+0.08} _{-0.08}	12.64 ^{+0.07} _{-0.08}	4.33 ^{+0.29} _{-0.31}	4.37 ^{+0.28} _{-0.28}	-10.19 ^{+0.33} _{-0.35}	-10.21 ^{+0.30} _{-0.33}	2
G45.45+0.06 1	11.89 ^{+0.08} _{-0.08}	11.92 ^{+0.07} _{-0.07}	5.00 ^{+0.26} _{-0.28}	5.04 ^{+0.26} _{-0.27}	-11.59 ^{+0.25} _{-0.29}	-11.60 ^{+0.23} _{-0.28}	2

Table 5
Derived physical properties from H₂CO

G45.45+0.06 2	< 11.55	< 11.66	< 4.77	< 5.39	< -9.04	< -9.43	6
G45.47+0.05 0	12.71 ^{+0.09} _{-0.07}	13.48 ^{+0.32} _{-0.50}	4.46 ^{+0.28} _{-0.28}	5.21 ^{+0.40} _{-0.34}	-10.23 ^{+0.28} _{-0.31}	-10.21 ^{+0.21} _{-0.19}	2
G45.47+0.05 1	< 11.91	< 11.92	< 5.34	< 5.23	< -8.65	< -8.57	5
G48.61+0.02 0	12.06 ^{+0.09} _{-0.09}	12.53 ^{+0.13} _{-0.17}	4.68 ^{+0.23} _{-0.25}	5.29 ^{+0.22} _{-0.24}	-11.10 ^{+0.25} _{-0.26}	-11.25 ^{+0.13} _{-0.16}	2
G48.61+0.02 1	< 11.88	< 11.91	< 5.09	< 4.47	< -8.61	< -8.58	5
G48.61+0.02 2	11.54 ^{+0.14} _{-0.13}	11.94 ^{+0.18} _{-0.23}	4.60 ^{+0.28} _{-0.39}	5.22 ^{+0.23} _{-0.36}	-11.54 ^{+0.33} _{-0.33}	-11.76 ^{+0.14} _{-0.19}	2
G50.32+0.68 0	> 11.71	> 12.41	> 4.61	> 5.31	> -11.77	> -12.63	8
G60.88-0.13 0	12.24 ^{+0.18} _{-0.25}	12.35 ^{+0.09} _{-0.09}	3.20 ^{+1.19} _{-1.16}	4.51 ^{+0.27} _{-0.28}	-9.44 ^{+1.29} _{-1.43}	-10.64 ^{+0.28} _{-0.31}	2
G61.48+0.09 0	> 12.51	> 12.62	> 5.07	> 5.19	> -11.27	> -12.33	8
G69.54-0.98 0	-	-	-	-	-	-	11
G70.29+1.60 0	12.21 ^{+0.09} _{-0.08}	12.25 ^{+0.08} _{-0.08}	4.67 ^{+0.23} _{-0.23}	4.74 ^{+0.23} _{-0.24}	-10.94 ^{+0.24} _{-0.26}	-10.97 ^{+0.23} _{-0.26}	2
G70.29+1.60 1	< 11.53	< 11.55	< 4.50	< 4.67	< -8.92	< -8.98	6
G70.33+1.59 0	13.16 ^{+0.09} _{-0.14}	13.41 ^{+0.19} _{-0.35}	4.64 ^{+0.34} _{-0.32}	4.83 ^{+0.39} _{-0.37}	-9.96 ^{+0.22} _{-0.31}	-9.90 ^{+0.21} _{-0.26}	2
IRAS 20051+3435 0	12.20 ^{+0.11} _{-0.10}	12.23 ^{+0.04} _{-0.05}	4.12 ^{+0.39} _{-0.41}	4.11 ^{+0.21} _{-0.23}	-10.40 ^{+0.45} _{-0.46}	-10.35 ^{+0.22} _{-0.22}	3
G41.74+0.10 0	12.25 ^{+0.17} _{-0.23}	12.48 ^{+0.10} _{-0.09}	2.99 ^{+0.99} _{-1.18}	4.50 ^{+0.28} _{-0.31}	-9.23 ^{+1.31} _{-1.22}	-10.50 ^{+0.29} _{-0.32}	2
G41.74+0.10 1	< 12.12	< 0.00	< 4.72	< 0.00	< -8.37	< 0.00	5
G41.74+0.10 2	< 12.18	< 0.00	< 3.21	< 0.00	< -8.91	< 0.00	5
G41.74+0.10 3	< 12.17	< 0.00	< 4.70	< 0.00	< -8.32	< 0.00	5
G41.74+0.10 4	< 12.27	< 0.00	< 4.11	< 0.00	< -8.22	< 0.00	5
IRDC 1923+13 0	< 11.86	< 11.84	< 5.19	< 4.47	< -8.63	< -8.65	5
IRDC 1923+13 1	< 11.86	< 11.77	< 5.30	< 4.58	< -8.70	< -8.72	5
IRDC 1923+13 2	< 13.29	< 11.53	< 8.00	< 5.00	< -8.95	< -8.96	5
IRDC 1916+11 0	< 12.05	< 12.57	< 5.16	< 5.62	< -8.44	< -8.46	5
IRDC 1916+11 1	< 12.36	< 12.40	< 4.61	< 5.03	< -8.13	< -8.16	5
IRDC 1916+11 2	< 12.09	< 13.77	< 5.55	< 8.00	< -8.68	< -8.68	5

^a The values used in this paper are shown in boldface. Uncorrected values are listed in this column. The filling-factor corrected values are shown for comparison in the next column even though they were not used for analysis.

^b The values used in this paper are shown in boldface. Filling-factor corrected values are listed in this column. The uncorrected values are shown for comparison in the previous column even though they not used for analysis.

^c Flags:

1. No filling factor correction (no FFC) is the most reliable.
2. Filling factor correction (FFC) is the most reliable
3. There is an ambiguity between low density / high abundance and low abundance / high density (no FFC)
4. There is an ambiguity between low density / high abundance and low abundance / high density (FFC)
5. Upper Limit (No FFC)
6. Upper Limit (FFC)
7. Lower Limit (No FFC)
8. Lower Limit (FFC)
9. Unreliable estimate because of continuum / filling factor uncertainty.
10. No limit (S/N)
11. Optically Thick

2.2. Green Bank Telescope

We observed the H₂CO 2₁₁ – 2₁₂ line at 2 cm (14.488789 GHz) with the Green Bank Telescope (GBT)⁴ dual-beam Ku-band receiver as part of project GBT09C-049. The GBT dual-beam Ku-band receiver was used for 4 hours on January 18th, 2010 in beam-switched nodding mode. System temperatures ranged from 27 to 38 K in

the H₂CO band centered on the 2₁₁ – 2₁₂ line. A bandwidth of 12.5 MHz (258.8 km s⁻¹) and channel width of 3.052 kHz (0.063 km s⁻¹) were used with 9-level sampling, with receiver temperature ≈ 21K. Three additional tunings were acquired simultaneously, centered between the H and He 75α, 76α, and 77α radio recombination lines (RRLs) with the same channel widths and bandwidths as above at 14.1315, 14.6930, and 15.2846 GHz. Each source was observed for 150 seconds in each receiver for a total on-source integration time of 300 seconds. Each observation in the pair was independently inspected to search for emission/absorption in the off position, which was 5.5' away in azimuth. When absorption was detected in one of the off positions, that on/off pair was discarded if one of the detected lines was affected, but otherwise was noted and ignored. Pointing and focus observations on the calibrator source 1822-0938 were taken at the start of and two hours into the observations.

The gain was assumed to be 1.91 K/Jy based on previous calibration observations on point sources in Ku-band; our flux density measurements will therefore be overestimates for extended sources. The aperture efficiency was $\eta_A = 0.671$, and the main beam efficiency $\eta_{MB} = 1.32\eta_A = 0.886$, so our main-beam corrected measurements could overestimate extended source flux densities by at most 13% (ignoring atmospheric absorption). The data were calibrated using the normal GETNOD procedure in GBTIDL⁵, which assumes an atmospheric opacity at zenith $\tau = 0.014$ at 14.488 GHz.

We assume primary beam $\theta_{FWHM} = 51.1''$ per the GBT observers manual. We assume a conservative 10% error in the beam area $\Omega = 7.8 \times 10^{-8}$ sr, which governs

⁴ The National Radio Astronomy Observatory operates the GBT and VLA and is a facility of the National Science Foundation operated under cooperative agreement by Associated Universities, Inc.

⁵ GBTIDL (<http://gbitdl.nrao.edu/>) is the data reduction package produced by NRAO and written in the IDL language for the reduction of GBT data. The National Radio Astronomy Observatory is a facility of the National Science Foundation operated under cooperative agreement by Associated Universities, Inc.

the flux density received from the CMB over the observed area. Beam size error should be dominated by small errors in focus. By utilizing the 305 m Arecibo telescope at 6 cm and the 100 m GBT at 2 cm, we acquired beam-matched (FWHM $\sim 50''$) observations of the H₂CO 1₁₀ – 1₁₁ and 2₁₁ – 2₁₂ lines.

2.2.1. GBT Data Reduction

In the 24 lines of sight, 75 independent components were identified from the 1₁₀ – 1₁₁ spectra. These were fit with gaussians using GBTIDL's FITGAUSS routine. Out of these 75 components, 51 had corresponding 2₁₁ – 2₁₂ detections. The fitted gaussian spectral lines are listed by line of sight in Table 1. The gaussian fits may not be representative of the true spectral line profile; complex spectral line profiles are discussed in Section 6.2.

The 2 cm continua were measured by fitting a first-order baseline in each reduced nodded pair excluding the line and the bandpass edges. Figure 1 shows the flat baselines achieved in the observations, though the RRL spectrum shows an example of the artifacts seen at the edges of the bandpass. The continuum error listed in the table is the RMS of only the data included in the baseline fit after the baseline was subtracted from the spectrum; the systematic error from flux calibration uncertainty is 20% and dominant.

2.3. Arecibo

The Arecibo 4.829660 GHz H₂CO 1₁₀ – 1₁₁ observations used in this project were previously presented in Araya et al. (2002) and Araya et al. (2004) and were kindly provided in reduced form by E. Araya. All observations were performed using standard on/off position switching and 5 minute integration times in both the on and off positions, resulting in off positions 1.25 degrees away from the pointing center. We assume a 30% error in the continuum (based on measured gains in the range 2.0-2.5 as reported in Araya et al. 2002) and an effective diameter of 227m ($\theta_{FWHM} = 56''$, $\Omega = 9.0 \times 10^{-8}$ sr) with 10% uncertainty⁶.

The Arecibo spectral lines were re-fit for this paper by converting the Arecibo data from CLASS⁷ to GBTIDL's SDFITS format⁸ and using GBTIDL's FITGAUSS routine. The 6 cm continua were taken directly from Araya et al. (2002) Table 3.

2.4. Other Archival Data

2.4.1. Very Large Array

We acquired VLA archival images from the Multi-Array Galactic Plane Imaging Survey (MAGPIS) 6 cm Epoch 3 data set (Helfand et al. 2006) and the NRAO VLA Archive Survey (NVAS)⁹. MAGPIS has a resolution of $\sim 4''$ and sensitivity $\sigma \sim 2.5$ mJy/bm. The NVAS has variable resolution and sensitivity since it is based on VLA archival data. The VLA data was used to estimate source sizes and interferometer-to-single-dish flux ratios.

⁶ http://www.naic.edu/~simphil/sysperf/misc/hpbw_vs_lambda_2004.html

⁷ CLASS is part of the GILDAS software developed by IRAM.

⁸ Code for the CLASS-GBTIDL conversion is available from http://code.google.com/p/casarradio/wiki/class_to_gbt

⁹ The NVAS is run by Laurant Sjouwerman at the NRAO. It has not yet been published.

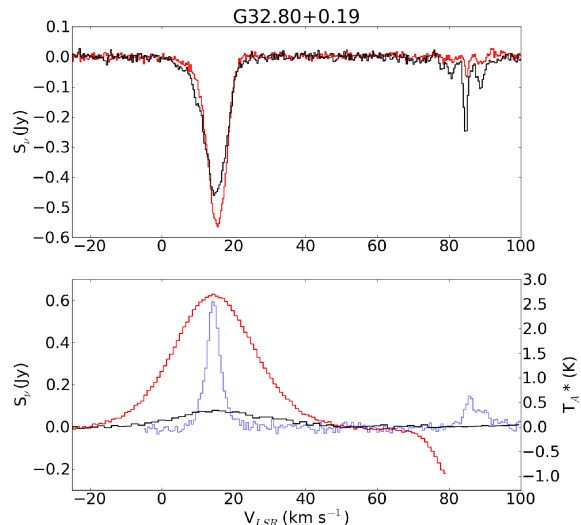


Figure 1. *Top:* The GBT 2₁₁ – 2₁₂ (red) and Arecibo 1₁₀ – 1₁₁ (black) spectra of G32.80+0.19. *Bottom:* The GBT H75 α (red) and Arecibo H110 α (black) spectra with the GRS ¹³CO spectrum (light blue) overlaid. The left axis is for the RRLs and the right axis is for the ¹³CO. The C and He RRLs are not displayed.

2.4.2. Bolocam 1.1 mm

We extract 1.1 mm dust continuum fluxes from the Bolocam Galactic Plane Survey (BGPS) v1.0 release summing over a 25'' radius aperture after subtracting the median in a 50-200'' annulus to remove background contributions. The aperture size is selected to match the 1.1 mm data to the 2 and 6 cm data. We assume a uniform 50% systematic error in BGPS fluxes from combined uncertainties in the calibration and background subtraction. Aguirre et al. (2011) contains a complete discussion of the uncertainties in the BGPS. We apply the Aguirre et al. (2011) recommended flux correction of 1.5 and aperture correction for a 25'' aperture of 1.21. Additionally, data from the Bolocam catalog (Rosolowsky et al. 2010) was used with the flux correction and an aperture correction of 1.46 for 20'' apertures.

2.4.3. Boston University / Five College Radio Observatory Galactic Ring Survey

The BU FCRAO GRS (Jackson et al. 2006) is a survey of the Galactic plane in the ¹³CO 1-0 line with $\sim 46''$ resolution. We extracted spectra in 25'' radius apertures from the publicly available data for comparison with the H₂CO spectra.

2.4.4. GLIMPSE

The Galactic Legacy Infrared Mid-Plane Survey Extraordinaire (Benjamin et al. 2003, GLIMPSE) maps were used to examine the morphology of the objects in our survey in order to determine whether an IRDC was present.

3. MODELS AND ERROR ESTIMATION

A grid of large velocity gradient (LVG) models was run using both the RADEX (van der Tak et al. 2007) code and a proprietary code by Henkel et al. (1980) with a gradient of 1 km s⁻¹pc⁻¹. The models from the two codes were consistent to within $\sim 10\%$ in predicted optical depth and T_{ex} . Both utilized collision rates from

Green (1991) extracted from the LAMDA database¹⁰ and multiplied by the recommended factor of 1.6 to account for collisions with H₂ being more efficient than He. The expected accuracy is $\sim 30\%$. Zeiger & Darling (2010) demonstrated that the errors in collision rates lead to systematic errors $\lesssim 50\%$ (0.3 dex) in the measured quantities ($N(\text{H}_2\text{CO})$, $n(\text{H}_2)$). When measuring density and column, we used the RADEX models because of their extensively tested code and documentation. All of the models used a kinetic temperature of 40 K and covered a range of 500 densities \times 500 columns logarithmically sampled over $10^1 < n(\text{H}_2) < 10^7 \text{ cm}^{-3}$ and $10^{11} < N(\text{o-H}_2\text{CO}) < 10^{16} \text{ cm}^{-2}$. The assumption $T_K = 40 \text{ K}$ is reasonable in UCH II regions, which should be warmer than IRDCs and other cold molecular clouds. Dust temperatures measured towards UCH II regions are around 40 K (Rivera-Ingraham et al. 2010). In the foreground clouds, this assumption is less well supported, but as long as the temperatures are higher than $\sim 20 \text{ K}$, the models change little with temperature (Figure 2).

Because of a collisional selection effect, above its critical density ($n_{cr}(\text{H}_2\text{CO } 1_{10} - 1_{11}) \approx 8 \text{ cm}^{-3}$, $n_{cr}(\text{H}_2\text{CO } 2_{11} - 2_{12}) \approx 76 \text{ cm}^{-3}$, Mangum et al. 2008) H₂CO preferentially overpopulates lower states of the K-doublet ($\Delta J = 0$, $\Delta K_a = 0$, $\Delta K_c = \pm 1$, Henkel et al. 1980). These spectral lines are cooled to excitation temperatures lower than the CMB and can therefore be seen in absorption against it. The $1_{10} - 1_{11}/2_{11} - 2_{12}$ absorption line ratio is sensitive to the density of H₂ at densities $\gtrsim 10^{3.5} \text{ cm}^{-3}$, allowing measurements of the density to within ~ 0.3 dex with little sensitivity to gas kinetic temperature (Mangum et al. 2008). When density is ‘measured’ with critical density based tracers such as CO, CS, HCN, or HCO⁺, the estimate can be off by as much as 2 orders of magnitude because of radiative trapping effects. Similarly, measurements of density assuming spherical symmetry can be very far from the local values.

The collision rates of H₂CO with H₂ have been re-derived with a claimed accuracy of 10% by Troscompt et al. (2009b). Troscompt et al. (2009a) showed that collisions with para-H₂ are more efficient at cooling H₂CO into absorption against the CMB than He or ortho-H₂ and that H₂CO absorption is therefore sensitive to the Ortho/Para ratio of H₂. These improved rates are not used in this paper since they are only computed over a more limited range of temperatures, but may be used in future works.

3.1. Turbulence

Molecular gas is often observed to have spectral line widths consistent with supersonic turbulence (Kainulainen et al. 2009) and therefore a lognormal density distribution (Kritsuk et al. 2007). Our LVG models assume constant density per velocity bin, so the resulting models should be smoothed by the probability distribution function (PDF) of the density. For clouds with a narrow density distribution (logarithmic standard deviation of the density $\sigma_s \equiv \sigma_{\ln(\rho)}/\ln(\bar{\rho}) \lesssim 0.5$)¹¹, the effect of smoothing is smaller than other systematic errors, but

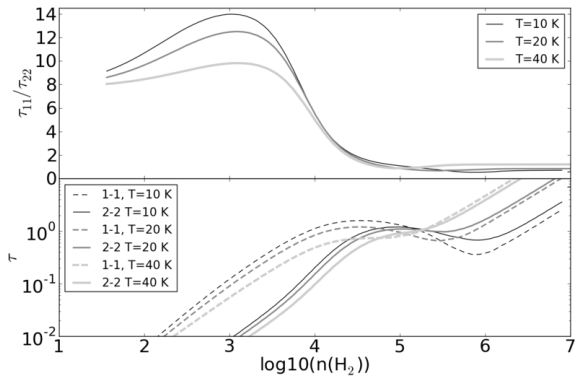


Figure 2. The predicted optical depth ratio (*top*) and optical depth (*bottom*) vs. volume density assuming a fixed abundance $X_{\text{o-H}_2\text{CO}} = 10^{-9}$ per $\text{km s}^{-1}\text{pc}^{-1}$ shows that the dependence of the derived density on temperature is weak. At lower abundances, these curves shift to the right, providing sensitivity to moderately higher densities. Our 5- σ detection limit is generally around $\tau \sim 0.01$.

for more turbulent clouds the density PDF width can exceed an order of magnitude (e.g., Federrath et al. 2010) and will substantially change the derived density. Because the Mach numbers of the turbulence in the observed clouds are unconstrained, we cannot correct for this added uncertainty. The change in measured density is $|\Delta \log(\rho)| < 0.25$ for $\sigma_s \leq 0.5$, with a slight bias towards higher densities at lower optical depth ratio $\tau_{1_{10}-1_{11}}/\tau_{2_{11}-2_{12}}$ (Figure 3). However, for $\sigma_s = 1.5$, the bias exceeds an order of magnitude at some densities.

Additionally, we consider the effects of ‘gravoturbulence’, in which a high-density tail inconsistent with a lognormal distribution is observed. Kainulainen et al. (2009) report column density distributions derived from 2MASS extinction measurements that can be used as a proxy for the density distribution for a wide variety of clouds. Non-star-forming clouds retain a lognormal distribution and are consistent with the analysis presented above. However, evolved star-forming regions develop a high-column density tail. For evolved (actively star-forming) regions like Ophiucus, Orion, and Perseus, the high-column density tail is substantial, and H₂CO density measurements will be highly biased towards the highest density gas. More quiescent regions like the Pipe and Coalsack nebulae are consistent with a lognormal column distribution to a degree that the high-column density tail would not affect H₂CO density measurements significantly.

To demonstrate the effects of turbulent distributions, we calculate the optical depth ratio as a function of the mean density for three turbulent widths in Figure 3. We compare the density that would be inferred from the spectral line ratio assuming no turbulence (just LVG) to the ‘correct’ density including turbulent effects in Figure 4. We have also compared the LVG and turbulent densities to ‘gravoturbulent’ density distributions, in which a power law tail of high-density gas begins at about 10^{-2} times the peak density (e.g., Klessen 2000; Cho & Kim 2011), but because the density distributions in these simulations are relatively narrow, the effects of the high-density tail on the measured density are negligible except

relative to a mean density, the scaling between mass and number density is unimportant.

¹⁰ [http://www.strw.leidenuniv.nl/\\$\sim\\$smoldata/](http://www.strw.leidenuniv.nl/\simsmoldata/)

¹¹ We use ρ to indicate number density in this section in order to be consistent with the cited literature. Because the widths are

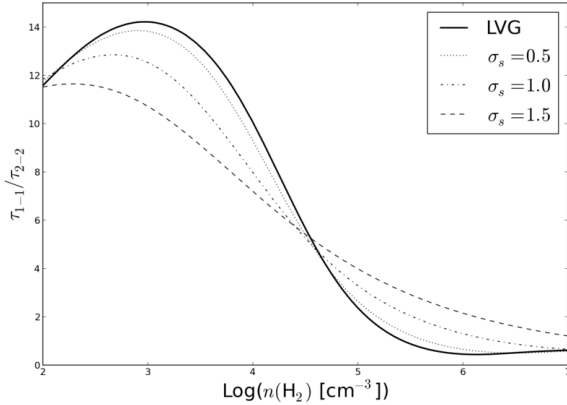


Figure 3. The optical depth ratio as a function of density for turbulent density distributions with widths specified in the legend. The optical depth ratio varies more slowly with density than in the pure LVG model (the solid line is the same as the black 10 K line in Figure 2a).

for the most turbulent cases.

Figure 3 is meant to demonstrate the effects of turbulence, but it is *not* used to derive densities, since the true density distribution in observed clouds is unknown. However, future measurements of the density distribution can be used to apply the ‘correction’ shown in Figure 4.

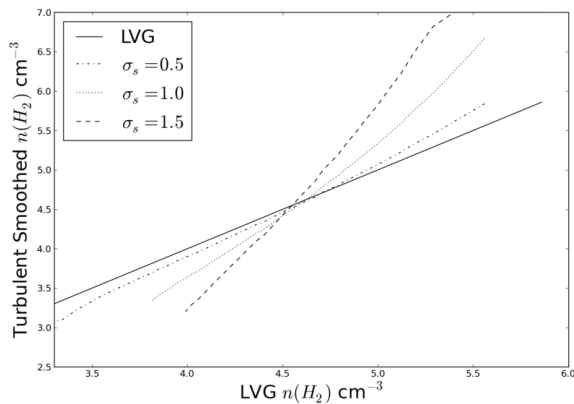


Figure 4. The mean density from a lognormal density distribution plotted against the density derived assuming a single density per region (i.e., the directly LVG-derived density). At low densities, the wider turbulent distributions are heavily biased towards “observing” higher densities than the true mean density. The distributions cut off at the low end where the optical depth ratio becomes a double-valued function of density; at these low densities, no detections are expected at our survey’s sensitivity. The cutoff at the high end is where the optical depth ratio becomes constant.

4. ANALYSIS

4.1. Measuring Line Optical Depth

In order to measure physical properties of an absorbing source, measurements must be obtained of the optical depths of both the $1_{10} - 1_{11}$ and $2_{11} - 2_{12}$ lines. These measurements are presented in Tables 1 and 1. Once an optical depth with errors is determined, the spectral line depths can be matched to large velocity gradient (LVG) models to determine column and spatial density. The spectral line optical depth depends both on the nadir flux density of the absorption line and the strength of the illuminating background continuum source. If the

background is the CMB, the ‘filling factor’ of the molecular cloud is simply its size relative to the beam size. If there is a continuum source in addition to the CMB, the size of the continuum source and the intervening molecular cloud both affect the absorption depth. Throughout this paper, we use the term ‘filling factor’ to refer to the fraction of the beam area filled by the absorbing molecular cloud and ‘covering factor’ to refer to the fraction of the background continuum source that is covered by the intervening molecular material.

The VLA archival images were used to estimate the size of the illuminating background source. When images at both wavelengths were available, we separately determined the 2 cm and 6 cm source sizes. The source size determination is imprecise because we select a single source size for non-uniform surface brightness profiles, and in many cases the VLA observation did not recover the full flux density seen in single-dish measurements. Araya et al. (2002) estimated the interferometer-to-single-dish flux ratio at 6 cm in this sample and found that the interferometer observations recovered anywhere from 3% to 100% of the single-dish flux. We repeat these measurements at 2 cm and find that the typical recovery fraction is higher, $\sim 40\%$ to 100%, although sources for which only VLA upper limits could be measured have recovery fractions $< 1\%$.

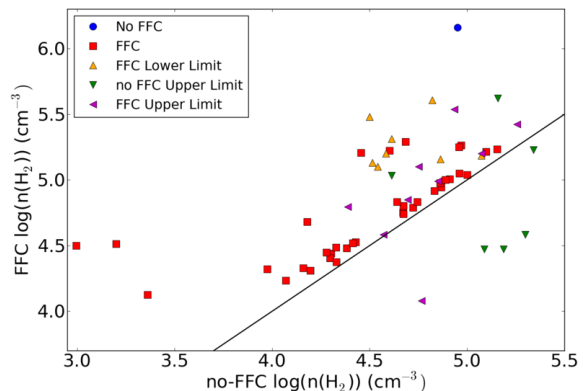


Figure 5. The filling factor corrected (FFC) density vs. the derived density with no filling factor correction. While there are some cases where the correction results in an order of magnitude or more increase in the density, most points show a small correction. The black line is the one-one line. Red squares show where the filling factor corrected point was used, while blue circles show where the uncorrected point was used. Magenta left-pointing triangles are limits where the filling factor correction was used, green downward triangles are limits where the uncorrected points were used, and orange upward triangles are lower limits where the filling-factor correction was used.

The optical depth measurements were “filling factor corrected” by assuming the CMB only contributed flux density over the same area as the H II region (i.e., the foreground cloud covers the exact same patch of sky as the UCH II region). When the H II region is small (e.g., 10% of the beam area or less), the contribution of the CMB to the continuum is negligible, but in cases of more diffuse H II regions, the CMB contribution is significant, particularly at 2 cm. The inferred optical depths and source areas are presented in Table 4. Both “filling factor corrected” and uncorrected densities are presented in Table 5. The effect of the filling factor correction (FFC)

on density measurements is shown in Figure 5. In a few cases, no volume density-column density parameter space in the models (Section 3) was consistent with the spectral line ratio after filling factor correction: in these cases, the filling factor correction was not used. Similarly, no filling factor correction was applied to sources without detected continuum. These exceptions are noted in Table 5 in the “Flag” column.

The above definitions are summarized briefly in the following equations:

$$\begin{aligned} S_{\nu,obs} &= S_{\nu,cont}(1 - CF e^{-\tau_{\nu}}) - S_{\nu,CMB}(FF e^{-\tau_{\nu}}) \\ FF &= \Omega_{cloud}/\Omega_{beam} \\ CF &= \Omega_{cloud}/\Omega_{continuum} \end{aligned}$$

in which CF is the “covering factor”, FF is the “filling factor”, and there is no positive contribution from the CMB because it is assumed to be removed by position-switching.

The systematic uncertainties in the continuum and the filling factor result in similar errors in the optical depth measurement, and together dominate the total error budget for our measurements. A 30% error in the $1_{10} - 1_{11}$ and 20% error in the $2_{11} - 2_{12}$ continuum levels were assumed because of flux calibration uncertainty characteristic of the instruments. An additional 10% error in the beam area, which sets the maximum coupling to the CMB (assuming a beam-filling source), was included to account for focus error. A 20% statistical error in the cloud filling factor was assumed for the majority of the survey, but it was decreased to 10% when the ratio of continuum to CMB flux was > 0.5 and the source size was small, indicating that the VLA-measured source is indeed the dominant continuum component in the beam. The statistical error does not account for systematic errors in the geometric assumptions. Note that changes to the filling factor should have a minimal effect on the derived density unless the source sizes at 2 cm and 6 cm differ substantially, while changes in the filling factor will always have a large effect on the derived column density (Figure 6).

Measurements of volume and column density were taken by averaging over the regions of LVG model parameter space consistent with both spectral line optical depth measurements to within 1σ . The “ 1σ ” (68% confidence; errors are non-gaussian) error bars on the derived parameters (N, n, X) were taken to be the extrema of these regions. An example of this fitting process is shown in Figure 7. A second example demonstrating a lower-limit on the density (instead of a direct measurement) is shown in Figure 8. This method is not as robust as χ^2 fitting, but because there are no free fit parameters, a statistically meaningful χ^2_{ν} cannot be computed.

In some cases, the ratio of the spectral line optical depths was consistent with low density ($n \lesssim 100 \text{ cm}^{-3}$) and high abundances ($X(\text{o-H}_2\text{CO}) > 10^{-8}$ per $\text{km s}^{-1}\text{pc}^{-1}$), but these were ruled out based on the prior assumption that extremely high H_2CO abundances should not be observed at very low densities, since it is formed at higher densities and destroyed by hard UV at low columns (see discussion in Troscompt et al. 2009a).

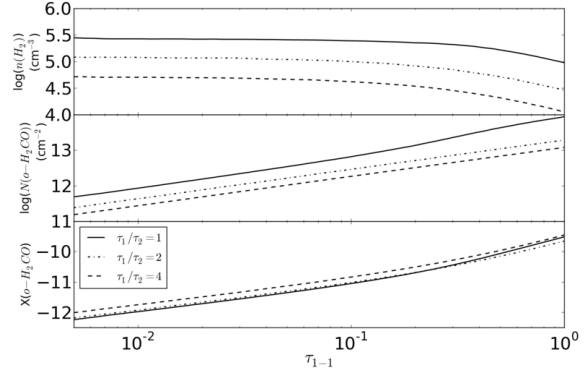


Figure 6. The dependence of derived parameters on the filling factor, assuming an optical depth ratio $\tau_{1_{10}-1_{11}}/\tau_{2_{11}-2_{12}} = 1$ (solid), 2 (dash-dot), or 4 (dashed). The X-axis is the “real” optical depth, $\tau_{1-1}(\text{real}) = \tau_{1-1}(\text{observed})/FF$. Assuming the same filling factor correction is applied to both the $1_{10} - 1_{11}$ and $2_{11} - 2_{12}$ lines, filling factor correction will only move the measurements along the X-axis of these plots. A decrease in the filling factor requires an increase in the true optical depth to maintain a constant apparent $\tau(\text{observed})$, which in turn drives up the derived abundance and column density while leaving the volume density unchanged (except at high optical depths, $\tau \gtrsim 0.2$).

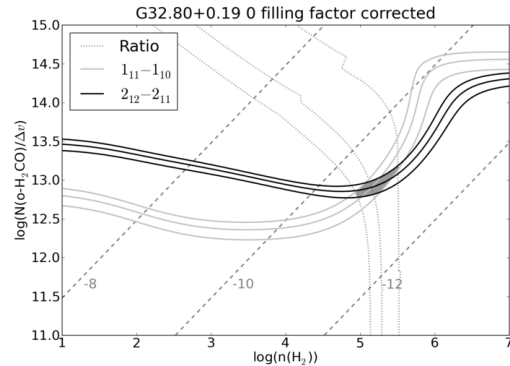


Figure 7. An example of the column density - density parameter space available given measured $1_{10} - 1_{11}$ and $2_{11} - 2_{12}$ optical depths. The dashed lines show abundances $\log_{10}(X(\text{o-H}_2\text{CO}))$ per $\text{km s}^{-1}\text{pc}^{-1}$. The contours show the regions allowed by the measurements of optical depth ($1_{10} - 1_{11}$: black, $2_{11} - 2_{12}$: grey, ratio: dotted); the middle curve is the measured value, while the pair of curves around it are $\pm 1\sigma$ including systematic error. The shaded region shows the allowed parameter space from which the physical parameters are derived.

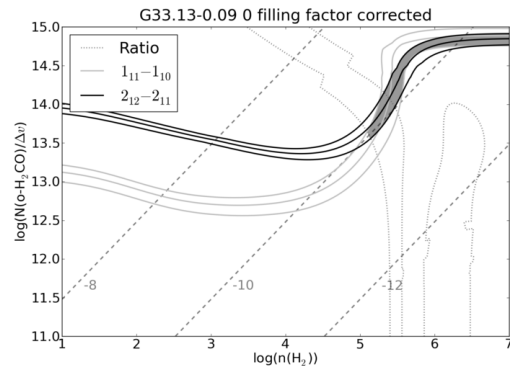


Figure 8. Same description as Figure 7 but for the strongest component in G33.13-0.09. It was only possible to measure lower limits on the volume and column density for this line; it is therefore assigned flag 8 in Table 5.

4.2. Systematic Errors: Absorption Geometry

There are potential systematic errors associated with geometric assumptions, i.e. the filling factor. There are four geometric configurations possible; these are outlined in Table 6. The “small source” geometry (3 and 4) is technically impossible given that the CMB is always present in these observations, but it is equivalent to the scenario in which the small illuminating compact source (UCH II) is much brighter than the CMB in the beam. The second column shows the effects of applying the ‘true’ filling factor correction for errors 2 and 4. For error type 3, the optical depth will only be overestimated if the absorber is “corrected” to be smaller than the background source (i.e., if a correction is applied when none should have been).

Figure 6 shows the effects of incorrect geometric assumptions. Type 1 and 3 errors - i.e. filling factor over-corrections - will result in measurements of column and abundance that are *greater* than the real values, while type 2 and 4 errors will result in column and abundance measurements that are *lower* than the real values.

Additionally, it is possible that an observation will include a beam-filling, low-density source that will contribute negligibly in 2₁₁ – 2₁₂ line absorption but substantially in 1₁₀ – 1₁₁ absorption over most of the beam area. This type of error will result in an underestimate of the volume density.

Since these errors are failures of assumptions, they cannot be quantified, but Figure 5 shows the effects of correcting for these errors to the extent possible with the available data.

Table 6
H₂CO Geometric Systematic Errors

Real Geometry	Assumed filling factor = 1	Assumed filling factor < 1
1. Beam-filling source, beam-filling absorber	^a $\tau_M = $ ^b τ_R	$\tau_M > \tau_R$
2. Beam-filling source, small absorber	$\tau_M < \tau_R$	$\tau_M = \tau_R$
3. Small source, beam-filling absorber	$\tau_M = \tau_R$	$\tau_M \geq \tau_R$
4. Small source, smaller absorber	$\tau_M < \tau_R$	$\tau_M = \tau_R$

^a τ_M = measured optical depth

^b τ_R = real optical depth

4.3. RRLs

Radio recombination lines are used to measure the velocity of the UCH II regions. The recombination lines 75-77 α were independently fitted with gaussians because the signal-to-noise in each spectrum with a detection was high. Out of our 24 spectra, there were 21 H detections, 13 He detections, and 12 C detections; Table 7 shows the fitted parameters using the 76 α lines (75 α and 77 α were also measured but are not reported for brevity). For some of the analysis in later sections, we addition-

ally use the deeper and more careful RRL study by Roshie et al. (2005), who observed 17 of our sample in the 89-92 α lines. We attempted to measure carbon RRLs in the Araya et al. (2002) spectra, who only measured hydrogen RRLs. We detected one carbon line in G61.48 and tentatively ($\sim 2\sigma$) detected another three in G32.80, G34.26, and G45.45; we report the low-significance detections in these sources because of corresponding detections of C75-77 α .

We compare the central velocities of the H and C α lines to the velocities of the H₂CO absorption lines on a case-by-case basis in Figures 23-40. The spectral line profiles are used to fit the observations into the models discussed in detail in Sections 6.2 and 6.3.

Table 7
Measured RRL 76 properties

Source Name	H			He			C		
	Peak H76 α^a (Jy)	Center H76 α (km s ⁻¹)	FWHM H76 α (km s ⁻¹)	Peak He76 α (Jy)	Center He76 α (km s ⁻¹)	FWHM He76 α (km s ⁻¹)	Peak C76 α (Jy)	Center C76 α (km s ⁻¹)	FWHM C76 α (km s ⁻¹)
G32.80+0.19	0.622 (0.001)	15.69 (0.03)	12.09 (0.03)	0.066 (0.002)	16.49 (0.36)	9.25 (0.38)	0.015 (0.002)	15.40 (1.45)	8.27 (1.64)
G33.13-0.09	0.067 (0.001)	73.49 (0.17)	14.10 (0.17)	-	-	-	-	-	-
G33.92+0.11	0.157 (0.001)	101.86 (0.07)	12.16 (0.07)	0.013 (0.001)	99.07 (0.87)	13.60 (0.87)	-	-	-
G34.26+0.15	0.367 (0.004) 0.251 (0.003)	54.68 (0.06) 37.46 (0.29)	10.43 (0.09) 22.76 (0.12)	0.034 (0.002)	51.98 (0.46)	6.54 (0.49)	0.026 (0.002)	59.54 (0.55)	5.66 (0.56)
G35.20-1.74	1.016 (0.002)	47.94 (0.02)	10.70 (0.02)	0.105 (0.002)	48.26 (0.21)	8.27 (0.21)	0.045 (0.003)	44.18 (0.33)	4.05 (0.33)
G35.57-0.03	0.036 (0.001)	52.38 (0.41)	13.71 (0.41)	-	-	-	-	-	-
G35.58+0.07	0.044 (0.001)	46.68 (0.20)	10.55 (0.20)	0.007 (0.001)	43.15 (0.94)	6.30 (0.94)	-	-	-
G37.87-0.40	0.446	59.99	15.47	0.042	60.16	11.88	0.018	59.27	7.93

Table 7
Measured RRL 76 properties

	(0.001)	(0.08)	(0.07)	(0.001)	(0.55)	(0.55)	(0.001)	(0.98)	(0.89)
	0.049	26.21	10.49	-	-	-	-	-	-
	(0.002)	(0.52)	(0.42)						
G41.74+0.10	0.038	11.46	13.89	-	-	-	-	-	-
	(0.001)	(0.29)	(0.29)						
G43.89-0.78	0.103	54.98	10.83	0.010	54.18	7.72	0.007	54.08	0.82
	(0.001)	(0.08)	(0.08)	(0.001)	(0.68)	(0.68)	(0.002)	(0.34)	(0.30)
G45.07+0.13	0.041	58.22	10.05	-	-	-	-	-	-
	(0.004)	(0.41)	(0.64)						
	0.043	41.57	20.01	-	-	-	-	-	-
	(0.003)	(1.53)	(0.59)						
G45.12+0.13	0.461	58.70	17.42	0.039	59.85	10.70	0.023	59.58	12.37
	(0.002)	(0.08)	(0.08)	(0.005)	(2.50)	(1.62)	(0.003)	(4.92)	(3.76)
G45.45+0.06	0.493	55.38	11.80	0.050	56.41	8.02	0.014	63.40	10.42
	(0.001)	(0.03)	(0.03)	(0.004)	(0.93)	(0.56)	(0.002)	(4.57)	(3.05)
G45.47+0.05	0.040	64.01	14.51	-	-	-	-	-	-
	(0.001)	(0.41)	(0.41)						
G48.61+0.02	0.076	16.77	10.53	0.007	16.33	7.73	0.006	19.08	4.71
	(0.001)	(0.14)	(0.14)	(0.001)	(1.30)	(1.39)	(0.001)	(1.26)	(1.29)
G50.32+0.68	0.034	26.94	10.27	-	-	-	-	-	-
	(0.001)	(0.27)	(0.27)						
G60.88-0.13	0.067	18.30	9.08	-	-	-	0.023	21.77	2.54
	(0.001)	(0.12)	(0.12)				(0.002)	(0.19)	(0.19)
G69.54-0.98	0.017	3.69	16.24	-	-	-	-	-	-
	(0.001)	(0.64)	(0.64)						
G70.33+1.59	0.343	-19.18	12.59	0.032	-20.14	10.12	0.025	-21.67	3.28
	(0.001)	(0.05)	(0.05)	(0.001)	(0.44)	(0.46)	(0.002)	(0.33)	(0.33)
G70.29+1.60	0.545	-26.97	17.82	0.042	-26.32	14.53	0.032	-24.78	4.71
	(0.001)	(0.12)	(0.09)	(0.001)	(0.64)	(0.68)	(0.002)	(0.36)	(0.42)
	0.066	-64.41	13.12	-	-	-	-	-	-
	(0.002)	(0.70)	(0.50)						
G61.48+0.09	0.566	25.96	11.16	0.046	28.80	7.86	0.059	21.27	2.48
	(0.001)	(0.02)	(0.02)	(0.001)	(0.24)	(0.24)	(0.002)	(0.11)	(0.11)

^a Some H lines were fit with two gaussian components, in which case the second fit component is on the second line below. Errors (1σ) are indicated by the numbers in parentheses on the line below the measurement.

5. RESULTS

5.1. Derived Properties

The average properties of the spectral line components associated with the UCH II regions and the other spectral

lines representing molecular clouds are shown in Table 8. The table includes the mean and median only of spectral lines with both $1_{10} - 1_{11}$ and $2_{11} - 2_{12}$ detections that yielded measurements of density; upper and lower limits are not included. The full results are presented in Table 5.

Table 8
Inferred properties

Parameter	UCH II			Other Lines (GMC)			
	Median ^a	Mean ^a	RMS ^a	Median ^b	Mean ^b	RMS ^b	KS PTE
$\log(\text{H}_2 \text{ Density}) (\text{cm}^{-3})$	4.95	4.91	0.27	4.49	4.61	0.32	0.022
$\log(\text{o-H}_2\text{CO Column}) (\text{cm}^{-2})$	12.59	12.59	0.44	11.86	11.83	0.20	6×10^{-6}
$X(\text{o-H}_2\text{CO})$	-10.84	-10.80	0.46	-11.16	-11.26	0.45	0.028

^a Spectral line components associated with UCH II regions

^b Other spectral lines (associated with line-of-sight molecular clouds)

There is statistical evidence that the deepest spectral line components have higher H_2CO column and/or abundance than the other (GMC) components (Table 8). It is unlikely that this difference could be caused by underestimates of the optical depths in the GMC components (type 2 and 4 errors, see Table 6) because the filling factor correction should tend to cancel out these errors.

However, it is possible that, in those cases where the H II emission and the CMB emission in the beam are the same order of magnitude, type 1 errors have occurred: the H II region absorber is much larger than the H II region and a significant fraction of the spectral line depth comes from absorption against the CMB; this error should have little effect on the derived density (see Figure 6) but may lead to overestimates of the derived column density.

Each identified Gaussian component was associated with an UCH II region if it was within 5 km s^{-1} of the

RRL peak, since RRLs are assumed to be generated in the UCH II regions. Any spectral lines blended with the UCH II H₂CO lines were also associated with the UCH II region. Other velocity components, including those without corresponding RRL detections, were assumed to be from GMCs along the line of sight or part of the larger cloud not directly associated with the UCH II region; 29 components were associated with UCH II regions and 46 were associated with unrelated line-of-sight GMCs (Table 3).

The density difference between the two populations is significant by a Kolmogorov-Smirnov (KS) test with $\sim 2\%$ probability of being drawn from the same distribution (the ‘probability to exceed’ or PTE in Table 8). This result is in contradiction to the results of Wadiak et al. (1988), who found no significant density difference between “warm clouds” and “cold clouds” selected and observed in the same manner (though with larger beams). The difference is likely because the larger beam sizes in their study and a failure to include the continuum contribution of the CMB (which is more substantial in a larger beam, especially at 2 cm), resulting in a type 3 error and an underestimate of density for their “warm clouds” in particular.

The measured H₂ densities do not display any trend with heliocentric distance over the range 2-14 kpc, contrasting with mm-continuum surveys of star forming regions that tend to measure lower densities at greater distances (Reid et al. 2010). The lack of correlation in Figure 9 demonstrates the strength of the H₂CO densitometry method: the properties of star-forming gas can be explored throughout the galaxy with distance bias largely removed. Similarly, no trend with Galactocentric distance was readily apparent.

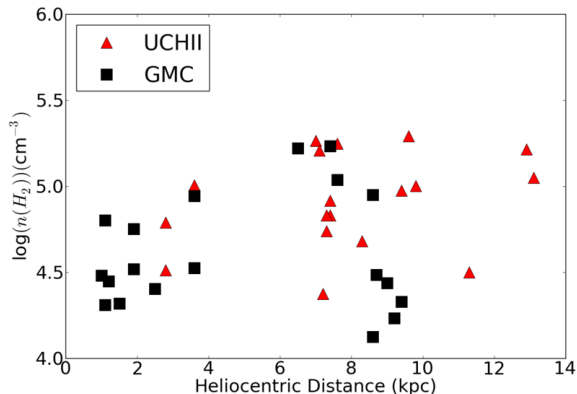


Figure 9. Derived density plotted against kinematic distance. No trend is obvious, demonstrating that the H₂CO densitometer is not biased by source distance. Black squares represent GMCs along the line of sight; red triangles represent UCH II regions.

Densities were measured within a range $10^4 \text{ cm}^{-3} \lesssim n(\text{H}_2) \lesssim 10^6 \text{ cm}^{-3}$ due to sensitivity cutoffs at low densities and thermalization of the spectral line ratio (ratio $\rightarrow 1$) at high densities (see Section 6.5 for a discussion of the limitations of the densitometer). On the high density end, a lower limit on the density remains interesting, as densities $n(\text{H}_2) \gtrsim 10^6 \text{ cm}^{-3}$ are close to those of low-mass protostellar cores and are a strong indication of runaway gravitational collapse, since such high densities are rarely observed in non-star-forming regions. On the low density

end, it should be possible to detect the $2_{11} - 2_{12}$ transition with sensitivity improvements $\sim 2 - 10\times$, a consideration that will govern the allocated time-on-source for future $2_{11} - 2_{12}$ observations.

5.2. Free-free Contribution to 1.1 mm Flux Density Measurements

It is expected that all young star-forming regions should be dust-rich and therefore bright at 1.1 mm. We therefore compare the BGPS 1.1 mm, GBT 2 cm, and Arecibo 6 cm continuum measurements for sources covered by the BGPS in Figure 10. For a flat-spectrum ($\alpha \approx -0.1$, $\tau_{ff} \ll 1$; Wilson et al. 2009) free-free continuum source, the 2 cm flux density should be $1.34\times$ the 1.1 mm flux density. For an optically thick source, $S_{1.1\text{mm}} = 330 S_{2\text{cm}}$.

The objects targeted in our survey include 9 of the 13 brightest ($S_{1.1\text{mm},40''} > 1.5 \text{ Jy}$) sources in the range $32 < \ell < 48$, and 11 of 26 with $S_{1.1\text{mm},40''} > 1.0 \text{ Jy}$. We use flux density measurements from the $40''$ apertures in the BGPS catalog because they are most appropriate for determining peak brightness of point-like sources (Rosolowsky et al. 2010). Out of the sample within the BGPS survey area, 6 of 15 sources have free-free fractions of at least 30%, but potentially much higher if the free-free emission is not optically thin. Since the sample was selected from well-known UCH II regions, these (rather incomplete) statistics are a warning that most of the brightest 1.1 mm emission sources in the BGPS are likely to be active UCH II regions and therefore may include a significant contribution from free-free emission to their measured flux densities (Figure 11). The same warning applies to other mm-wavelength galactic plane surveys, though the contamination should be less severe at shorter wavelengths.

In order to evaluate the impact of this conclusion on the BGPS, we examine the flux distribution of 6 cm continuum sources from the MAGPIS survey compared to the BPGS in the same area, $5 < \ell < 42$ and $|b| < 0.42$, which is the full range of the MAGPIS survey excluding the galactic center, where the BGPS catalog follows a different flux distribution (Bally et al. 2010).

In Figure 12, we plot histograms of the MAGPIS 6 cm flux density and the BGPS $40''$ aperture flux density along with the best-fit power-law distribution line¹². Since the 6 cm power-law distribution is shallower than the 1.1 mm distribution, the 6 cm sources can dominate at high flux densities, although the power-law fit for the 6 cm sources significantly overpredicts the highest-flux bins and therefore the power-law is not an acceptable fit above $S_{6\text{cm}} > 1 \text{ Jy}$ ¹³. The dashed line in Figure 12

¹² The power law was fit using the python translation of the Clauset et al. (2009) power-law fitter provided at <http://code.google.com/p/agpy/wiki/PowerLaw>. The fitter computes the maximum likelihood value of the power-law α and the cutoff of the distribution, below which a power law is no longer valid either because of incompleteness or a change in the underlying distribution.

¹³ We have tested the consistency of the two data sets with a low-cutoff power-law distribution by the Monte-Carlo process described in Clauset et al. (2009). The BGPS $40''$ aperture flux densities are consistent with a power-law distribution at the $p = 0.64$ level, while the MAGPIS 6 cm fluxes are inconsistent, with $p < 0.001$ (where p measures the probability that the data are drawn from a low-cutoff power-law distribution)

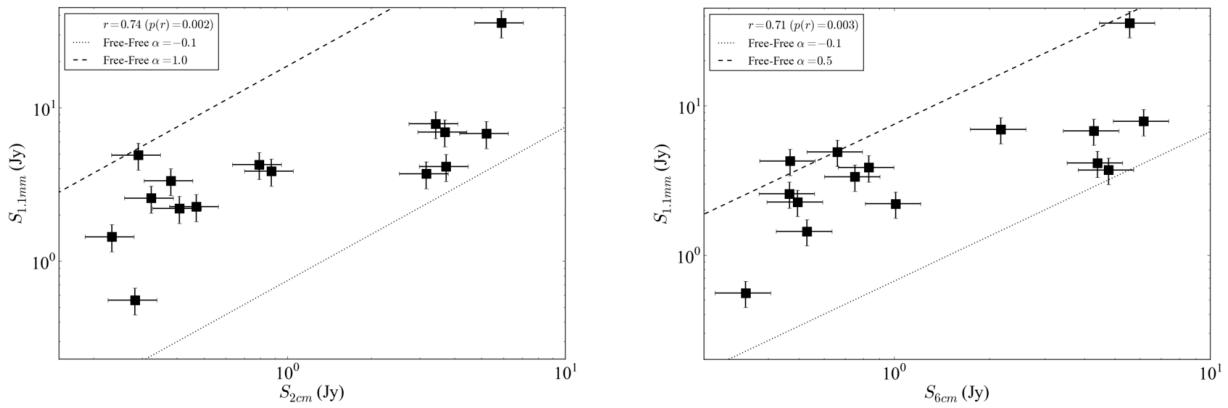


Figure 10. Bolocam 1.1 millimeter flux density versus the cm continuum flux density at 2 cm (left) and 6 cm (right). The BGPS 1.1 mm flux density is moderately correlated with both cm continuum measurements; the legend shows the regression parameter. The expectation for optically-thin free-free emission ($\alpha = -0.1$, dotted) and for intermediate spectral index emission ($\alpha > 0$, dashed) are shown to illustrate that some sources have significant free-free contributions at 1.1 mm (the optically thick case is not shown for either 2 or 6 cm because it does not fit on the plot). The legend shows the predicted flux densities for a given spectral index α , the regression parameter r , and its likelihood p . The brighter sources are likely to be less optically thick in the free-free continuum than the faint sources.

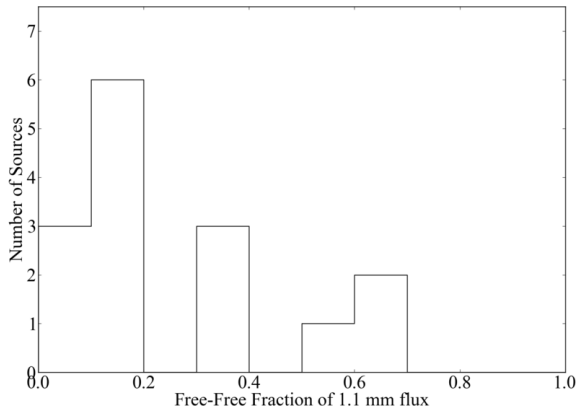


Figure 11. The distribution of free-free contributions to the 1.1 mm flux density assuming the UCH II region is optically thin at 2 cm, $f_{ff} = (S_{2cm}/1.34)/S_{1.1mm}$. While 9 sources are either dust-dominated or optically thick at 2 cm, 6 sources have free-free contributions of 30% or greater. The other sources in the sample were missing 1.1 mm flux density measurements because they are outside the BGPS survey area.

shows the best-fit power-law distribution of the MAGPIS flux densities scaled down by 0.67, which is the expected decrement for an optically thin free-free source from 6 cm to 1.1 mm (spectral index $\alpha = -0.1$).

Figure 12b shows the ratio of the BGPS to the MAGPIS best-fit power-law distribution, indicating that the free-free contamination fraction is only large ($\sim 10\%$) at values much greater than the valid range of the 6 cm power law fit, which overpredicts the number of sources at $S_{6cm} \approx 1$ Jy. However, if any of these sources are *not* optically thin at 6 cm, this fraction could be much larger. Additionally, these numbers only describe the sources in which *all* of the 1.1 mm flux is free-free emission; the implication remains that a large number of 1.1 mm sources have a substantial (if not dominant) free-free contribution.

Finally, we emphasize that unless a large fraction of 6 cm sources are optically thick in free-free continuum, the lower flux-density BGPS dust-continuum sample should be negligibly contaminated by free-free emission sources, but the brightest BGPS sources may have a significant free-free contribution.

5.3. Distances

We measure a kinematic distance to each source using the Reid et al. (2009) rotation curve. We resolved the Kinematic Distance Ambiguity (KDA) towards each line of sight using a variety of methods described below. The method in Sewilo et al. (2004) allows a resolution in favor of the far distance for UCH II regions with an intervening molecular absorption line at more positive velocities in the first Galactic quadrant. Associations with infrared dark clouds (IRDCs) can resolve the KDA in favor of the near distance. We compare our KDA resolutions to Anderson et al. (2009), with whom we agree on all common sources except for G33.13-0.09, which we place at the far distance based on the Sewilo et al. (2004) method. The derived distances are listed in Table 3.

5.3.1. Size Estimates

We estimate the source size using two methods. First, we use the VLA measurements of UCH II region sizes. As stated in Section 4.1, the VLA size measurements are very uncertain and are simplifications of an evidently complicated geometry. We estimate a spherical radius $r = \sqrt{area/\pi}$. Second, we assume the gas traced by H_2CO and the BGPS 1.1 mm images are the same and get a ‘size scale’ $r = 2N_{mm}(H_2)/n(H_2)$ where $n(H_2)$ is derived from the H_2CO line ratio.

The sizes derived from the two methods are plotted against each other in Figure 13. The sizes estimated from the two different methods are not well correlated and disagree by around an order of magnitude in most sources. The disagreement could be because of poor VLA-based size estimates, substantial 1.1 mm emission from low-density gas, or incorrect dust temperature or opacity estimates. While additional line-of-sight GMCs could in principle contribute to the N/n size estimate, the disagreement for sources even without associated GMCs prevents this hypothesis from fully explaining the disagreement. Therefore, any quantities derived from the size - i.e. mass, which depends on r^3 - are even less constrained. We therefore do not derive any quantities dependent on the intrinsic source size.

6. DISCUSSION

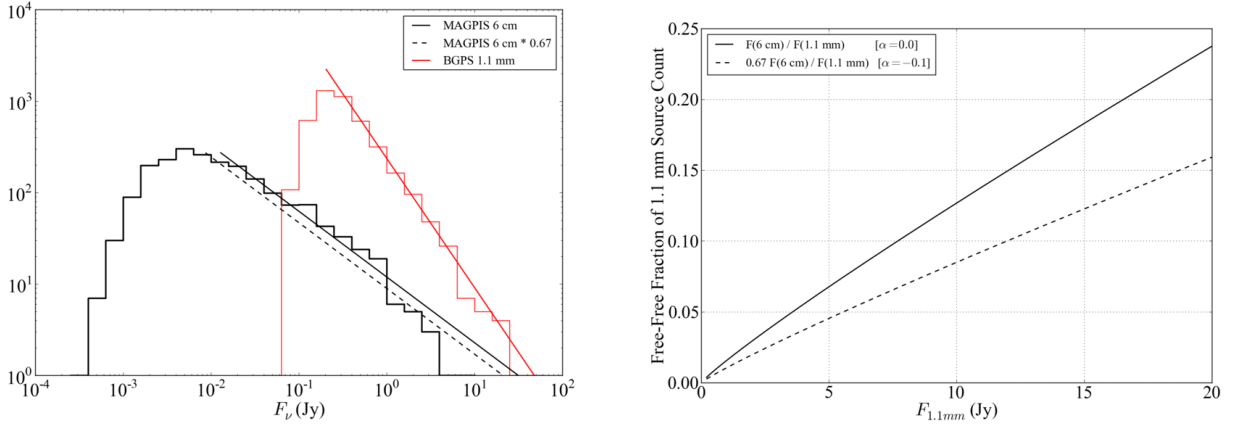


Figure 12. *Left:* Histograms of BGPS 1.1 mm 40'' aperture flux densities (red) and the MAGPIS 6 cm flux densities (black), and their respective best-fit power-law distributions ($\alpha(1.1\text{mm}) = 2.41 \pm 0.03$, $\alpha(6\text{cm}) = 1.72 \pm 0.03$). The dashed black line shows the MAGPIS best-fit power-law scaled down to the expected flux density at 1.1 mm assuming all sources are optically thin. Both distributions appear to be reasonably well-fit by power-laws above a cutoff (presumably set by completeness), although the power-law significantly over-predicts the number of sources with $S_{6\text{cm}} > 1\text{Jy}$. The histograms are binned by 0.1 dex, and while the best-fit α and x_{min} values are independent of the binning scheme, the normalization is not. *Right:* The ratio of the number of MAGPIS 6 cm sources to BGPS 1.1 mm sources as a function of flux density for the best-fit power laws. Only 10 1.1 mm sources are detected above 5 Jy (in 40'' apertures), so even the brightest detected 1.1 mm sources are not purely free-free, but they probably have a substantial free-free component.

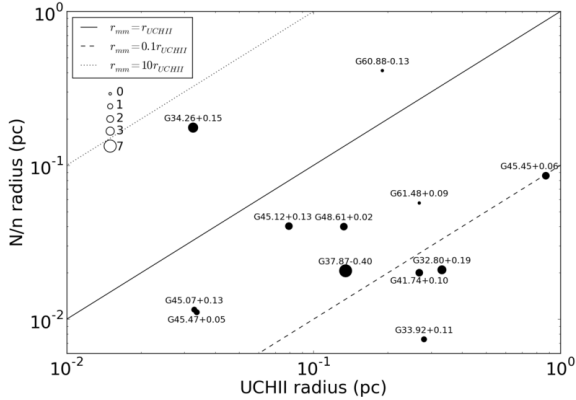


Figure 13. A plot of the two derived sizes discussed in Section 5.3.1. The two size estimates are at best very weakly correlated. Because of the substantial disagreement between the two methods, we choose not to explore any parameters with a strong dependence on the size. The plotted point size indicates the number of associated line-of-sight GMCs, which in principle could lead to an overestimate of the N/n size because of additional mass included in the 1.1 mm continuum measurement.

6.1. Comparison to extragalactic observations

We compare our measured column and volume densities to a selection of starburst galaxies from Mangum et al. (2008) in Figure 14. All of the extragalactic observations have much lower column densities per km s^{-1} than we measure in the main lines of most UCH II regions, but similar volume densities. This discrepancy can be easily explained by a difference in the area filling factor of molecular clouds in observations of galaxies and UCH II regions. In a galaxy, the total area filling factor of molecular clouds per km s^{-1} (which is similar but not identical to the volume filling factor) is likely to be < 1 , even in extreme starbursts; although the galaxy may appear to be uniformly filled with molecular gas in projection, at any given velocity it is likely to have significant gaps of ionized or neutral atomic gas. In contrast, an UCH II region should be completely embedded in a molecular cloud that is much larger than the free-free emitting continuum region, so the covering factor of

molecular gas should be ~ 1 .

It is therefore interesting to note that Arp 220, possibly the most extreme nearby example of a starburst galaxy, has nearly the same column per channel as the low end of the UCH II regions, suggesting that it is analogous to a scaled-up UCH II region to within a factor of a few; the measured density in Arp 220 is consistent with only the highest-density UCH II regions. M82, on the other hand, has a bright continuum background analogous to an UCH II region, but a correspondingly low filling factor, implying that it consists of many compact but bright sources with a total filling factor 0.001-0.1. Alternatively, the density and column measurements are consistent with M82 being dominated by quiescent GMCs, but that is unlikely given the starburst nature of the galaxy.

The gravitational lens source B0218+357 is a different scenario. Its low density is consistent with that of a non-star-forming GMC, while its column per km s^{-1} is comparable to the Galactic sample. This source is therefore likely to be a sightline through a ‘normal’ quiescent molecular cloud in its host galaxy, similar to the narrow beam of an UCH II region through the Galactic disk. Zeiger & Darling (2010) note that there is a range of covering factors cited in the literature, which can affect the measured density and column, but should not affect the conclusion that the B0128+357 cloud’s density is not consistent with that of massive-star forming regions. The low-density gas is detected partly because the Zeiger & Darling (2010) data are $3.5\times$ more sensitive than ours with a background continuum source of similar brightness.

6.2. Line Profiles

Despite the many systematics discussed above that can affect H₂CO absorption measurements with a compact illumination source, it is possible to directly compare the properties of gas along a given line of sight without most of these hindering factors. Since most of our spectra have kinematically resolved spectral line profiles, it is possible to make many density measurements at different velocities towards each source. An example of this type of anal-

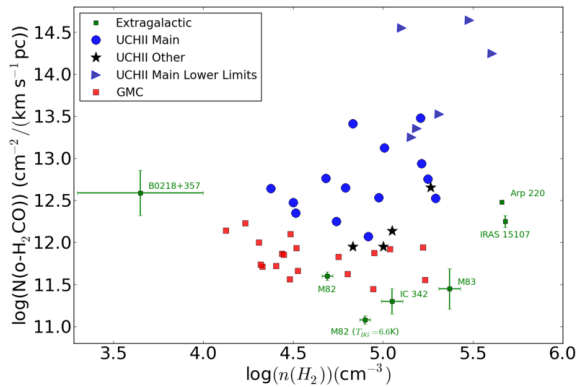


Figure 14. Comparison of the UCH II sample (blue circles are measurements, blue triangles are lower limits on volume density with poorly constrained column densities), the GMC sample (red squares), secondary lines associated with UCH II regions (black stars) and the extragalactic sample of Mangum et al. (2008) (green squares). The errorbars on the Galactic data points are excluded for clarity. The observed galaxies have similar densities to the Galactic UCH II sample, but significantly lower column densities, suggesting that the molecular gas in these galaxies has a filling factor $\ll 1$. The lack of direct density measurements of UCH II regions at high densities is due to the presence of a dominant background source; in Arp 220 a direct measurement of density was possible because H_2CO was seen in emission.

ysis is shown in Figure 15. An example demonstrating the need for this type of analysis is shown in Figure 16, in which two lines well-fit by gaussian profiles nonetheless display a density gradient because the line centers are significantly offset; the figure also demonstrates that the offset cannot be accounted for by any instrumental effects.

Of our sample, 18 of the 24 observed lines-of-sight had high enough signal-to-noise spectra ($S/N \gtrsim 5$ in at least four adjacent 0.4 km s^{-1} channels in both lines) to measure the density in many velocity bins. Of these, 12 have different peak velocities in the $1_{10} - 1_{11}$ and $2_{11} - 2_{12}$ lines, indicating density gradients in the molecular gas with velocity. Figure 15b is an example density-velocity plot.

We have classified each high S/N spectrum as *gradient*, *envelope*, or *single* based on spectral line morphology. The *gradient* classification was used for gaussian or nearly gaussian lines in which the $1_{10} - 1_{11}$ and $2_{11} - 2_{12}$ line centers were offset, indicating a gradient in the density with velocity; the color listed in the table indicates the direction of *increasing* density. The *envelope* classification was used for flat profiles on the wings of deeper gaussian lines. The *single* classification was used for lines where the $1_{10} - 1_{11}$ and $2_{11} - 2_{12}$ velocities matched. Low S/N spectra were not classified. Classifications are given in Table 3.

Of the 12 sources with density gradients, 6 show an increased density towards the red and 5 towards the blue. One source, G45.12+0.13, shows a slight increase towards the red over a broad (8 km s^{-1}) velocity range, but a sharp increase towards the blue over only 1 km s^{-1} and is therefore classified as *other*.

Figures 23-40 show the ‘main line’ (associated with the UCH II region) profile and the associated density, column, and abundance velocity profiles. The density, column, and abundance measured for each main line via the gaussian fit technique are shown overplotted on the

profiles with blue squares. In all cases, the gaussian fit measurement of density is consistent with the individual channels nearby and the gaussian fit measurements of column and abundance are consistent with the peak column and abundance. The consistency of adjacent velocity bins confirms the validity of associating gaussian components in observations of whole galaxies (e.g., Mangum et al. 2008) or kpc-scale regions, since on these scales the $1_{10} - 1_{11}$ and $2_{11} - 2_{12}$ lines should be blended by kinematics to have the same shape.

6.3. Comparison of RRLs and H_2CO lines

We compare the density spectra with the fitted RRL centroids and attempt to interpret these spectra in the context of various simple models of H II region interaction with molecular clouds. The simple models described below may actually be short-lived but recurring stages in the normal life cycle of a collapsing clump that is forming massive ($M \gtrsim 10M_{\odot}$) stars (Peters et al. 2010).

We consider five simple models of embedded UCH II regions. For each scenario, we include a brief description of the model and an analysis of the observational consequences in terms of C and H RRL velocities and velocity-density structure. We assume that the carbon RRLs are only detected if seen in the foreground of a bright source. This assumption is based on predictions that C RRLs will be amplified by an order of magnitude even in the presence of a weak background (Natta et al. 1994). It is backed by a strong correlation between the continuum and the C RRL intensity (Roshi et al. 2005). We also assume that lower-frequency RRLs will have a stronger stimulated emission component than higher-frequency RRLs (Lockman & Brown 1978). All H_2CO absorption is assumed to be against the UCH II region in this section. The scenario that describes a given spectrum is listed in the figure caption for each spectrum and in Table 3.

- SCENARIO 1: STATIC

In a uniform medium with no bulk motions (i.e., no collapse), a massive star ignites and generates an expanding H II region. Figure 17.

1. Lower frequency RRLs are blueshifted from higher-frequency RRLs because of an increased stimulated emission component (Lockman & Brown 1978)
2. A carbon RRL should be seen at the same velocity as or blueshifted from the hydrogen RRL line center.
3. Molecular gas closest to the H II region should have the highest density because of compression by the expanding H II region. It will be at a similar velocity or blueshifted from the H RRLs.

- SCENARIO 2: COLLAPSE

A massive star ignites while spherically accreting from a molecular cloud undergoing bulk (inside-out) collapse. Figure 18.

1. The H_2CO -measured density should peak at the velocities most redshifted relative to the

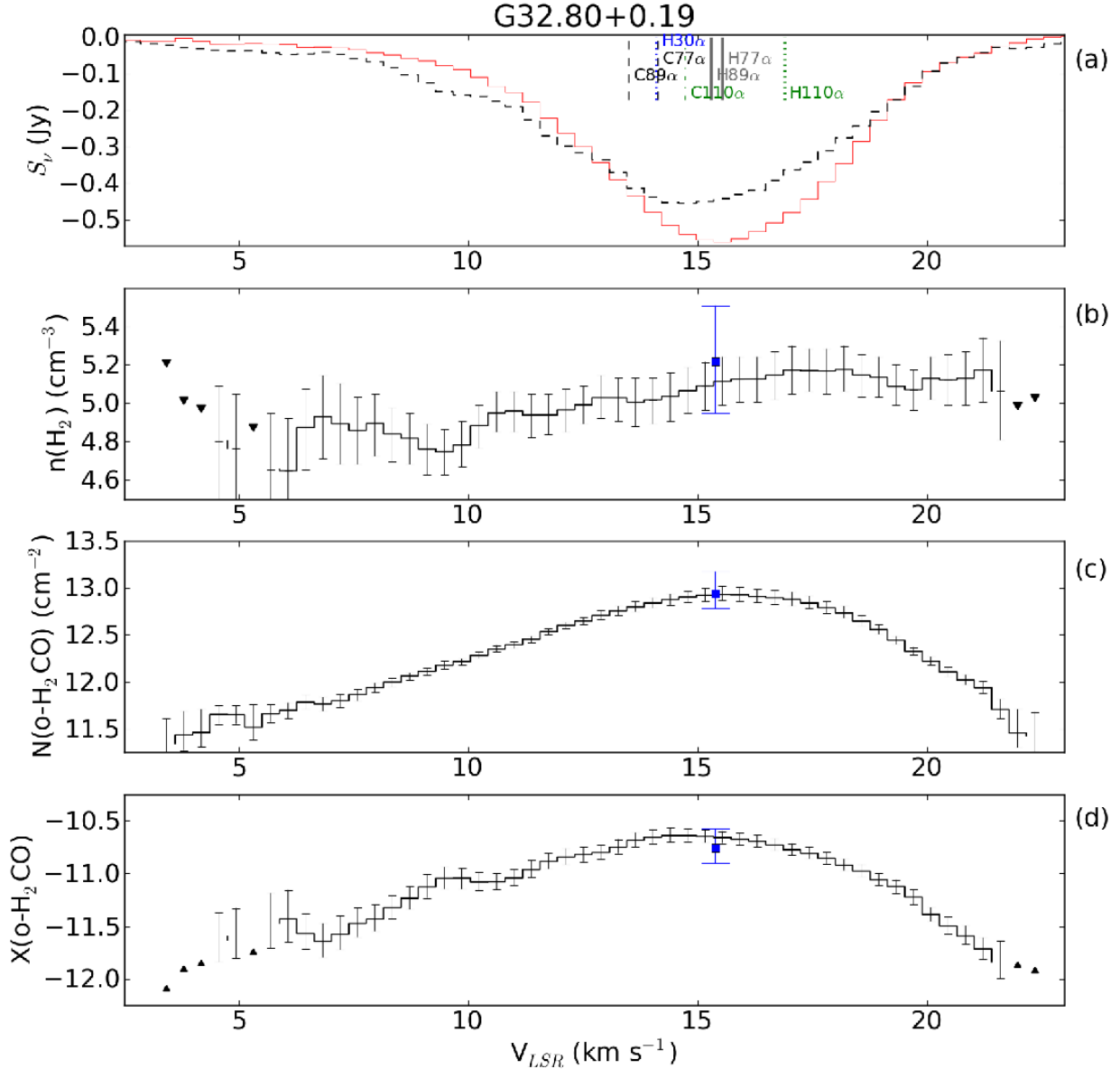


Figure 15. Plot of the derived parameters per velocity bin for the main line of G32.80+0.19; the full spectrum is shown in Figure 1. The density peak around 16 km s^{-1} is slightly redshifted of the H and C RRL velocity centers, although the C RRLs are blueshifted of the H RRLs, indicating that the PDR has been accelerated towards us along the line of sight. The blueshifted emission tail is suggestive of an outflow. This source cannot therefore be easily classified under any of the scenarios in Section 6.3, but is consistent with components of scenarios 2 and 3.

a. The spectra of G32.80+0.19. The GBT $2_{11} - 2_{12}$ spectrum (red solid) has been smoothed to a resolution of 0.38 km s^{-1} to match the Arecibo (black dashed) spectral resolution. Labeled vertical bars indicate the measured velocity centers of H and C RRLs from this work, Roshi et al. (2005), and Churchwell et al. (2010).

b. The measured densities in each spectral bin. The Y-scale is in \log_{10} units. Error bars include a 10% systematic uncertainty in the continuum and therefore errors in adjacent channels are not independent. Limits are indicated by triangles. Bins with no information above the $1\text{-}\sigma$ noise cutoff are left blank. The increase of density towards higher velocities led us to classify this source as a *red gradient* in Table 3.

c. The measured column densities per spectral bin. Because these column densities are derived from a large velocity gradient code, they are in per $\text{km s}^{-1}\text{pc}^{-1}$ units.

d. The measured abundances per spectral bin. The column and abundance are somewhat degenerate, but it is possible in some cases to place tight constraints on the total o-H₂CO column while only placing upper limits on abundance and density. The abundance must also be interpreted per $\text{km s}^{-1}\text{pc}^{-1}$.

In plots *b* through *d*, the blue square with error bars represents the measured value from Table 5 using gaussian fits to the lines.

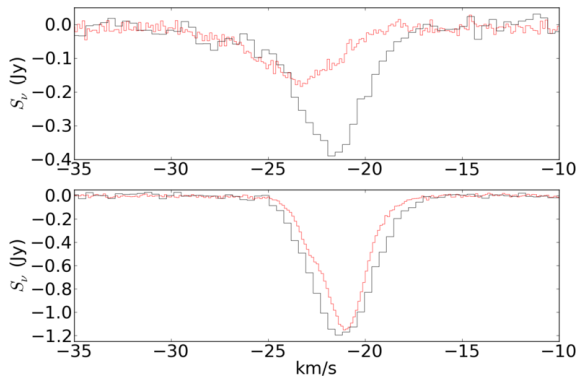


Figure 16. Comparison of G70.29+1.60 (top) and G70.33+1.59 (bottom) spectra as observed by Arecibo (black) and GBT (red/grey). Note that in G70.29+1.60, the $2_{11} - 2_{12}$ line is shifted towards the blue of the $1_{10} - 1_{11}$ line, while in G70.33+1.59 the line centers match well.

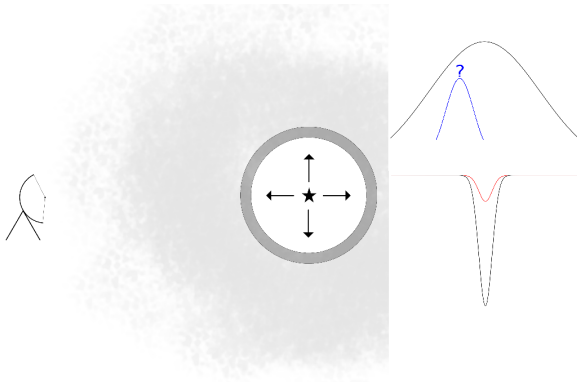


Figure 17. Scenario 1: An UCH II region forms and begins expanding spherically in a uniform density gas cloud. A cartoon of the geometry seen by the observer is shown on the left side of the figure, with arrows indicating expansion and darkness of the gray shading indicating relative density. The white region around the central star is the ionized UCH II region. On the right side, a cartoon of the relative velocity and width of the RRLs and H_2CO lines is shown. The relative heights of the H_2CO lines is representative of the observed density; black is $1_{10} - 1_{11}$ and red is $2_{11} - 2_{12}$. The narrow emission line with a ? above it indicates a possible blueshifted carbon RRL; its height has no physical meaning. In this scenario, the hydrogen recombination and H_2CO lines should occur at the same velocity, and the H_2CO lines should show relatively low-density (high $1_{10} - 1_{11}/2_{11} - 2_{12}$ ratio) and modest spectral line widths. A blueshifted carbon RRL may form, but is not guaranteed.

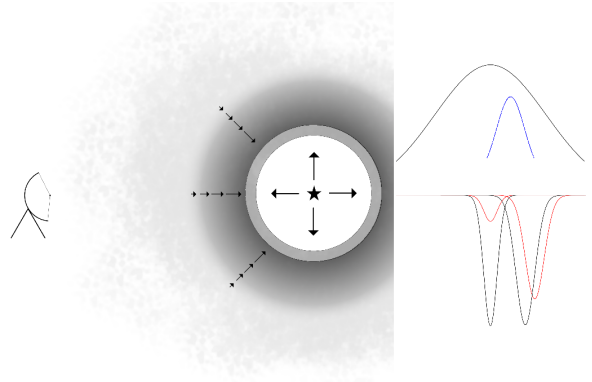


Figure 18. Scenario 2: An UCH II region forms from a gravitationally unstable cloud undergoing inside-out collapse. See Figure 17 for a complete description of the figure. The highest density should correspond to the highest-velocity infall, so the $2_{11} - 2_{12}$ line peak should be redshifted of the $1_{10} - 1_{11}$ line peak. The hydrogen recombination line may align with a low-density cloud but should be blueshifted of the infalling gas. The carbon RRL should be redshifted from the hydrogen RRL and blueshifted from the H_2CO line.

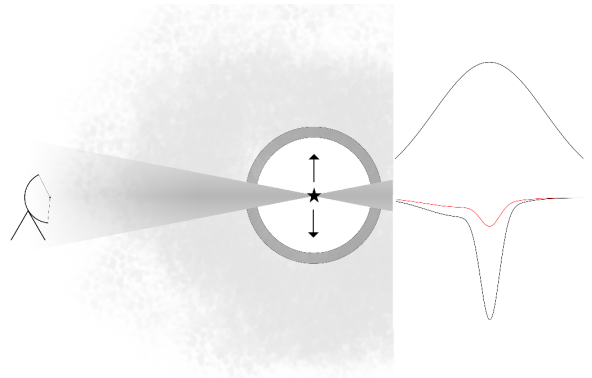


Figure 19. Scenario 3: An UCH II region expanding in a uniform medium ejects a bipolar outflow. Presumably the bipolar outflow comes from a disk-accreting source. See Figure 17 for a complete description of the figure. The outflow (indicated by the cones emitting from the central source) should have lower column density but could have high or low volume density. It will be observed as high-velocity blueshifted absorption in a line wing. Carbon recombination line emitting regions may be destroyed by the outflowing material. As in the simple scenario 1, the hydrogen recombination line should be at the same velocity as the molecular cloud.

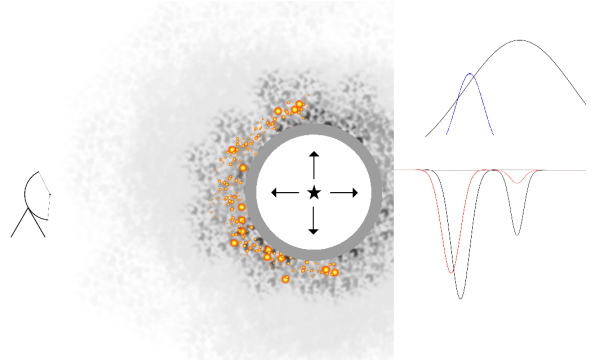


Figure 20. Scenario 4: An UCH II region expanding in a uniform medium sweeps up and accelerates material that undergoes triggered star formation. Because the highest-density material is the swept up material, it should be the most blueshifted. See Figure 17 for a complete description of the figure. The orange and yellow circles are meant to indicate triggered star formation.

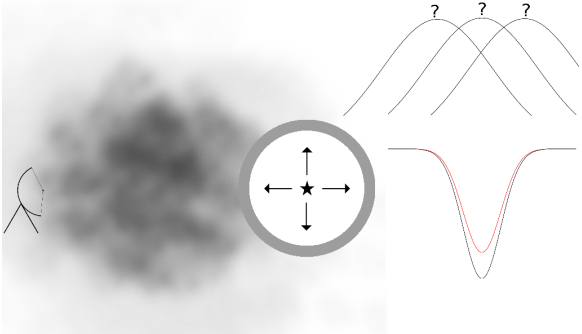


Figure 21. Scenario 5: An UCH II region is seen behind a high-density, turbulent gas cloud. The turbulence drives large spectral line widths, while the high density makes the $1_{10}-1_{11}$ and $2_{11}-2_{12}$ line depths very close. The RRL velocity could in principle be at any velocity relative to the foreground turbulent cloud. See Figure 17 for a complete description of the figure. In this case, the ?’s indicate an uncertain velocity for the hydrogen RRLs; a carbon RRL is not expected because the H II region is not necessarily interacting with the molecular gas.

hydrogen RRLs. Inside-out collapse dictates that the highest densities should be infalling at the highest speeds.

2. The C RRL velocity should be between the H₂CO and H RRL velocity since the PDR will be decelerated by radiation and gas pressure from the H II region
 3. Since the accreting star should be at approximately the rest velocity of the cloud, there should be little to no gas blueshifted from the RRL velocity
- **SCENARIO 3: OUTFLOW**
An accreting massive star generates a massive outflow with a significant component along the line of sight. Figure 19.
 1. Substantial low-column, low-abundance per km s⁻¹ gas should be observed at velocities blue of the RRL velocities. Densities can range from low to high. Covering factors may be low.
 2. No carbon RRL is expected from the outflow, though if the flow is accelerated by ionization pressure a C RRL should be observed blueshifted of the H RRL velocity.
 - **SCENARIO 4: SWEEPING**
An expanding H II region pushes on a low-density envelope, possibly triggering a new stage of star formation as in the “collect and collapse” scenario. This scenario is similar to #1 but with either a higher-density envelope or with more gas swept up (i.e., #4 may represent a more evolved region). Figure 20.
 1. The hydrogen RRLs should be red of the dense gas and the carbon RRLs. The expanding H II region should accelerate the dense gas blue along the line of sight.
 2. A low-density envelope should persist at the same velocity as the H II region

- **SCENARIO 5: FOREGROUND CLUMP**

A high density, highly turbulent or high mass and rotating clump of gas is in front of the UCH II region or surrounds it. This physical situation may exist in all of the above and provides alternate explanations for any spectral line wings. Figure 21.

1. Moderate density gas from a molecular cloud will result in high column but moderate density at the center velocity
2. Wide wings of high density gas will exist both blue and redshifted of the highest-column point

6.4. The Filling Factor of Molecular Clouds

We have measured the density in 19 line-of-sight molecular clouds in addition to the 18 measurements of densities around UCH II regions (we only include measurements, not limits, in these counts). The measured density from the H₂CO line ratio can be compared to other measures of density, e.g. the mean molecular cloud density measured by Roman-Duval et al. (2010) from the BU-FCRAO GRS. It is clear from Figure 22 that the average density in GMCs is typically $\sim 2-3$ orders of magnitude lower than densities measured in our sample of line-of-sight GMCs.

Roman-Duval et al. (2010) point out that the mean densities they measure are significantly below the critical density of ¹³CO, $n_{cr} = 2.7 \times 10^3$ cm⁻³, indicating that they do not resolve the high-density clumps that make up the GMCs. Our data indicate that a typical GMC consists of $n \sim 3 \times 10^4$ cm⁻³ gas (the median of our GMC subsample excluding upper limits), substantially higher than the critical density of ¹³CO. Taking the ratio of the median density in the Roman-Duval et al. (2010) catalog to that in our sample, we derive a volume filling factor of 5×10^{-3} of dense gas in molecular clouds.

We measured an additional 20 upper limits towards GMCs, all of which are consistent with high densities ($n(\text{H}_2) > 10^4$ cm⁻³), but could represent a sample of lower density ($n(\text{H}_2) \sim 10^3$ cm⁻³) gas, in which case our ‘measurement’ of the cloud volume filling factor is biased to be too low. In order to test for this bias, we need to acquire more sensitive observations of the upper-limit systems. However, we continue analysis below based on the assumption that the cloud filling factor measurement is realistic, i.e. assuming that the density upper limit measurements have densities consistent with the other observed GMCs.

Can a medium with supersonic turbulence produce the same density measurements without having to invoke high-density clumping? Below about $n(\text{H}_2) \approx 10^5$ cm⁻³, measurements of density in a turbulent medium are biased towards higher densities, i.e. the densities we report may be overestimates for GMCs since they have a median density $n(\text{H}_2) = 10^{4.49}$ cm⁻³. For turbulent density PDFs with logarithmic widths $\sigma_{\ln(\rho)/\ln(\bar{\rho})} \lesssim 1.5$, the overestimate is no more than 0.4 dex, and therefore can only bring the filling factor up by a factor < 3 . As discussed in Section 3.1 and Figure 4, a high-density tail could create a larger discrepancy (~ 0.5 dex). However, at the measured densities, these are extreme upper limits on the ‘turbulent correction’, and therefore

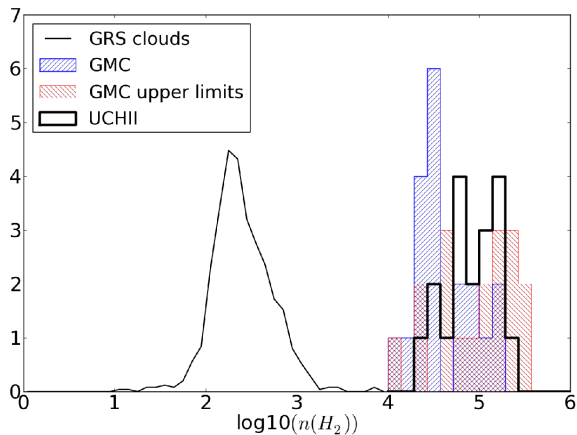


Figure 22. Histograms of the GMC and UCH II subsamples from our data plotted along with the GMC-averaged densities from the ^{13}CO Roman-Duval et al. (2010) GRS measurements arbitrarily scaled to fit on this plot. The measured densities in UCH II regions are significantly (by a KS test) higher than densities in GMCs. The H_2CO -measured densities in GMCs are 2-4 orders of magnitude higher than volume-averaged densities of GMCs from the GRS, suggesting that GMCs consist of very low volume-filling factor ($\sim 5 \times 10^{-3}$) high-density ($n(\text{H}_2) \sim 3 \times 10^4 \text{ cm}^{-3}$) clumps. In Section 6.4, we argue that the observed difference is most likely not a selection effect imposed by the different gas tracers. The GMC upper limits shown are $3 - \sigma$ upper limits, and all are consistent with the measured GMC densities.

(gravo)turbulence alone cannot account for the measured densities.

What clumping properties are required to reproduce the observed density? As long as the clumps are all optically thin in the H_2CO absorption lines, the spectral line optical depths and ratio are independent of clumping. However, a large number of low-density ($n(\text{H}_2) \approx 10^{3.5} \text{ cm}^{-3}$) clumps optically thick in the $1_{10} - 1_{11}$ line and thin in the $2_{11} - 2_{12}$ line would appear to have a higher density. This phenomenon could only occur at densities $\lesssim 10^{4.5} \text{ cm}^{-3}$, where the $1_{10} - 1_{11}$ absorption line is much stronger than the $2_{11} - 2_{12}$ line, and column densities $10^{14} \text{ cm}^{-2} \gtrsim N(\text{o-H}_2\text{CO}) \gtrsim 10^{13.5} \text{ cm}^{-2}$ per clump (at higher columns, both lines are optically thick; at lower columns, both lines are optically thin). Assuming a typical H_2CO abundance (ortho+para) $X_{\text{H}_2\text{CO}} = 10^{-9}$, the required spherical clump radius would be $\sim 0.3 \text{ pc}$, which would be Jeans-unstable at the assumed density and temperature (40 K) and is therefore unlikely to persist for long time periods¹⁴. We therefore regard a collection of optically thick clumps in the H_2CO $1_{10} - 1_{11}$ line to be unlikely; clumps optically thick in both lines are even less likely following the same line of reasoning.

The combination of the observed large spatial scales (and therefore low volume-averaged density) of GMCs and the high densities measured along essentially arbitrary sightlines through these GMCs suggests that GMCs are not consistent with a purely turbulent medium with a lognormal density distribution. The observations also require a more substantial high-density tail than typically seen in gravoturbulent simulations, i.e. they require a clumpier medium.

Alternatively, it is possible that H_2CO is chemically

¹⁴ However, the lifetime of such clumps in a turbulent medium in which small-scale turbulence supports the clumps against collapse is unconstrained.

enriched in high-density pockets within a turbulent medium, which would imply that H_2CO observations probe different gas than CO. No such mechanism has been proposed on theoretical grounds, and the timescales for enhancement would have to be very short (intermittent density enhancement occurs on timescales much shorter than the dynamical timescale; Kritsuk et al. 2007), so we regard this possibility as unlikely but include it for completeness.

Another alternative is that the ^{13}CO systematically underestimates the mass or overestimates the volume of the cloud, resulting in an underestimate of the cloud density. Sub-thermal excitation of ^{13}CO in the low-density parts of the cloud can lead to an underestimate of the mass (Roman-Duval et al. 2010, Section 9.3). Since the cloud sizes were derived using an assumed spherical symmetry, but molecular gas is typically observed in filamentary structures, the densities in Roman-Duval et al. (2010) are likely to be lower limits on the mean density in the molecular gas. While both of these factors bring the H_2CO and ^{13}CO densities into closer agreement, it is difficult to quantify these effects.

6.5. Strengths and Weaknesses of the H_2CO K-doublet Densitometer

The dynamic range of a spectral line as a tracer of a physical quantity is an important consideration when designing an experiment. We have demonstrated only a modest dynamic range in density measurements using the $1_{10} - 1_{11}$ and $2_{11} - 2_{12}$ lines in absorption against bright background sources: above $n(\text{H}_2) \approx 10^{5.6} \text{ cm}^{-3}$, we are only able to set lower limits on the density because the spectral line ratio asymptotes to 1, and below $n(\text{H}_2) \approx 10^4 \text{ cm}^{-3}$, the $2_{11} - 2_{12}$ line optical depth drops to very low levels (Figure 2).

The lower limits on density at $n(\text{H}_2) \gtrsim 10^{5.6} \text{ cm}^{-3}$ can only be modestly improved upon by using higher K-doublet transitions (e.g. $3_{12} - 3_{13}$) when observing H_2CO in absorption against bright continuum sources. However, when observing anomalous absorption against the CMB, an additional density diagnostic is the transition from absorption to emission at higher densities, which expands the sensitivity of the $1_{10} - 1_{11}/2_{11} - 2_{12}$ pair to $n(\text{H}_2) \approx 10^{6.5} \text{ cm}^{-3}$.

The low-density end can only be probed by more sensitive observations of the $2_{11} - 2_{12}$ line. Because the H_2CO line depths become negligible below $n(\text{H}_2) \approx 10^3 \text{ cm}^{-3}$, the densitometer is not a useful probe below these densities. However, at such low densities, even within a molecular cloud, it is questionable whether any molecular probes are reliable, as even CO will be underabundant in these environments (e.g., Glover et al. 2010).

As noted in Mangum et al. (2008) and Zeiger & Darling (2010), the K-doublet densitometer has the advantage that line detection only depends on the brightness of the background source and the gas density. It can therefore be used nearly independent of distance when observing clouds against the CMB or bright illuminating background sources. The Zeiger & Darling (2010) measurements are more sensitive than any presented in our study because of longer integration times and the selection of a bright illuminating background source despite their target being at a distance $z=0.68$. Following

this line of reasoning, any bright synchrotron or free-free source can be used to sensitively probe the density of a line-of-sight molecular cloud in the Galaxy. The observation will have angular resolution limited only by the size of the background source as long as it is much brighter than the CMB in the beam.

7. CONCLUSIONS

We have presented a pilot study to measure molecular gas densities in clouds along 24 lines of sight in the H₂CO 1₁₀ – 1₁₁ and 2₁₁ – 2₁₂ transitions primarily toward UCH II regions. We have shown that the H₂CO densitometer is robust within reasonable ranges of turbulent density distributions, most cloud geometries, and different cloud clumping properties. We have presented the methodology and discussed the errors intrinsic to the H₂CO densitometer.

Gas volume densities were measured toward 14 of the 24 sources using the best-fit gaussian profiles; density limits were measured for the remaining 10. In 18 sources, it was possible to estimate the density in each 0.4 km s⁻¹-wide channel centered on the main line. Of these, 12 showed some sign of a density gradient with velocity, 5 appeared to have a single-valued density (i.e. only a single spectral line component well-fit by a gaussian), and one, G69.54-0.98, had a spectral line optical depth that was beyond our ability to model.

Velocity-density gradients have been used to fit 18 sources with simple models of UCH II regions embedded in molecular clouds. We have found some examples consistent with inside-out collapse onto the UCH II region, UCH II region expansion, and bulk outflow. H₂CO absorption provides a unique probe of the physical conditions around UCH II regions because it is only seen in absorption against the continuum background (for sources much brighter than the CMB), giving different constraints than mm and sub-mm spectral lines that are seen both in front of and behind the UCH II region.

The measurements of serendipitously detected line-of-sight GMCs revealed densities ~ 200 times higher than volume-average densities measured using ¹³CO. The high density measured suggests that GMCs consist of many sparsely distributed high-density clumps and have density distributions inconsistent with the lognormal distribution predicted by supersonic turbulent models. The implied density distribution is also more skewed to high densities than predicted by typical gravoturbulent simulations. Alternatively, the ¹³CO-based mean densities may be lower than the mean densities within the molecular gas either because they underestimate the mass or overestimate the volume of GMCs.

The density measurements show that UCH IIs are associated with high-density ($n(\text{H}_2) > 10^{4.5} \text{ cm}^{-3}$) gas, and UCH IIs are associated with higher column and volume densities than other line-of-sight molecular clouds, in contradiction with previous results (Wadiak et al. 1988).

The 6 cm, 2 cm, and 1.1 mm flux density measurements are strongly correlated and in most objects in our sample the 1.1 mm flux density has a substantial (> 30%) contribution free-free continuum emission. This result implies that the brightest sources detected in the BGPS have significant free-free emission. A comparison to the 6 cm MAGPIS survey suggests that the sample of 1.1 mm sources below about 3 Jy is not significantly con-

taminated by pure free-free emission sources.

Comparison of the density measurements in our sample to the starburst sample of Mangum et al. (2008) suggest that the molecular gas volume filling factor in most of these galaxies is small (~ 0.01), but in Arp 220 it is quite high ($\gtrsim 0.1$). The physical properties measured by H₂CO in Arp 220 are similar to those in UCH II regions. Although velocity-density gradients are observed in our sample, we argue that kinematic spectral line blending should uphold the assumption of a single spectral line profile in galaxies as robust for radiative transfer purposes.

8. ACKNOWLEDGEMENTS

We thank Jim Braatz for assistance with data acquisition and processing, Esteban Araya for providing us with reduced data, and our referee Jeff Mangum for a helpful and timely review. This work was supported by the National Science Foundation through NSF grant AST-0708403 to John Bally and AST-0707713 to Jeremy Darling. This research has made use of the SIMBAD database, operated at CDS, Strasbourg, France. This research made use of pyspeckit, an open-source spectroscopic toolkit hosted at <http://pyspeckit.bitbucket.org>.

Facilities: GBT, Arecibo, VLA, FCRAO, CSO

REFERENCES

- Aguirre, J. E. et al. 2011, *ApJS*, 192, 4
 Anderson, L. D., Bania, T. M., Jackson, J. M., Clemens, D. P., Heyer, M., Simon, R., Shah, R. Y., & Rathborne, J. M. 2009, *ApJS*, 181, 255
 Araya, E., Hofner, P., Churchwell, E., & Kurtz, S. 2002, *ApJS*, 138, 63
 Araya, E., Hofner, P., Linz, H., Sewilo, M., Watson, C., Churchwell, E., Olmi, L., & Kurtz, S. 2004, *ApJS*, 154, 579
 Bally, J. et al. 2010, *ApJ*, 721, 137
 Benjamin, R. A. et al. 2003, *PASP*, 115, 953
 Cho, W. & Kim, J. 2011, *MNRAS*, 410, L8
 Churchwell, E. 2002, *Annual Review of Astronomy and Astrophysics*, 40, 27
 Churchwell, E., Sievers, A., & Thum, C. 2010, *A&A*, 513, A9+
 Clauaset, A., Rohilla Shalizi, C., & Newman, M. E. J. 2009, *SIAM Review*, 51, 661
 de Wit, W. J., Testi, L., Palla, F., & Zinnecker, H. 2005, *A&A*, 437, 247
 Dickel, H. R. & Goss, W. M. 1987, *A&A*, 185, 271
 Dickel, H. R., Goss, W. M., Rots, A. H., & Blount, H. M. 1986, *A&A*, 162, 221
 Dunham, M. K. et al. 2010, *ApJ*, 717, 1157
 Federrath, C., Roman-Duval, J., Klessen, R. S., Schmidt, W., & Mac Low, M. 2010, *A&A*, 512, A81+
 Glover, S. C. O., Federrath, C., Mac Low, M., & Klessen, R. S. 2010, *MNRAS*, 404, 2
 Green, S. 1991, *ApJS*, 76, 979
 Helfand, D. J., Becker, R. H., White, R. L., Fallon, A., & Tuttle, S. 2006, *Astronomical Journal*, 131, 2525
 Henkel, C., Walmsley, C. M., & Wilson, T. L. 1980, *A&A*, 82, 41
 Henkel, C., Wilson, T. L., Walmsley, C. M., & Pauls, T. 1983, *A&A*, 127, 388
 Jackson, J. M. et al. 2006, *ApJS*, 163, 145
 Kainulainen, J., Beuther, H., Henning, T., & Plume, R. 2009, *A&A*, 508, L35
 Keto, E. 2007, *ApJ*, 666, 976
 Klessen, R. S. 2000, *ApJ*, 535, 869
 Kritsuk, A. G., Norman, M. L., Padoan, P., & Wagner, R. 2007, *ApJ*, 665, 416
 Lockman, F. J. & Brown, R. L. 1978, *ApJ*, 222, 153
 Mangum, J. G., Darling, J., Menten, K. M., & Henkel, C. 2008, *ApJ*, 673, 832

- Mangum, J. G. & Wootten, A. 1993, ApJS, 89, 123
 McKee, C. F. & Ostriker, E. C. 2007, ARA&A, 45, 565
 Natta, A., Walmsley, C. M., & Tielens, A. G. G. M. 1994, ApJ, 428, 209
 Peters, T., Banerjee, R., Klessen, R. S., Mac Low, M., Galván-Madrid, R., & Keto, E. R. 2010, ApJ, 711, 1017
 Reid, M. A., Wadsley, J., Petitclerc, N., & Sills, A. 2010, ApJ, 719, 561
 Reid, M. J. et al. 2009, ApJ, 700, 137
 Rivera-Ingraham, A. et al. 2010, 1009.1296
 Roman-Duval, J., Jackson, J. M., Heyer, M., Rathborne, J., & Simon, R. 2010, ApJ, 723, 492
 Roshi, D. A., Bailer, D. S., Bania, T. M., Goss, W. M., & De Pree, C. G. 2005, ApJ, 625, 181
 Rosolowsky, E. et al. 2010, ApJS, 188, 123
 Sewilo, M., Watson, C., Araya, E., Churchwell, E., Hofner, P., & Kurtz, S. 2004, ApJS, 154, 553
 Sunada, K., Nakazato, T., Ikeda, N., Hongo, S., Kitamura, Y., & Yang, J. 2007, PASJ, 59, 1185
 Troscompt, N., Faure, A., Maret, S., Ceccarelli, C., Hily-Blant, P., & Wiesenfeld, L. 2009a, A&A, 506, 1243
 Troscompt, N., Faure, A., Wiesenfeld, L., Ceccarelli, C., & Valiron, P. 2009b, A&A, 493, 687
 Turner, B. E., Richard, L. J., & Xu, L. 1989, ApJ, 344, 292
 Urquhart, J. S. et al. 2009, A&A, 501, 539
 van der Tak, F. F. S., Black, J. H., Schöier, F. L., Jansen, D. J., & van Dishoeck, E. F. 2007, A&A, 468, 627
 Wadiak, E. J., Rood, R. T., & Wilson, T. L. 1988, ApJ, 324, 931
 Wilson, T. L., Rohlfs, K., & Hüttemeister, S. 2009, Tools of radio astronomy (Springer)
 Zeiger, B. & Darling, J. 2010, ApJ, 709, 386
 Zylka, R., Guesten, R., Henkel, C., & Batrla, W. 1992, A&AS, 96, 525

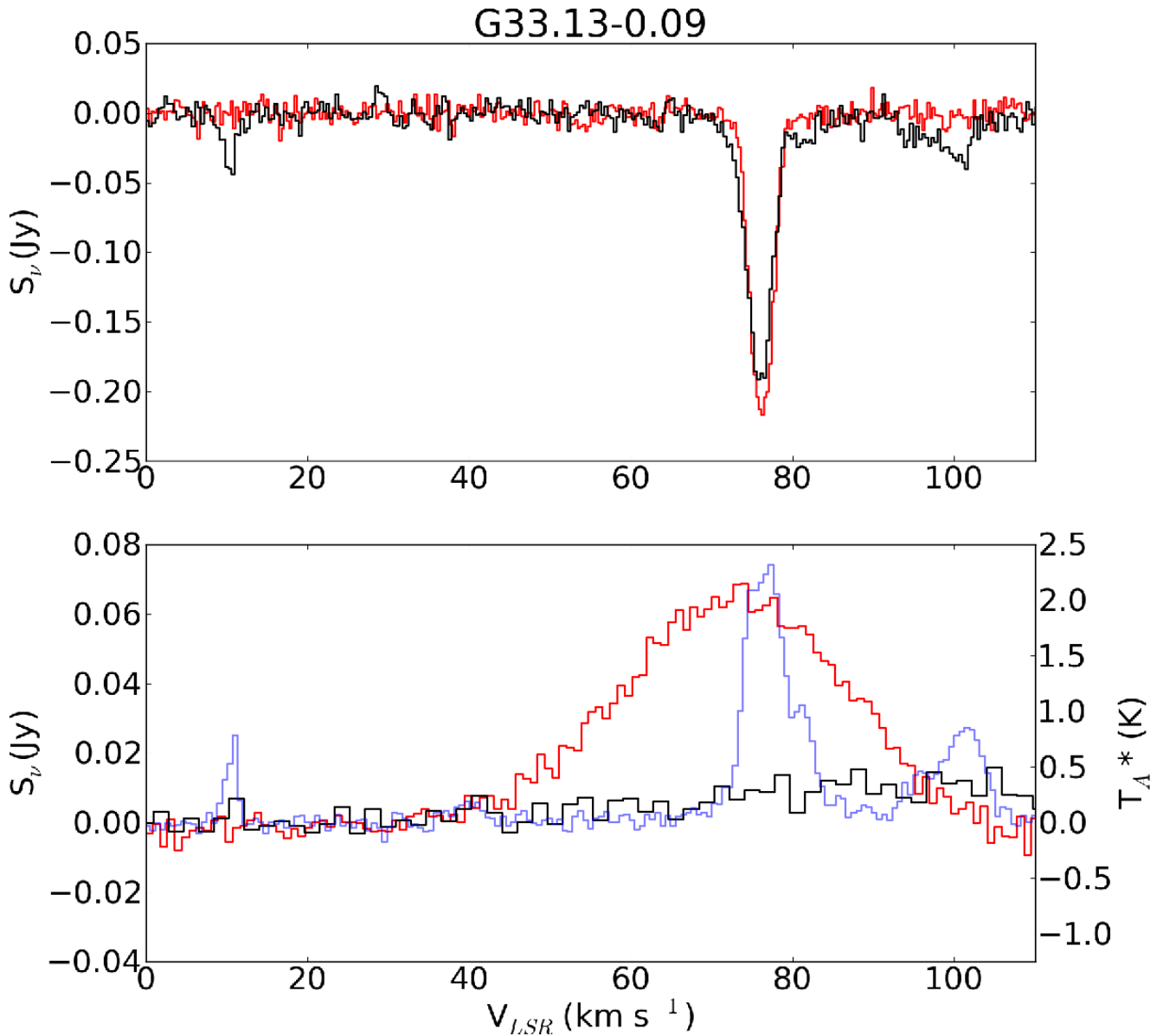


Figure 23. *Top:* The GBT $2_{11} - 2_{12}$ and Arecibo $1_{10} - 1_{11}$ spectra of G33.13-0.09. *Bottom:* The GBT H75 α and Arecibo H110 α spectra with the GRS ^{13}CO spectrum overlaid. The left axis is for the RRLs and the right axis is for the ^{13}CO .

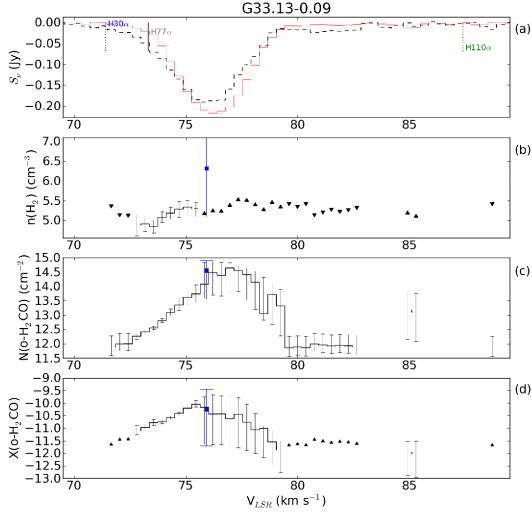


Figure 24. Same panel description as Figure 15. The recombination lines in this source show enormously different velocities. H110 α is $14.6 \pm 2.9 \text{ km s}^{-1}$ redshifted from H75-77 α , which is a significant fraction of the total line width ($\sigma_{110} = 41.6 \pm 6.35, \sigma_{75} = 31.8 \pm 2.2$). Churchwell et al. (2010) measure H30 α slightly bluer still, $v_{30} = 71.4 \pm 1.7 \text{ km s}^{-1}, \sigma_{30} = 27.8 \pm 3.2 \text{ km s}^{-1}$. This discrepancy could be explained by a significant gradient in the density of the ionized gas with velocity, i.e. low-density gas blowing out from the back side of the UCH II region. The tail of redshifted gas from 80-85 km s^{-1} is either rapidly-infalling, low-column gas (Scenario 2) or unassociated line-of-sight cloud material (Scenario 5). The main line has a number of points in which only a lower limit on density could be measured, but because of the rising lower limits out to $\sim 78 \text{ km s}^{-1}$, the spectrum is classified as a red gradient.

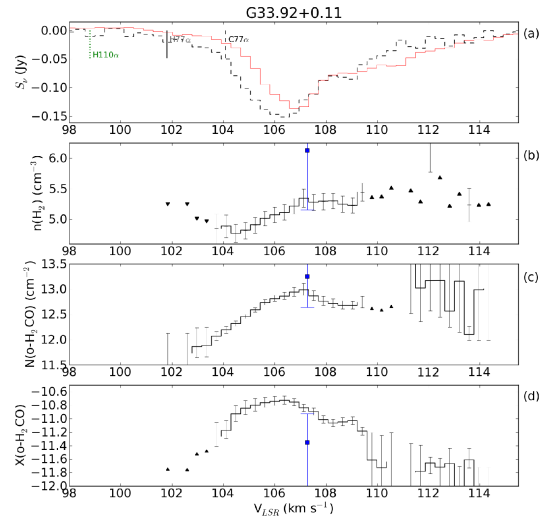
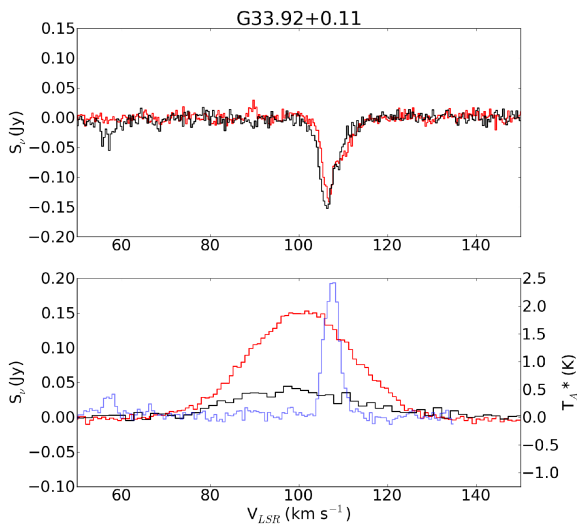


Figure 25. *Left:* Same description as Figure 1. *Right:* Panels described in Figure 15. The red gradient and carbon recombination line at a velocity between the hydrogen lines and the H₂CO density peak are consistent with the inside-out collapse model, Scenario 2. The larger systematic error bars included for the main line resulted in a lower limit on density being measured. In this spectrum, a gaussian line fit is not representative of the line profile.

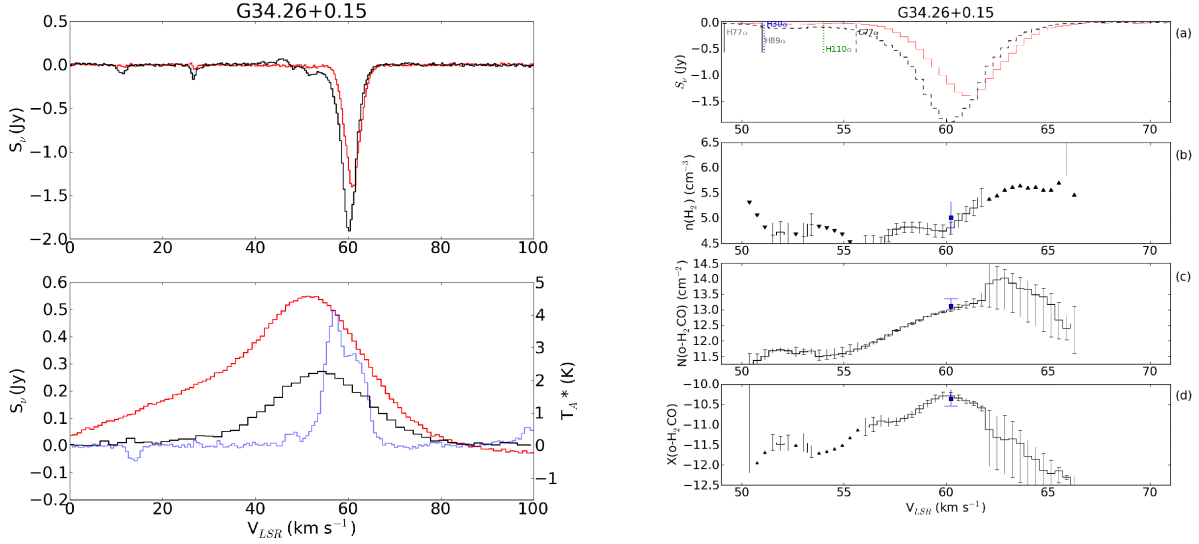


Figure 26. *Left:* Same description as Figure 1. *Right:* Panels described in Figure 15. The red velocity gradient in this source is very steep and widely separated (by $6 - 15 \text{ km s}^{-1}$) from the RRL velocities, indicating that the dense gas is rapidly approaching the UCH II region. The line profile is exemplary of Scenario 2, inside-out collapse, since the dense gas is redshifted of the recombination lines and the C RRL is at an intermediate velocity. The derived density at the peak is lower than previous measurements of density using C^{34}S and the mm transitions of H_2CO (Mangum & Wootten 1993), although both of those measurements are consistent with the density in at least one velocity bin. The measurements are consistent despite the high temperature ($T_K = 230\text{K}$) measured by (Mangum & Wootten 1993).

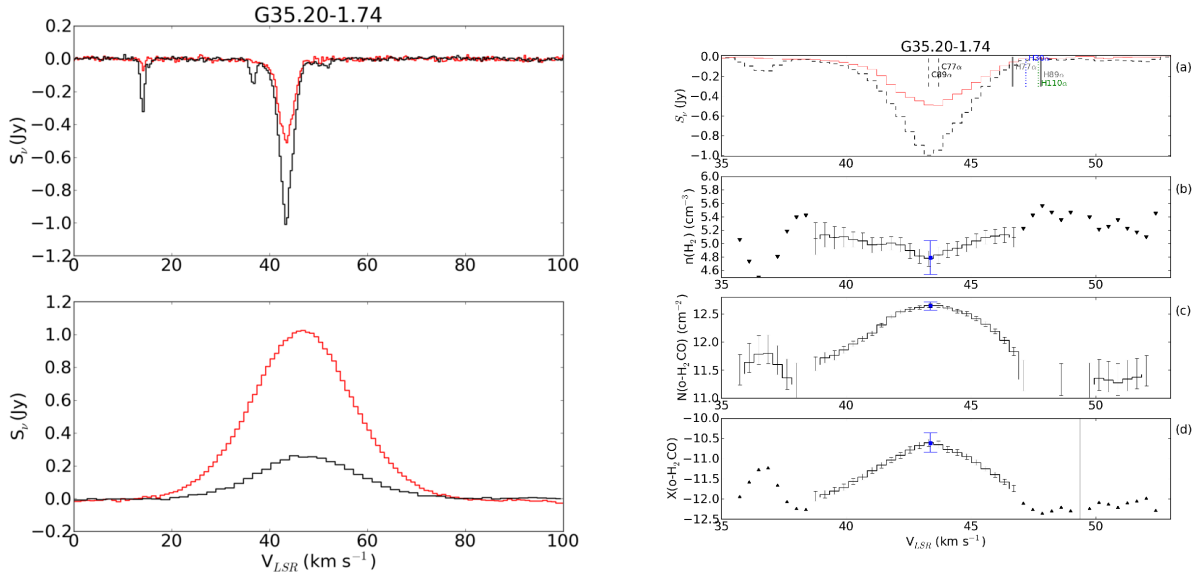


Figure 27. *Left:* Same description as Figure 1. *Right:* For panel descriptions, see Figure 15. Identified as a single gaussian line. The line peak could be optically thick based on morphological comparison to G69.54-0.98. Since the carbon RRLs are aligned with the H_2CO column peak and both are blueshifted from the hydrogen RRLs, this spectrum is consistent with Scenario 4, in which a layer of gas is being pushed towards the observer and compressed.

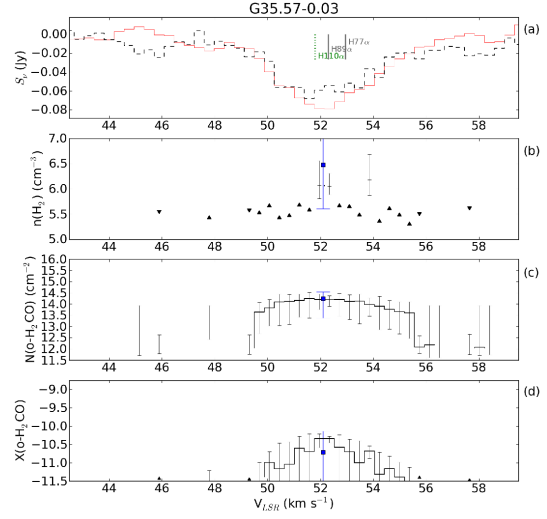
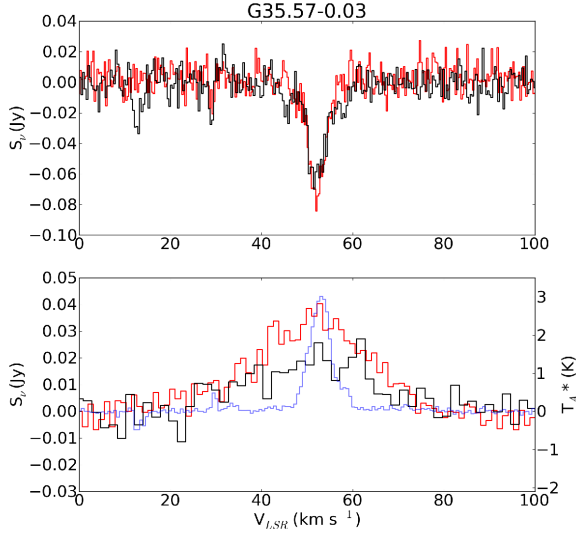


Figure 28. *Left:* Same description as Figure 1. One of the two off positions contained an absorption line at 45 km s⁻¹; the position was coincident with an IRDC. *Right:* For panel descriptions, see Figure 15. The densities measured are very high ($n(\text{H}_2) > 10^6 \text{ cm}^{-3}$) and lower limits are all at similar levels. The match between the H₂CO and RRL velocities and the slight blueshift of the lower frequency RRLs suggest that this source is consistent with Scenario 1, though the lack of a carbon RRL detection suggests that the UCH II and molecular gas are not interacting.

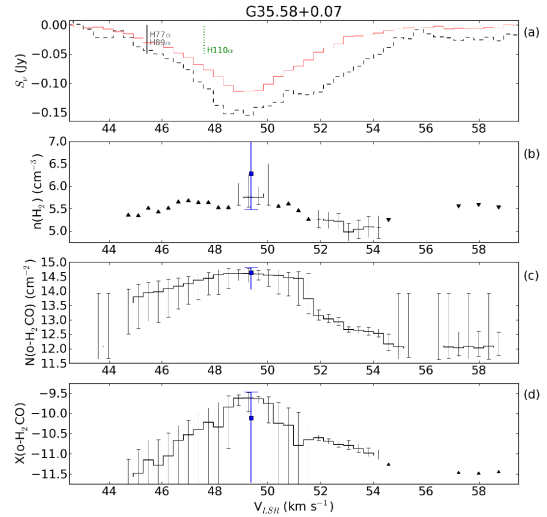
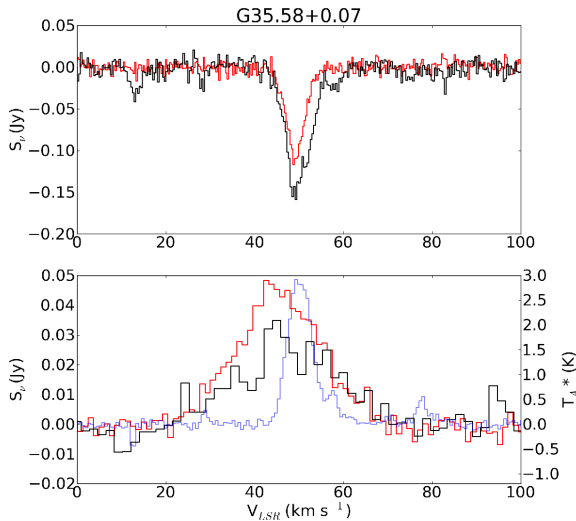


Figure 29. *Left:* Same description as Figure 1. *Right:* For panel descriptions, see Figure 15. Identified as a blue gradient because of the low density region centered around 53 km s⁻¹. However, in this source, the low density region is also substantially lower column per km s⁻¹ pc⁻¹, so it may be more appropriate to classify as an envelope. Because the peak density is slightly redshifted from the RRL velocities, this source is consistent with Scenario 2, but the lack of carbon RRLs and the lower limits on density at many velocities makes the match imperfect.

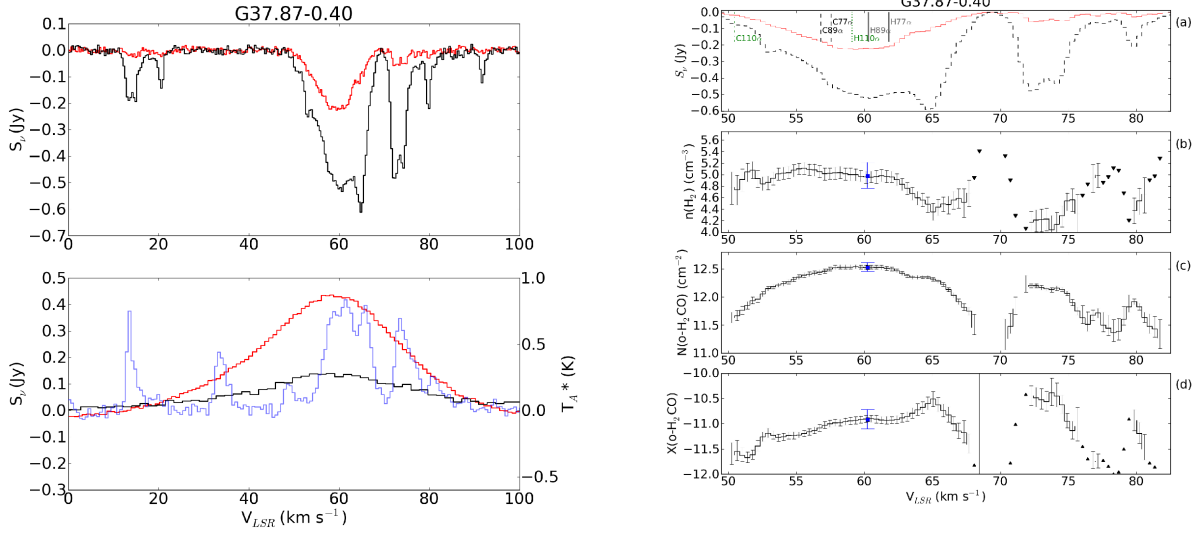


Figure 30. *Left:* Same description as Figure 1. *Right:* Plot of the derived parameters per velocity bin for G37.87-0.40. This source is an example with high column and density associated with the line core (55-63 km s^{-1}) and declining columns at the edge of the line core (50-55, 63-67 km s^{-1}) with additional low density ($n < 10^{4.8} \text{ cm}^{-3}$) components along the line of sight. A modest increase in density towards bluer velocities is observed, but the complexity of the line morphology suggests that this gradient may represent unassociated line of sight clouds. The relative velocities of the carbon and hydrogen recombination lines are consistent with the very simple Scenario 1, although the H_2CO line suggests a more complex situation.

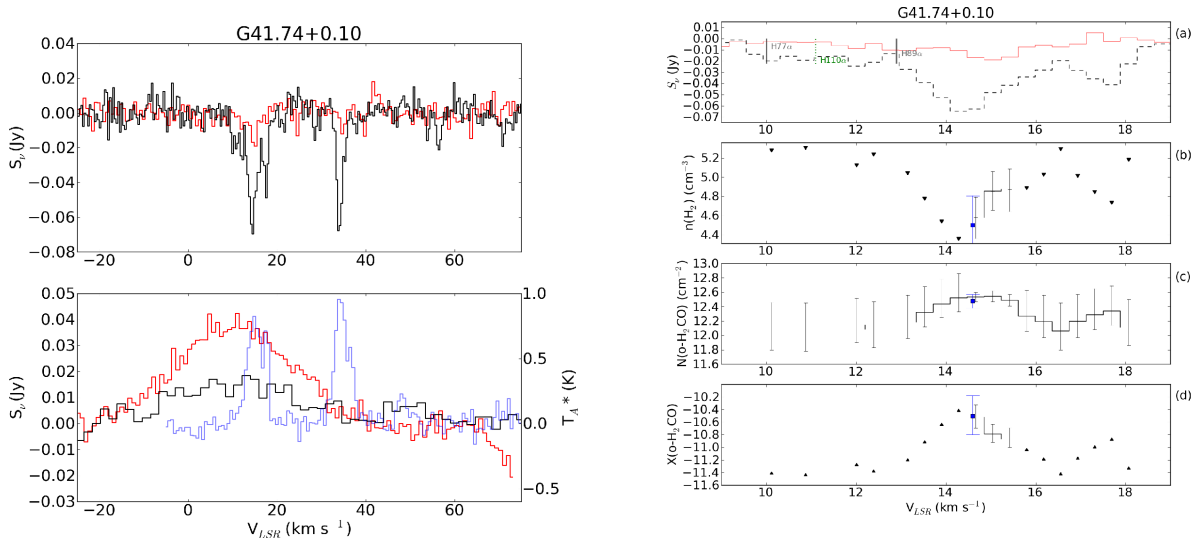


Figure 31. *Left:* Same description as Figure 1. *Right:* Panels described in Figure 15. The S/N is only adequate to place upper limits on density at most velocities. Because of the low S/N, we do not attempt to associate G41.74 with any of the physical scenarios from section 6.3.

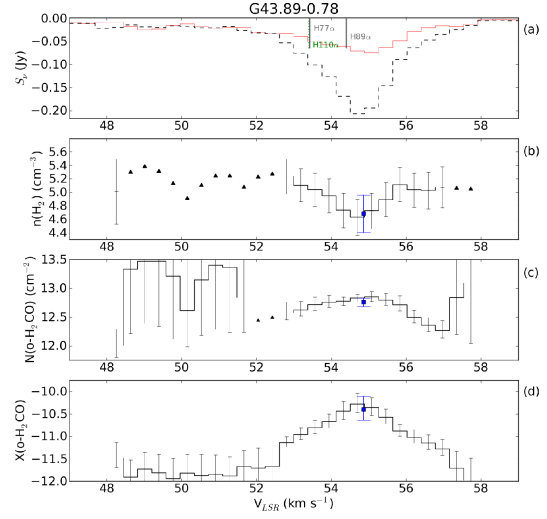
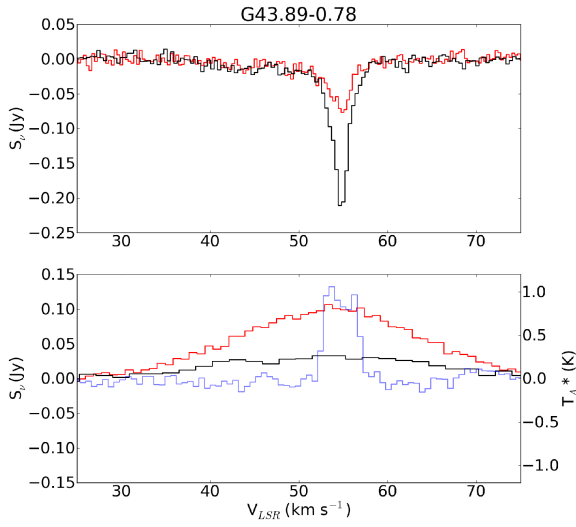


Figure 32. *Left:* Same description as Figure 1. *Right:* Plot of the derived parameters per velocity bin for G43.89-0.78. For panel descriptions, see Figure 15. The line core (55 km s^{-1}) is very deep in the $1_{10} - 1_{11}$ line but the $1_{10} - 1_{11}/2_{11} - 2_{12}$ ratio, and therefore the spatial density, is substantially higher in the blue tail ($48\text{--}52 \text{ km s}^{-1}$). Since the column densities are lower in the blue tail, it probably represents a relatively small patch of highly turbulent, high-density material as in Scenario 5. It is also possible that the blue tail represents an outflow as in Scenario 3, but the high density measured is not expected in an outflow. It is possible that there is a significant contribution to the 55 km s^{-1} $1_{10} - 1_{11}$ line from surrounding low-density gas in the beam absorbing against the CMB, creating a Type 3 error (Table 6).

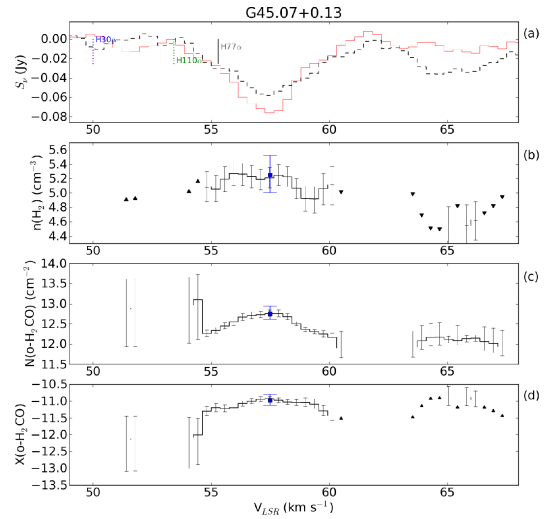
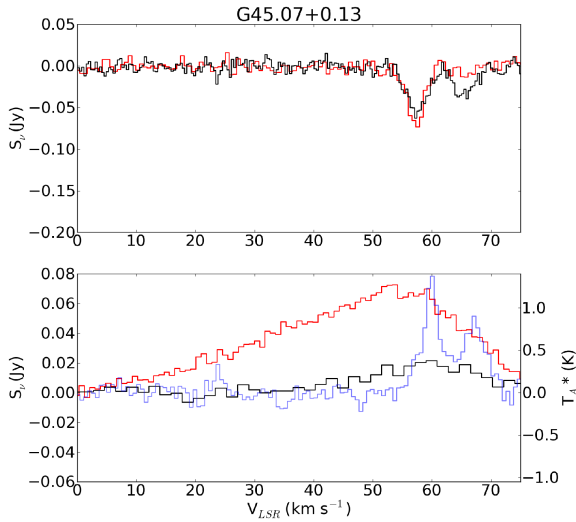


Figure 33. *Left:* Same panel description as Figure 1. The H75 α line cannot be fit by a single gaussian. *Right:* For panel descriptions, see Figure 15. The velocity difference between the RRLs and the H₂CO lines is consistent with Scenario 2, but no carbon RRL is observed so there is no direct evidence of interaction between the UCH II region and the molecular gas.

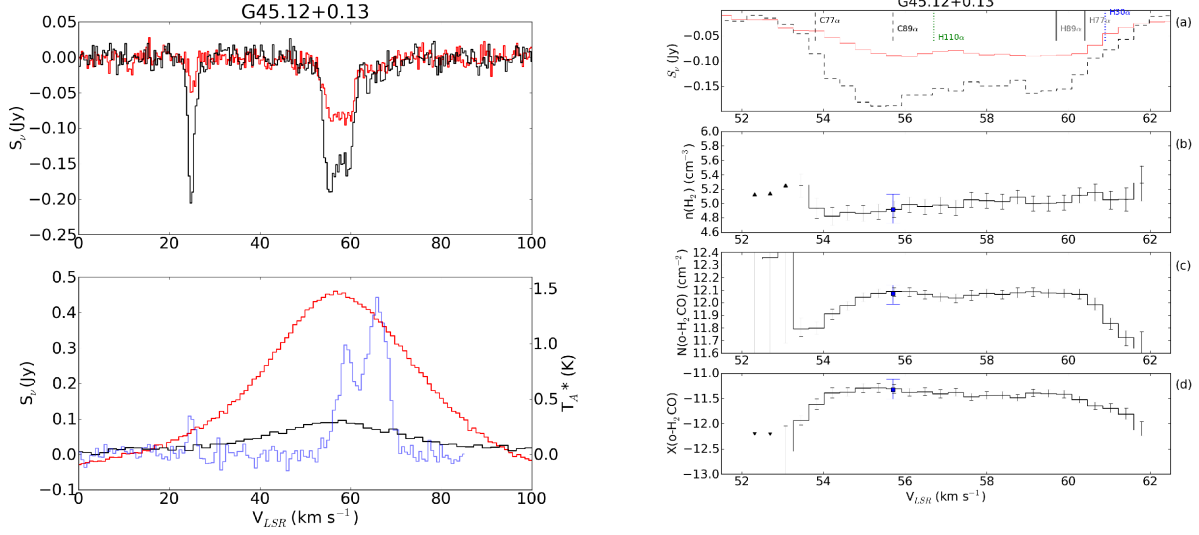


Figure 34. *Left:* Same description as Figure 1 *Right:* For panel descriptions, see Figure 15. The line is classified as *other* because of the very wide, flat line. The relative velocities of the recombination lines and their alignment with the H₂CO line are consistent with Scenario 1.

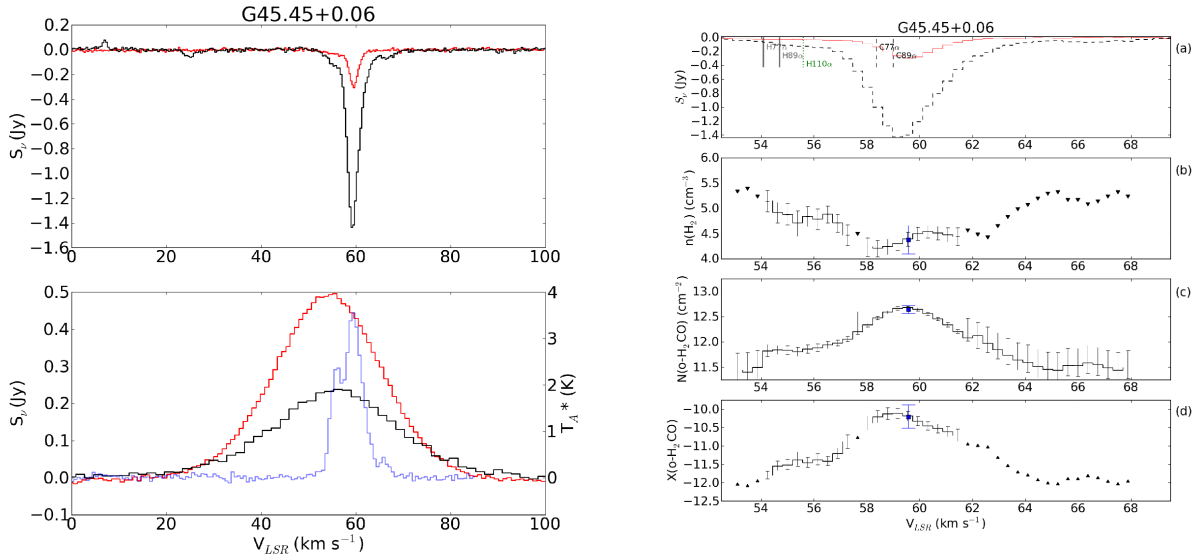


Figure 35. *Left:* Same description as Figure 1 *Right:* For panel descriptions, see Figure 15. Identified as a blue gradient because density clearly increases towards the blue, while only upper limits are measured towards the red. Based on the relative locations of the RRLs and the peak H₂CO column, the spectrum appears to be consistent with Scenario 2.

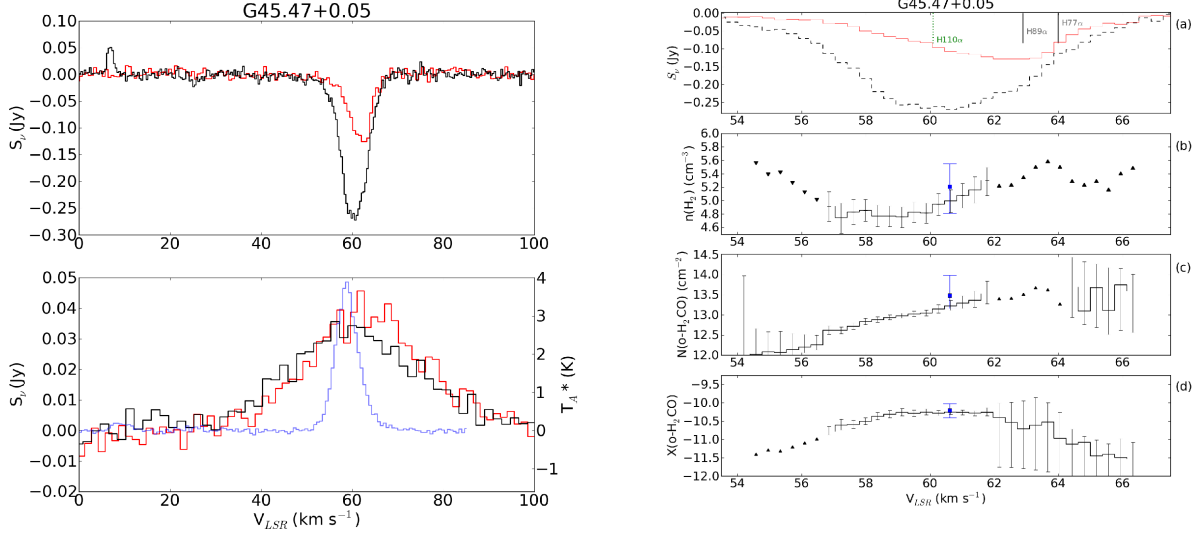


Figure 36. *Left:* Same description as Figure 1 *Right:* Panels described in Figure 15. Identified as a red gradient. The hydrogen recombination line velocities are consistent with Scenario 1. However, the highest density gas is the most redshifted, which is more consistent with Scenario 2. Additionally, there is a low-density blueshifted tail that is suggestive of an outflow as in Scenario 3.

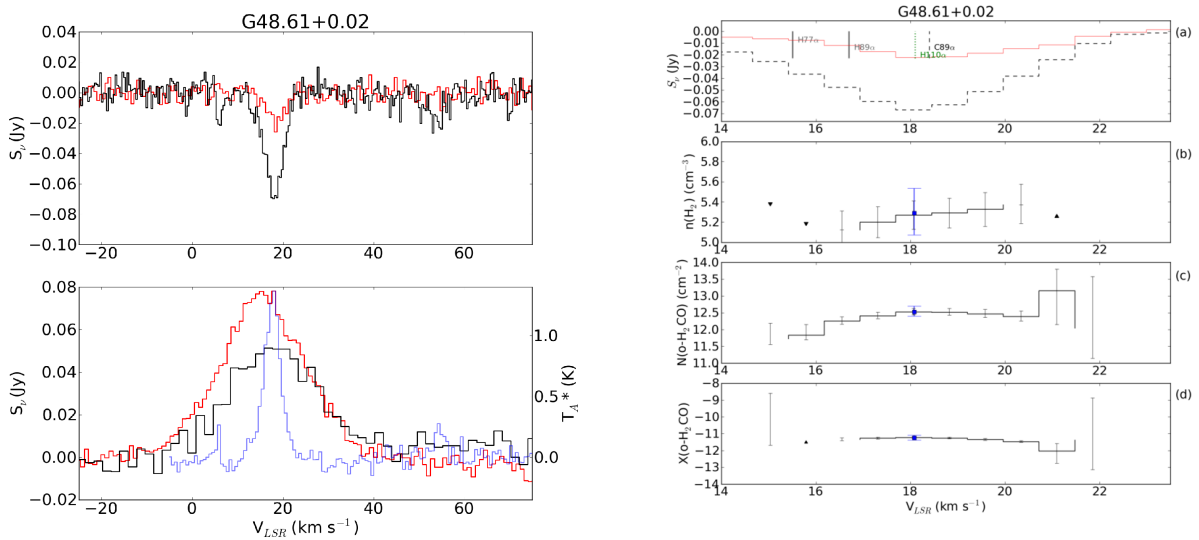


Figure 37. *Left:* Same description as Figure 1 *Right:* Panels described in Figure 15. Identified as a red gradient. The RRL locations and density profile are consistent with Scenario 2, but the modest S/N leaves open the possibility of other explanations.

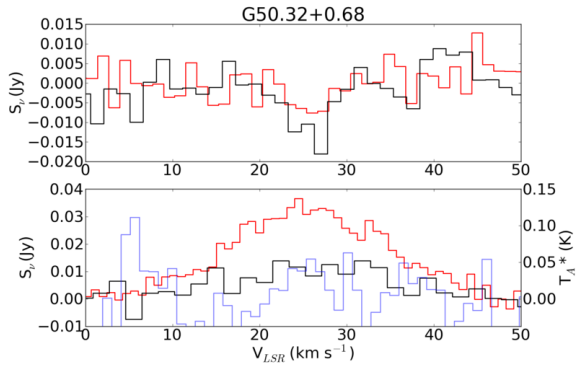


Figure 38. Same description as Figure 1. There were not enough adjacent high S/N velocity bins to perform the velocity-density analysis. However, the velocity coincidence of the detected H RRLs and H₂CO lines suggests that this source is an example of Scenario 1, but no carbon RRL is detected.

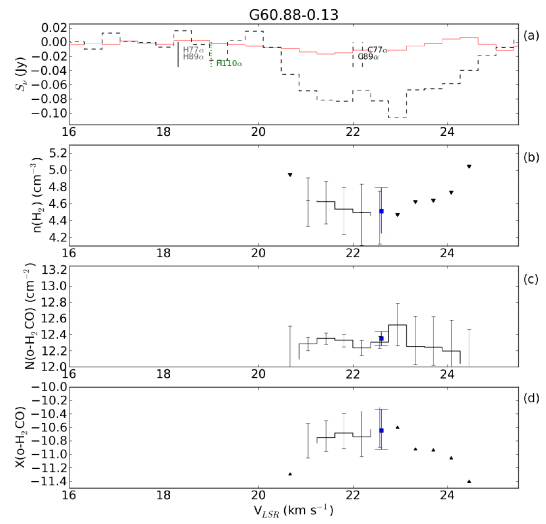
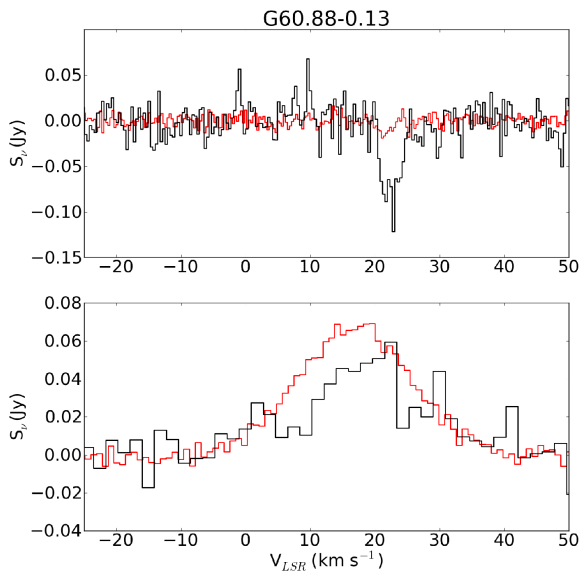


Figure 39. *Left:* Same description as Figure 1 *Right:* Panels described in Figure 15. It was only possible to derive upper limits on density at most velocities. The locations of the RRLs and H₂CO lines are consistent with Scenario 2.

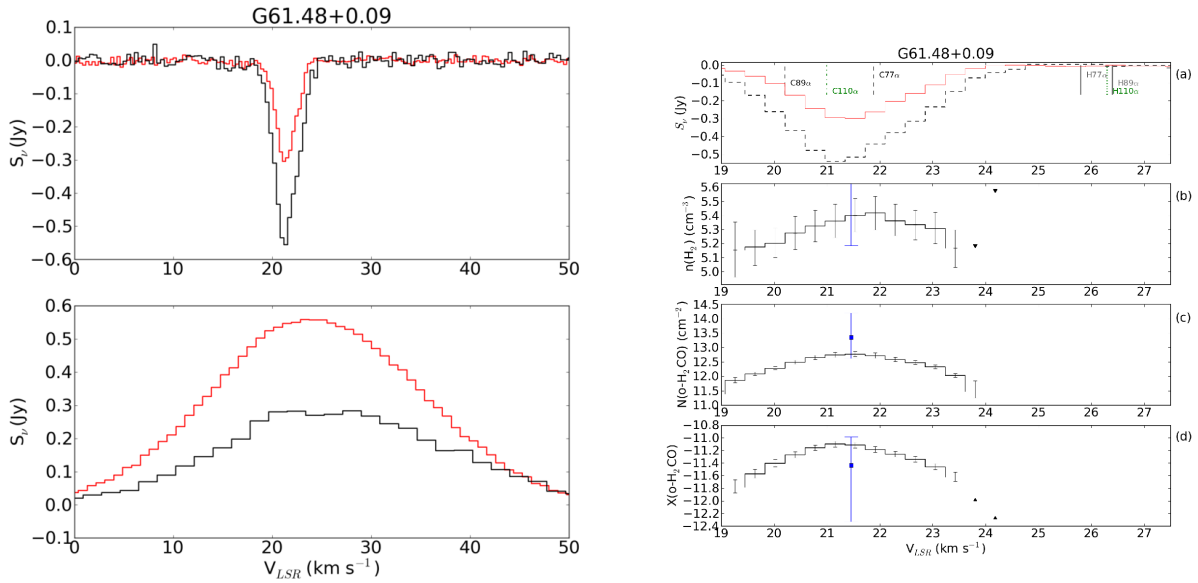


Figure 40. *Left:* Same description as Figure 1 *Right:* Panels described in Figure 15. Identified as a single gaussian morphology because of the peak in density and column. Because both the H₂CO and carbon RRLs are blueshifted from the hydrogen RRLs, this source is an excellent example of Scenario 4.

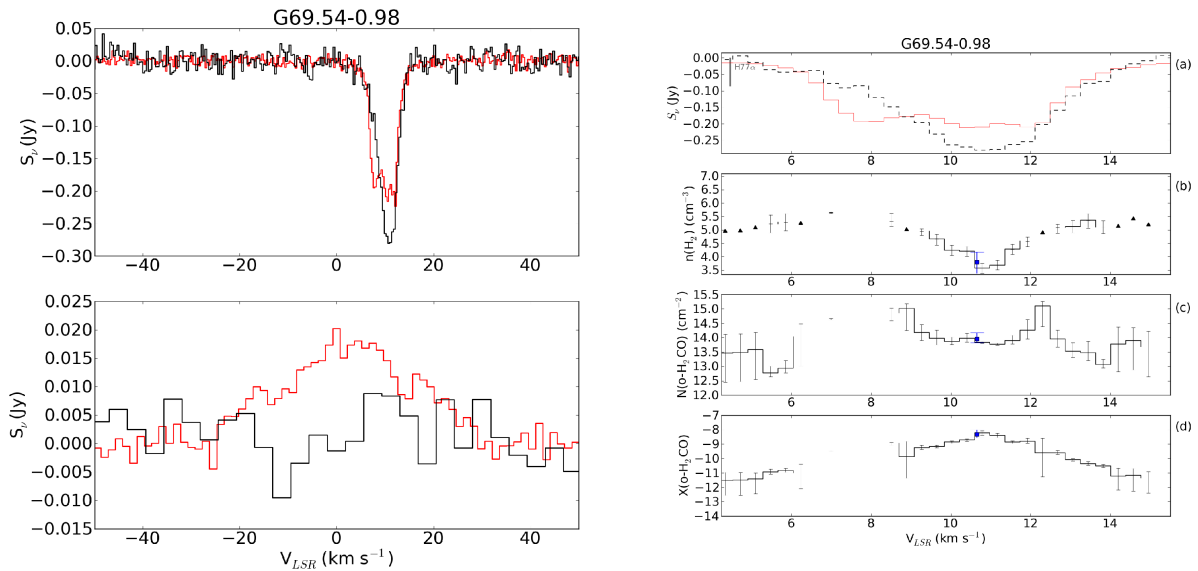


Figure 41. *Left:* Same description as Figure 1 *Right:* Panels described in Figure 15. The flat-bottomed line profile suggests that the absorption in this source is optically thick. The blank region around 8 km s⁻¹ is where there is no allowed parameter space in the models. The rest of the measurements are likely to be incorrect because they are biased by optically thick components contributing to the line. Because of the added uncertainty in the density measurement from the high line optical depth, it is not clear what scenario, if any, this source's line profile is consistent with. However, the RRL at 16.4 km s⁻¹ (off the right side of the spectrum) would be consistent with Scenarios 4 and 5.

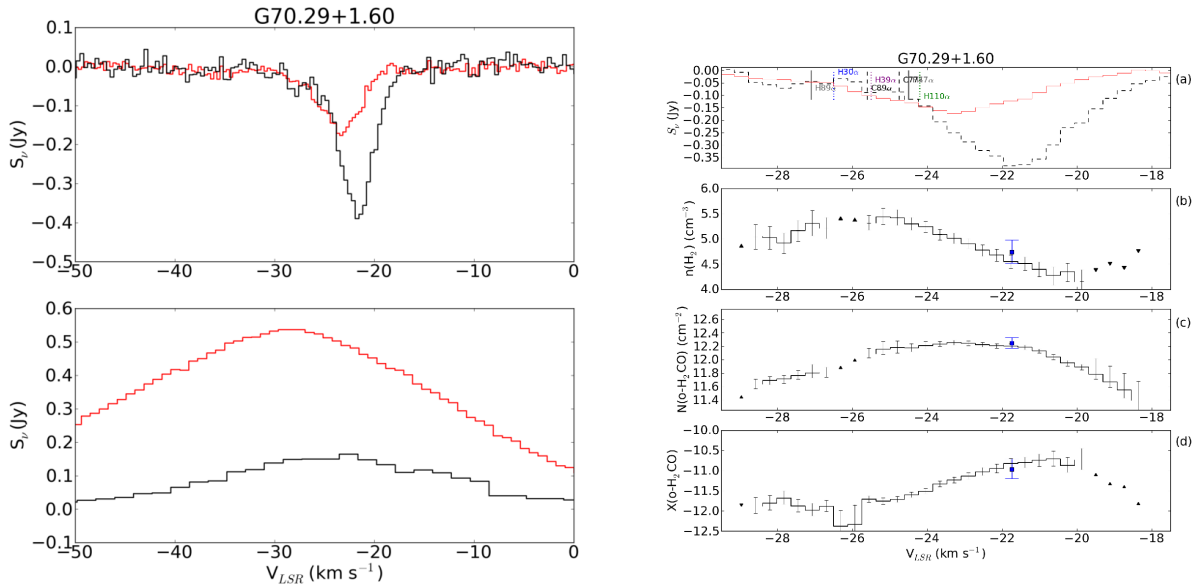


Figure 42. *Left:* Same description as Figure 1 *Right:* Plot of the derived parameters per velocity bin for G70.29+1.60. For panel descriptions, see Figure 15. The velocity offset between the $1_{10} - 1_{11}$ and $2_{11} - 2_{12}$ line centers results in a strong blue density gradient. Since the density peaks at the same velocity as the UCH II region, but there is high column gas redshifted of the density peak, the spectrum is not directly consistent with Scenario 2, to which it is otherwise similar.

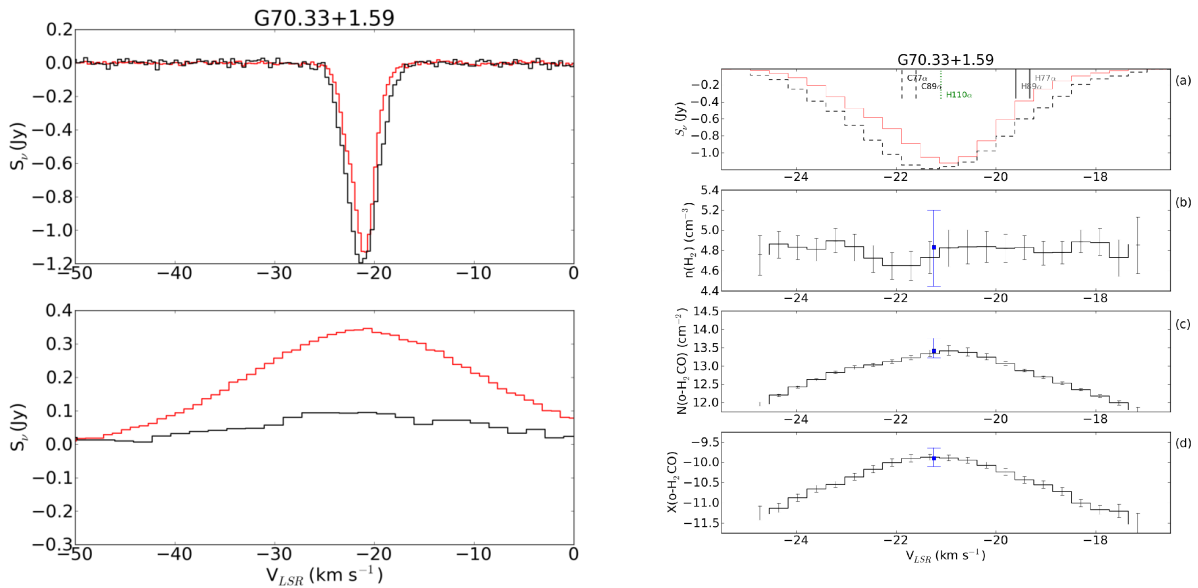


Figure 43. *Left:* Same description as Figure 1 *Right:* Plot of the derived parameters per velocity bin for G70.33+1.59. For panel descriptions, see Figure 15. Unlike G70.29+1.60, there is no offset between the $1_{10} - 1_{11}$ and $2_{11} - 2_{12}$ line centers, so this source is consistent with a single gas component along the line of sight. Because carbon recombination lines are detected, though, it is evident that the UCH II region is interacting with the molecular gas. The recombination line velocities are consistent with Scenario 1, but the lack of a gradient in the H_2CO -derived density is not. The region could be intermediate between Scenario 2 (infall) and Scenario 1 (expansion), causing the observed density to be more evenly spread in velocity even though it varies spatially.

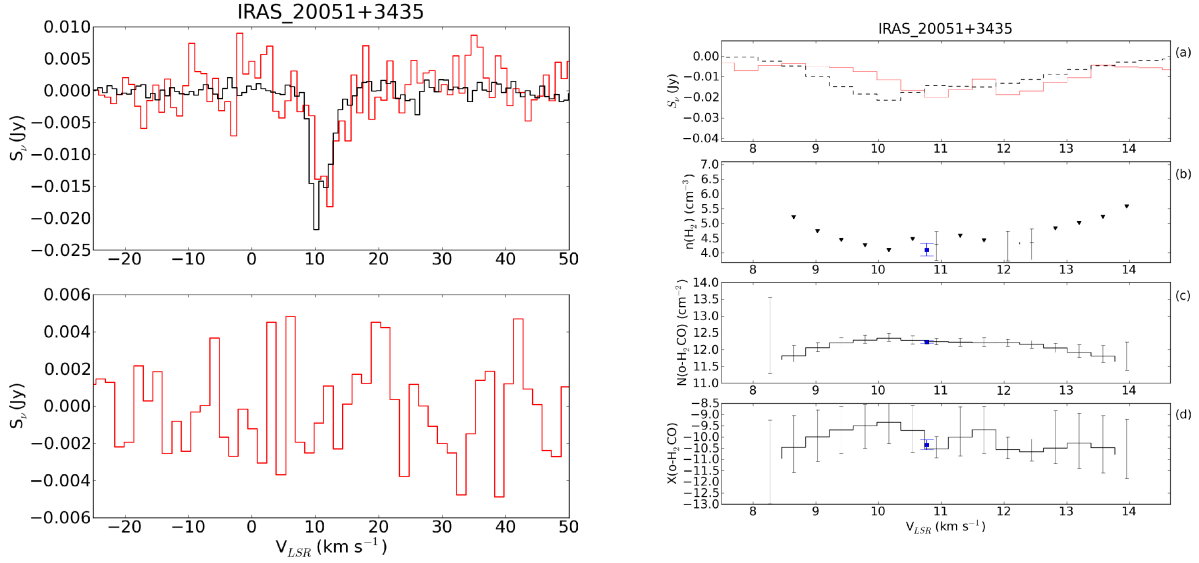


Figure 44. *Left:* Same description as Figure 1 *Right:* Panels described in Figure 15. There is no continuum emission or RRL detected towards this source: the absorption is exclusively against the CMB. Urquhart et al. (2009) report a HCH II detection at 0.23 mJy at 6cm, which is substantially lower than the ~ 20 mJy absorption detected in the $1_{10} - 1_{11}$ line. The presence of a faint HCH II region and water masers (Sunada et al. 2007) suggest that this is an active but very young region, probably the youngest in our sample. It is therefore a good example of what can be expected of a survey selected from millimeter sources instead of UCH II regions. Because of the lack of an RRL detection and the low S/N, we cannot classify this source in an UCH II scenario.

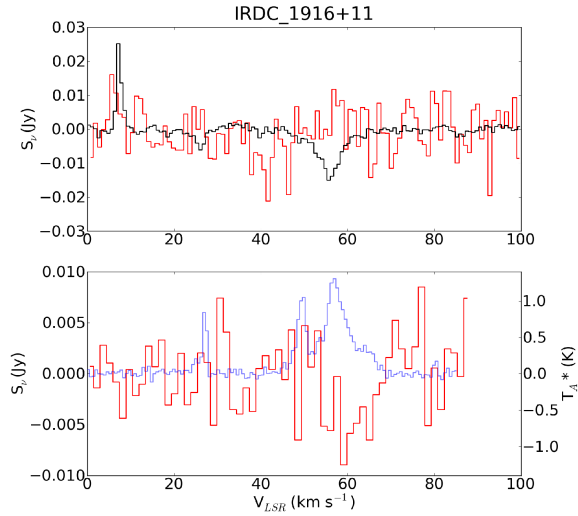


Figure 45. Same description as Figure 1. The $2_{11} - 2_{12}$ noise levels are too great to measure physically interesting limits on the density. No continuum emission is detected at 2 cm, 6 cm, or 1.1 mm. There is also no evidence of an IRDC in the Spitzer $8\mu\text{m}$ image. This sightline is probably more accurately characterized as a lack of emission region rather than a dust-absorbed IRDC. The three $1_{10} - 1_{11}$ absorption features detected are associated with ^{13}CO clouds and only have density upper limits from our data. These observations are a strong indication that deep enough H₂CO observations in the Galactic plane will always detect H₂CO against the CMB or diffuse galactic background, and therefore it can be used to measure (or constrain) densities of even diffuse GMCs.

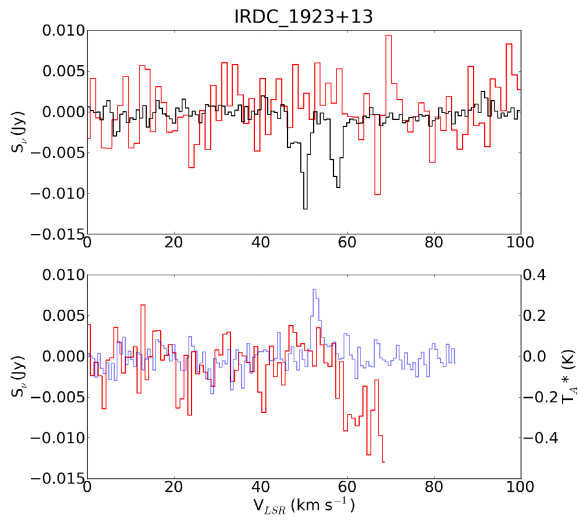


Figure 46. Same description as Figure 1. The $2_{11} - 2_{12}$ noise levels are too great to measure physically interesting limits on the density.